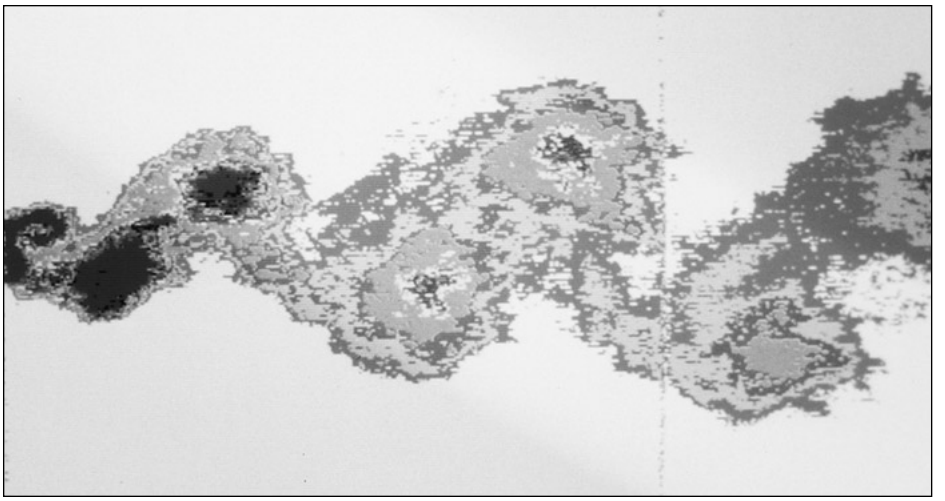

The turbulent wake behind a bluff body immersed in a stream flow is a subject of the present chapter. This is a digitized video image showing the distribution of tracer-dye concentration in the wake of the body. Compare with Fig. 5.2a of the text, which is a laminar wake. *(Courtesy of R. Balachandar, by permission of the American Society of Mechanical Engineers.)*

Chapter 7
Flow Past Immersed Bodies

Motivation. This chapter is devoted to "external" flows around bodies immersed in a fluid stream. Such a flow will have viscous (shear and no-slip) effects near the body surfaces and in its wake, but will typically be nearly inviscid far from the body. These are unconfined *boundary-layer* flows.

Chapter 6 considered "internal" flows confined by the walls of a duct. In that case the viscous boundary layers grow from the sidewalls, meet downstream, and fill the entire duct. Viscous shear is the dominant effect. For example, the Moody chart of Fig. 6.13 is essentially a correlation of wall shear stress for long ducts of constant cross section.

External flows are unconfined, free to expand no matter how thick the viscous layers grow. Although boundary-layer theory (Sec. 7.3) is helpful in understanding external flows, complex body geometries usually require experimental data on the forces and moments caused by the flow. Such immersed-body flows are commonly encountered in engineering studies: *aerodynamics* (airplanes, rockets, projectiles), *hydrodynamics* (ships, submarines, torpedos), *transportation* (automobiles, trucks, cycles), *wind engineering* (buildings, bridges, water towers, wind turbines), and *ocean engineering* (buoys, breakwaters, pilings, cables, moored instruments). This chapter provides data and analysis to assist in such studies.

7.1 Reynolds-Number and Geometry Effects

The technique of boundary-layer (BL) analysis can be used to compute viscous effects near solid walls and to "patch" these onto the outer inviscid motion. This patching is more successful as the body Reynolds number becomes larger, as shown in Fig. 7.1.

In Fig. 7.1 a uniform stream U moves parallel to a sharp flat plate of length L. If the Reynolds number UL/ν is low (Fig. 7.1*a*), the viscous region is very broad and extends far ahead and to the sides of the plate. The plate retards the oncoming stream greatly, and small changes in flow parameters cause large changes in the pressure distribution along the plate. Thus, although in principle it should be possible to patch the

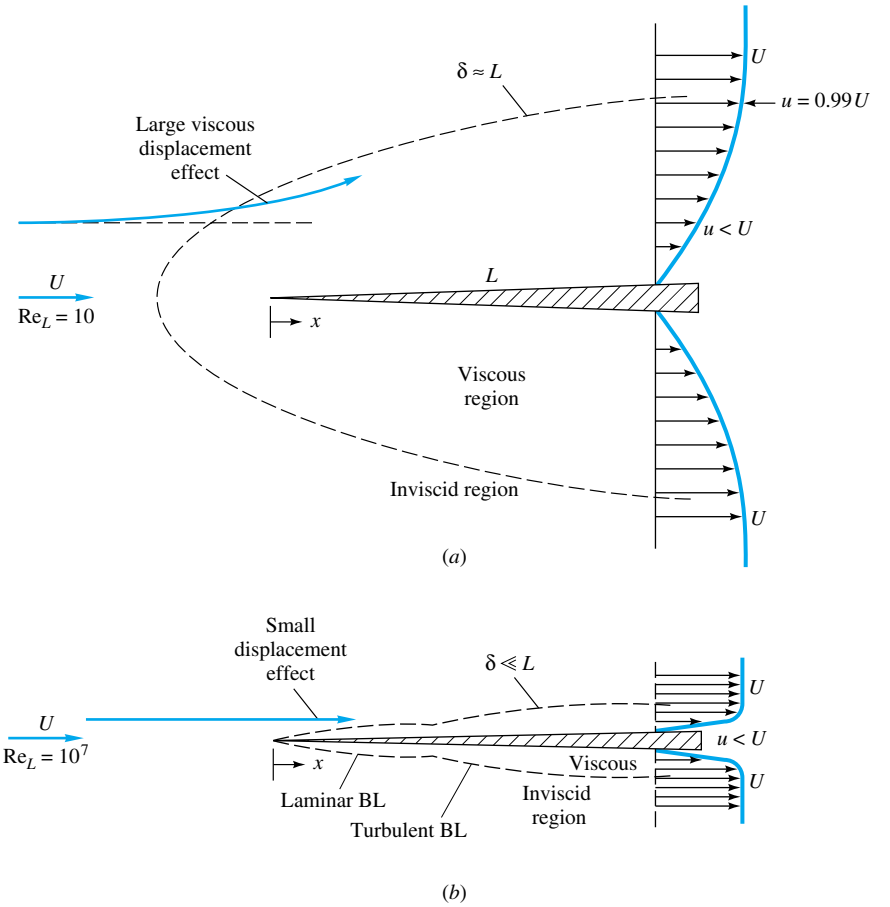

Fig. 7.1 Comparison of flow past a sharp flat plate at low and high Reynolds numbers: (*a*) laminar, low-Re flow; (*b*) high-Re flow.

viscous and inviscid layers in a mathematical analysis, their interaction is strong and nonlinear [1 to 3]. There is no existing simple theory for external-flow analysis at Reynolds numbers from 1 to about 1000. Such thick-shear-layer flows are typically studied by experiment or by numerical modeling of the flow field on a digital computer [4].

A high-Reynolds-number flow (Fig. 7.1*b*) is much more amenable to boundary-layer patching, as first pointed out by Prandtl in 1904. The viscous layers, either laminar or turbulent, are very thin, thinner even than the drawing shows. We define the boundary-layer thickness δ as the locus of points where the velocity u parallel to the plate reaches 99 percent of the external velocity U. As we shall see in Sec. 7.4, the accepted formulas for flat-plate flow are

$$\frac{\delta}{x} \approx \begin{cases} \dfrac{5.0}{\mathrm{Re}_x^{1/2}} & \text{laminar} \quad (7.1a) \\ \dfrac{0.16}{\mathrm{Re}_x^{1/7}} & \text{turbulent} \quad (7.1b) \end{cases}$$

where $\mathrm{Re}_x = Ux/\nu$ is called the *local Reynolds number* of the flow along the plate surface. The turbulent-flow formula applies for Re_x greater than approximately 10^6.

Some computed values from Eq. (7.1) are

Re_x	10^4	10^5	10^6	10^7	10^8
$(\delta/x)_{\mathrm{lam}}$	0.050	0.016	0.005		
$(\delta/x)_{\mathrm{turb}}$			0.022	0.016	0.011

The blanks indicate that the formula is not applicable. In all cases these boundary layers are so thin that their displacement effect on the outer inviscid layer is negligible. Thus the pressure distribution along the plate can be computed from inviscid theory as if the boundary layer were not even there. This external pressure field then "drives" the boundary-layer flow, acting as a forcing function in the momentum equation along the surface. We shall explain this boundary-layer theory in Secs. 7.4 and 7.5.

For slender bodies, such as plates and airfoils parallel to the oncoming stream, we conclude that this assumption of negligible interaction between the boundary layer and the outer pressure distribution is an excellent approximation.

For a blunt-body flow, however, even at very high Reynolds numbers, there is a discrepancy in the viscous-inviscid patching concept. Figure 7.2 shows two sketches of flow past a two- or three-dimensional blunt body. In the idealized sketch (7.2*a*), there is a thin film of boundary layer about the body and a narrow sheet of viscous wake in the rear. The patching theory would be glorious for this picture, but it is false. In the

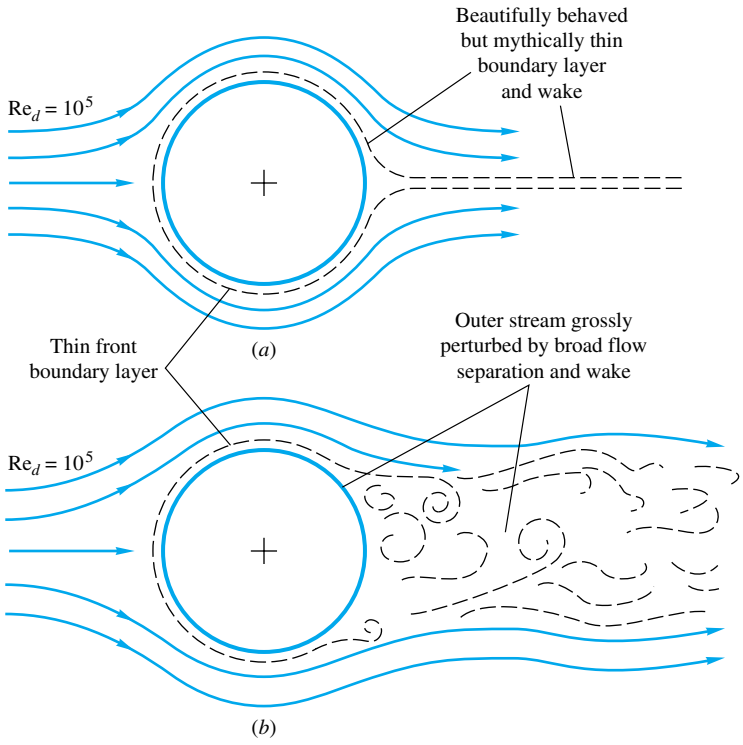

Fig. 7.2 Illustration of the strong interaction between viscous and inviscid regions in the rear of blunt-body flow: (*a*) idealized and definitely false picture of blunt-body flow; (*b*) actual picture of blunt-body flow.

actual flow (Fig. 7.2*b*), the boundary layer is thin on the front, or windward, side of the body, where the pressure decreases along the surface (*favorable* pressure gradient). But in the rear the boundary layer encounters increasing pressure (*adverse* pressure gradient) and breaks off, or separates, into a broad, pulsating wake. (See Fig. 5.2*a* for a photograph of a specific example.) The mainstream is deflected by this wake, so that the external flow is quite different from the prediction from inviscid theory with the addition of a thin boundary layer.

The theory of strong interaction between blunt-body viscous and inviscid layers is not well developed. Flows like that of Fig. 7.2*b* are normally studied experimentally. Reference 5 is an example of efforts to improve the theory of separated-boundary-layer flows. Reference 6 is a textbook devoted to separated flow.

EXAMPLE 7.1

A long, thin flat plate is placed parallel to a 20-ft/s stream of water at 20°C. At what distance x from the leading edge will the boundary-layer thickness be 1 in?

Solution

Since we do not know the Reynolds number, we must guess which of Eqs. (7.1) applies. From Table 1.4 for water, $\nu = 1.09 \times 10^{-5}$ ft^2/s; hence

$$\frac{U}{\nu} = \frac{20 \text{ ft/s}}{1.09 \times 10^{-5} \text{ ft}^2/\text{s}} = 1.84 \times 10^6 \text{ ft}^{-1}$$

With $\delta = 1$ in $= \frac{1}{12}$ ft, try Eq. (7.1*a*):

Laminar flow:
$$\frac{\delta}{x} = \frac{5}{(Ux/\nu)^{1/2}}$$

or
$$x = \frac{\delta^2(U/\nu)}{5^2} = \frac{(\frac{1}{12} \text{ ft})^2(1.84 \times 10^6 \text{ ft}^{-1})}{25} = 511 \text{ ft}$$

Now we can test the Reynolds number to see whether the formula applied:

$$\text{Re}_x = \frac{Ux}{\nu} = \frac{(20 \text{ ft/s})(511 \text{ ft})}{1.09 \times 10^{-5} \text{ ft}^2/\text{s}} = 9.4 \times 10^8$$

This is impossible since the maximum Re_x for laminar flow past a flat plate is 3×10^6. So we try again with Eq. (7.1*b*):

Turbulent flow:
$$\frac{\delta}{x} = \frac{0.16}{(Ux/\nu)^{1/7}}$$

or
$$x = \left[\frac{\delta(U/\nu)^{1/7}}{0.16}\right]^{7/6} = \left[\frac{(\frac{1}{12} \text{ ft})(1.84 \times 10^6 \text{ ft}^{-1})^{1/7}}{0.16}\right]^{7/6} = (4.09)^{7/6} = 5.17 \text{ ft} \qquad \textit{Ans.}$$

Test
$$\text{Re}_x = \frac{(20 \text{ ft/s})(5.17 \text{ ft})}{1.09 \times 10^{-5} \text{ ft}^2/\text{s}} = 9.5 \times 10^6$$

This is a perfectly proper turbulent-flow condition; hence we have found the correct position x on our second try.

7.2 Momentum-Integral Estimates

When we derived the momentum-integral relation, Eq. (3.37), and applied it to a flat-plate boundary layer in Example 3.11, we promised to consider it further in Chap. 7. Well, here we are! Let us review the problem, using Fig. 7.3.

A shear layer of unknown thickness grows along the sharp flat plate in Fig. 7.3. The no-slip wall condition retards the flow, making it into a rounded profile $u(y)$, which merges into the external velocity U = constant at a "thickness" $y = \delta(x)$. By utilizing the control volume of Fig. 3.11, we found (without making any assumptions about laminar versus turbulent flow) in Example 3.11 that the drag force on the plate is given by the following momentum integral across the exit plane

$$D(x) = \rho b \int_0^{\delta(x)} u(U - u)\, dy \tag{7.2}$$

where b is the plate width into the paper and the integration is carried out along a vertical plane x = constant. You should review the momentum-integral relation (3.37) and its use in Example 3.11.

Kármán's Analysis of the Flat Plate

Equation (7.2) was derived in 1921 by Kármán [7], who wrote it in the convenient form of the *momentum thickness* θ

$$D(x) = \rho b U^2 \theta \qquad \theta = \int_0^{\delta} \frac{u}{U}\left(1 - \frac{u}{U}\right) dy \tag{7.3}$$

Momentum thickness is thus a measure of total plate drag. Kármán then noted that the drag also equals the integrated wall shear stress along the plate

$$D(x) = b \int_0^x \tau_w(x)\, dx$$

or

$$\frac{dD}{dx} = b\tau_w \tag{7.4}$$

Meanwhile, the derivative of Eq. (7.3), with U = constant, is

$$\frac{dD}{dx} = \rho b U^2 \frac{d\theta}{dx}$$

By comparing this with Eq. (7.4) Kármán arrived at what is now called the *momentum-integral relation* for flat-plate boundary-layer flow

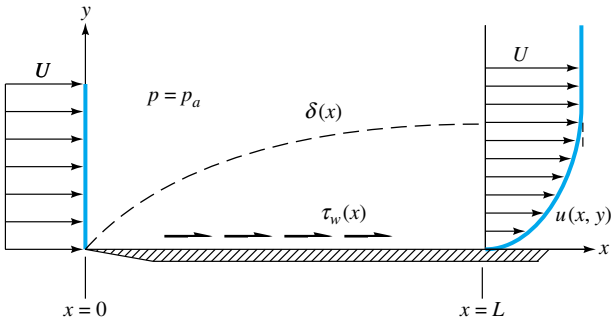

Fig. 7.3 Growth of a boundary layer on a flat plate.

$$\tau_w = \rho U^2 \frac{d\theta}{dx} \tag{7.5}$$

It is valid for either laminar or turbulent flat-plate flow.

To get a numerical result for laminar flow, Kármán assumed that the velocity profiles had an approximately parabolic shape

$$u(x, y) \approx U\left(\frac{2y}{\delta} - \frac{y^2}{\delta^2}\right) \qquad 0 \le y \le \delta(x) \tag{7.6}$$

which makes it possible to estimate both momentum thickness and wall shear

$$\theta = \int_0^\delta \left(\frac{2y}{\delta} - \frac{y^2}{\delta^2}\right)\left(1 - \frac{2y}{\delta} + \frac{y^2}{\delta^2}\right) dy \approx \frac{2}{15}\delta$$
$$\tau_w = \mu \left.\frac{\partial u}{\partial y}\right|_{y=0} \approx \frac{2\mu U}{\delta} \tag{7.7}$$

By substituting (7.7) into (7.5) and rearranging we obtain

$$\delta\, d\delta \approx 15 \frac{\nu}{U} dx \tag{7.8}$$

where $\nu = \mu/\rho$. We can integrate from 0 to x, assuming that $\delta = 0$ at $x = 0$, the leading edge

$$\frac{1}{2}\delta^2 = \frac{15\nu x}{U}$$

or

$$\frac{\delta}{x} \approx 5.5\left(\frac{\nu}{Ux}\right)^{1/2} = \frac{5.5}{\mathrm{Re}_x^{1/2}} \tag{7.9}$$

This is the desired thickness estimate. It is all approximate, of course, part of Kármán's *momentum-integral theory* [7], but it is startlingly accurate, being only 10 percent higher than the known exact solution for laminar flat-plate flow, which we gave as Eq. (7.1*a*).

By combining Eqs. (7.9) and (7.7) we also obtain a shear-stress estimate along the plate

$$c_f = \frac{2\tau_w}{\rho U^2} \approx \left(\frac{\frac{8}{15}}{\mathrm{Re}_x}\right)^{1/2} = \frac{0.73}{\mathrm{Re}_x^{1/2}} \tag{7.10}$$

Again this estimate, in spite of the crudeness of the profile assumption (7.6) is only 10 percent higher than the known exact laminar-plate-flow solution $c_f = 0.664/\mathrm{Re}_x^{1/2}$, treated in Sec. 7.4. The dimensionless quantity c_f, called the *skin-friction coefficient,* is analogous to the friction factor f in ducts.

A boundary layer can be judged as "thin" if, say, the ratio δ/x is less than about 0.1. This occurs at $\delta/x = 0.1 = 5.0/\mathrm{Re}_x^{1/2}$ or at $\mathrm{Re}_x = 2500$. For Re_x less than 2500 we can estimate that boundary-layer theory fails because the thick layer has a significant effect on the outer inviscid flow. The upper limit on Re_x for laminar flow is about 3×10^6, where measurements on a smooth flat plate [8] show that the flow undergoes transition to a turbulent boundary layer. From 3×10^6 upward the turbulent Reynolds number may be arbitrarily large, and a practical limit at present is 5×10^9 for oil supertankers.

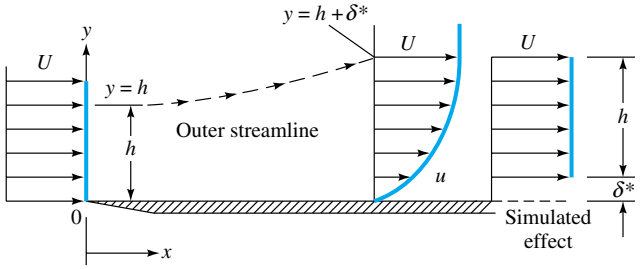

Fig. 7.4 Displacement effect of a boundary layer.

Displacement Thickness

Another interesting effect of a boundary layer is its small but finite displacement of the outer streamlines. As shown in Fig. 7.4, outer streamlines must deflect outward a distance $\delta^*(x)$ to satisfy conservation of mass between the inlet and outlet

$$\int_0^h \rho U b \, dy = \int_0^\delta \rho u b \, dy \qquad \delta = h + \delta^* \tag{7.11}$$

The quantity δ^* is called the *displacement thickness* of the boundary layer. To relate it to $u(y)$, cancel ρ and b from Eq. (7.11), evaluate the left integral, and slyly add and subtract U from the right integrand:

$$Uh = \int_0^\delta (U + u - U)\, dy = U(h + \delta^*) + \int_0^\delta (u - U)\, dy$$

or

$$\delta^* = \int_0^\delta \left(1 - \frac{u}{U}\right) dy \tag{7.12}$$

Thus the ratio of δ^*/δ varies only with the dimensionless velocity-profile shape u/U.

Introducing our profile approximation (7.6) into (7.12), we obtain by integration the approximate result

$$\delta^* \approx \frac{1}{3}\,\delta \qquad \frac{\delta^*}{x} \approx \frac{1.83}{\mathrm{Re}_x^{1/2}} \tag{7.13}$$

These estimates are only 6 percent away from the exact solutions for laminar flat-plate flow given in Sec. 7.4: $\delta^* = 0.344\delta = 1.721x/\mathrm{Re}_x^{1/2}$. Since δ^* is much smaller than x for large Re_x and the outer streamline slope V/U is proportional to δ^*, we conclude that the velocity normal to the wall is much smaller than the velocity parallel to the wall. This is a key assumption in boundary-layer theory (Sec. 7.3).

We also conclude from the success of these simple parabolic estimates that Kármán's momentum-integral theory is effective and useful. Many details of this theory are given in Refs. 1 to 3.

EXAMPLE 7.2

Are low-speed, small-scale air and water boundary layers really thin? Consider flow at $U = 1$ ft/s past a flat plate 1 ft long. Compute the boundary-layer thickness at the trailing edge for (*a*) air and (*b*) water at 20°C.

Solution

Part (a) From Table A.3, $\nu_{air} \approx 1.61$ E-4 ft^2/s. The trailing-edge Reynolds number thus is

$$\mathrm{Re}_L = \frac{UL}{\nu} = \frac{(1 \text{ ft/s})(1 \text{ ft})}{1.61 \text{ E-4 ft}^2/\text{s}} = 6200$$

Since this is less than 10^6, the flow is presumed laminar, and since it is greater than 2500, the boundary layer is reasonably thin. From Eq. (7.1*a*), the predicted laminar thickness is

$$\frac{\delta}{x} \approx \frac{5.0}{\sqrt{6200}} = 0.0634$$

or, at $x = 1$ ft, $\delta = 0.0634$ ft ≈ 0.76 in *Ans. (a)*

Part (b) From Table A.2 $\nu_{water} \approx 1.08$ E-5 ft^2/s. The trailing-edge Reynolds number is

$$\mathrm{Re}_L = \frac{(1 \text{ ft/s})(1 \text{ ft})}{1.08 \text{ E-5 ft}^2/\text{s}} \approx 92{,}600$$

This again satisfies the laminar and thinness conditions. The boundary-layer thickness is

$$\frac{\delta}{x} \approx \frac{5.0}{\sqrt{92{,}600}} = 0.0164$$

or, at $x = 1$ ft, $\delta = 0.0164$ ft ≈ 0.20 in *Ans. (b)*

Thus, even at such low velocities and short lengths, both airflows and water flows satisfy the boundary-layer approximations.

7.3 The Boundary-Layer Equations

In Chaps. 4 and 6 we learned that there are several dozen known analytical laminar-flow solutions [1 to 3]. None are for external flow around immersed bodies, although this is one of the primary applications of fluid mechanics. No exact solutions are known for turbulent flow, whose analysis typically uses empirical modeling laws to relate time-mean variables.

There are presently three techniques used to study external flows: (1) numerical (digital-computer) solutions, (2) experimentation, and (3) boundary-layer theory.

Computational fluid dynamics (CFD) is now well developed and described in advanced texts such as that by Anderson et al. [4]. Thousands of computer solutions and models have been published; execution times, mesh sizes, and graphical presentations are improving each year. Both laminar- and turbulent-flow solutions have been published, and turbulence modeling is a current research topic [9]. Except for a brief discussion of computer analysis in Chap. 8, the topic of CFD is beyond our scope here.

Experimentation is the most common method of studying external flows. Chapter 5 outlined the technique of dimensional analysis, and we shall give many nondimensional experimental data for external flows in Sec. 7.6.

The third tool is boundary-layer theory, first formulated by Ludwig Prandtl in 1904. We shall follow Prandtl's ideas here and make certain order-of-magnitude assumptions to greatly simplify the Navier-Stokes equations (4.38) into boundary-layer equations which are solved relatively easily and patched onto the outer inviscid-flow field.

One of the great achievements of boundary-layer theory is its ability to predict the flow separation illustrated in Fig. 7.2*b*. Before 1904 no one realized that such thin shear layers could cause such a gross effect as flow separation. Unfortunately, even today theory cannot accurately predict the behavior of the separated-flow region and its interaction with the outer layer. This is the weakness of boundary-layer theory, which we hope will be overcome by intensive research into the dynamics of separated flows [6].

Derivation for Two-Dimensional Flow

We consider only steady two-dimensional incompressible viscous flow with the x direction along the wall and y normal to the wall, as in Fig. 7.3.[1] We neglect gravity, which is important only in boundary layers where fluid buoyancy is dominant [2, sec. 4.13]. From Chap. 4, the complete equations of motion consist of continuity and the x- and y-momentum relations

$$\frac{\partial u}{\partial x} + \frac{\partial v}{\partial y} = 0 \tag{7.14a}$$

$$\rho\left(u\frac{\partial u}{\partial x} + v\frac{\partial u}{\partial y}\right) = -\frac{\partial p}{\partial x} + \mu\left(\frac{\partial^2 u}{\partial x^2} + \frac{\partial^2 u}{\partial y^2}\right) \tag{7.14b}$$

$$\rho\left(u\frac{\partial v}{\partial x} + v\frac{\partial v}{\partial y}\right) = -\frac{\partial p}{\partial y} + \mu\left(\frac{\partial^2 v}{\partial x^2} + \frac{\partial^2 v}{\partial y^2}\right) \tag{7.14c}$$

These should be solved for u, v, and p subject to typical no-slip, inlet, and exit boundary conditions, but in fact they are too difficult to handle for most external flows.

In 1904 Prandtl correctly deduced that a shear layer must be very thin if the Reynolds number is large, so that the following approximations apply:

Velocities: $$v \ll u \tag{7.15a}$$

Rates of change: $$\frac{\partial u}{\partial x} \ll \frac{\partial u}{\partial y} \qquad \frac{\partial v}{\partial x} \ll \frac{\partial v}{\partial y} \tag{7.15b}$$

Our discussion of displacement thickness in the previous section was intended to justify these assumptions.

Applying these approximations to Eq. (7.14*c*) results in a powerful simplification

$$\frac{\partial p}{\partial y} \approx 0 \qquad \text{or} \qquad p \approx p(x) \text{ only} \tag{7.16}$$

In other words, the y-momentum equation can be neglected entirely, and the pressure varies only *along* the boundary layer, not through it. The pressure-gradient term in Eq. (7.14*b*) is assumed to be known in advance from Bernoulli's equation applied to the outer inviscid flow

$$\frac{\partial p}{\partial x} = \frac{dp}{dx} = -\rho U\frac{dU}{dx} \tag{7.17}$$

[1]For a curved wall, x can represent the arc length along the wall and y can be everywhere normal to x with negligible change in the boundary-layer equations as long as the radius of curvature of the wall is large compared with the boundary-layer thickness [1 to 3].

Presumably we have already made the inviscid analysis and know the distribution of $U(x)$ along the wall (Chap. 8).

Meanwhile, one term in Eq. (7.14*b*) is negligible due to Eqs. (7.15)

$$\frac{\partial^2 u}{\partial x^2} \ll \frac{\partial^2 u}{\partial y^2} \tag{7.18}$$

However, neither term in the continuity relation (7.14*a*) can be neglected—another warning that continuity is always a vital part of any fluid-flow analysis.

The net result is that the three full equations of motion (7.14) are reduced to Prandtl's two boundary-layer equations

Continuity: $$\frac{\partial u}{\partial x} + \frac{\partial v}{\partial y} = 0 \tag{7.19a}$$

Momentum along wall: $$u\frac{\partial u}{\partial x} + v\frac{\partial u}{\partial y} \approx U\frac{dU}{dx} + \frac{1}{\rho}\frac{\partial \tau}{\partial y} \tag{7.19b}$$

where $$\tau = \begin{cases} \mu \dfrac{\partial u}{\partial y} & \text{laminar flow} \\ \mu \dfrac{\partial u}{\partial y} - \rho\overline{u'v'} & \text{turbulent flow} \end{cases}$$

These are to be solved for $u(x, y)$ and $v(x, y)$, with $U(x)$ assumed to be a known function from the outer inviscid-flow analysis. There are two boundary conditions on u and one on v:

At $y = 0$ (wall): $u = v = 0$ (no slip) (7.20*a*)

At $y = \delta(x)$ (outer stream): $u = U(x)$ (patching) (7.20*b*)

Unlike the Navier-Stokes equations (7.14), which are mathematically elliptic and must be solved simultaneously over the entire flow field, the boundary-layer equations (7.19) are mathematically parabolic and are solved by beginning at the leading edge and marching downstream as far as you like, stopping at the separation point or earlier if you prefer.[2]

The boundary-layer equations have been solved for scores of interesting cases of internal and external flow for both laminar and turbulent flow, utilizing the inviscid distribution $U(x)$ appropriate to each flow. Full details of boundary-layer theory and results and comparison with experiment are given in Refs. 1 to 3. Here we shall confine ourselves primarily to flat-plate solutions (Sec. 7.4).

7.4 The Flat-Plate Boundary Layer

The classic and most often used solution of boundary-layer theory is for flat-plate flow, as in Fig. 7.3, which can represent either laminar or turbulent flow.

[2]For further mathematical details, see Ref. 2, sec. 2.8.

Laminar Flow

For laminar flow past the plate, the boundary-layer equations (7.19) can be solved exactly for u and v, assuming that the free-stream velocity U is constant ($dU/dx = 0$). The solution was given by Prandtl's student Blasius, in his 1908 dissertation from Göttingen. With an ingenious coordinate transformation, Blasius showed that the dimensionless velocity profile u/U is a function only of the single composite dimensionless variable $(y)[U/(\nu x)]^{1/2}$:

$$\frac{u}{U} = f'(\eta) \qquad \eta = y\left(\frac{U}{\nu x}\right)^{1/2} \tag{7.21}$$

where the prime denotes differentiation with respect to η. Substitution of (7.21) into the boundary-layer equations (7.19) reduces the problem, after much algebra, to a single third-order nonlinear ordinary differential equation for f

$$f''' + \tfrac{1}{2} f f'' = 0 \tag{7.22}$$

The boundary conditions (7.20) become

At $y = 0$: $$f(0) = f'(0) = 0 \tag{7.23a}$$

As $y \to \infty$: $$f'(\infty) \to 1.0 \tag{7.23b}$$

This is the *Blasius equation,* for which accurate solutions have been obtained only by numerical integration. Some tabulated values of the velocity-profile shape $f'(\eta) = u/U$ are given in Table 7.1.

Since u/U approaches 1.0 only as $y \to \infty$, it is customary to select the boundary-layer thickness δ as that point where $u/U = 0.99$. From the table, this occurs at $\eta \approx 5.0$:

$$\delta_{99\%}\left(\frac{U}{\nu x}\right)^{1/2} \approx 5.0$$

or

$$\frac{\delta}{x} \approx \frac{5.0}{\mathrm{Re}_x^{1/2}} \qquad \text{Blasius (1908)} \tag{7.24}$$

Table 7.1 The Blasius Velocity Profile [1 to 3]

$y[U/(\nu x)]^{1/2}$	u/U	$y[U/(\nu x)]^{1/2}$	u/U
0.0	0.0	2.8	0.81152
0.2	0.06641	3.0	0.84605
0.4	0.13277	3.2	0.87609
0.6	0.19894	3.4	0.90177
0.8	0.26471	3.6	0.92333
1.0	0.32979	3.8	0.94112
1.2	0.39378	4.0	0.95552
1.4	0.45627	4.2	0.96696
1.6	0.51676	4.4	0.97587
1.8	0.57477	4.6	0.98269
2.0	0.62977	4.8	0.98779
2.2	0.68132	5.0	0.99155
2.4	0.72899	∞	1.00000
2.6	0.77246		

With the profile known, Blasius, of course, could also compute the wall shear and displacement thickness

$$c_f = \frac{0.664}{\mathrm{Re}_x^{1/2}} \qquad \frac{\delta^*}{x} = \frac{1.721}{\mathrm{Re}_x^{1/2}} \tag{7.25}$$

Notice how close these are to our integral estimates, Eqs. (7.9), (7.10), and (7.13). When c_f is converted to dimensional form, we have

$$\tau_w(x) = \frac{0.332\rho^{1/2}\mu^{1/2}U^{1.5}}{x^{1/2}}$$

The wall shear drops off with $x^{1/2}$ because of boundary-layer growth and varies as velocity to the 1.5 power. This is in contrast to laminar pipe flow, where $\tau_w \propto U$ and is independent of x.

If $\tau_w(x)$ is substituted into Eq. (7.4), we compute the total drag force

$$D(x) = b\int_0^x \tau_w(x)\,dx = 0.664b\rho^{1/2}\mu^{1/2}U^{1.5}x^{1/2} \tag{7.26}$$

The drag increases only as the square root of the plate length. The nondimensional *drag coefficient* is defined as

$$C_D = \frac{2D(L)}{\rho U^2 bL} = \frac{1.328}{\mathrm{Re}_L^{1/2}} = 2c_f(L) \tag{7.27}$$

Thus, for laminar plate flow, C_D equals twice the value of the skin-friction coefficient at the trailing edge. This is the drag on one side of the plate.

Kármán pointed out that the drag could also be computed from the momentum relation (7.2). In dimensionless form, Eq. (7.2) becomes

$$C_D = \frac{2}{L}\int_0^\delta \frac{u}{U}\left(1 - \frac{u}{U}\right)dy \tag{7.28}$$

This can be rewritten in terms of the momentum thickness at the trailing edge

$$C_D = \frac{2\theta(L)}{L} \tag{7.29}$$

Computation of θ from the profile u/U or from C_D gives

$$\frac{\theta}{x} = \frac{0.664}{\mathrm{Re}_x^{1/2}} \qquad \text{laminar flat plate} \tag{7.30}$$

Since δ is so ill defined, the momentum thickness, being definite, is often used to correlate data taken for a variety of boundary layers under differing conditions. The ratio of displacement to momentum thickness, called the dimensionless-profile *shape factor,* is also useful in integral theories. For laminar flat-plate flow

$$H = \frac{\delta^*}{\theta} = \frac{1.721}{0.664} = 2.59 \tag{7.31}$$

A large shape factor then implies that boundary-layer separation is about to occur.

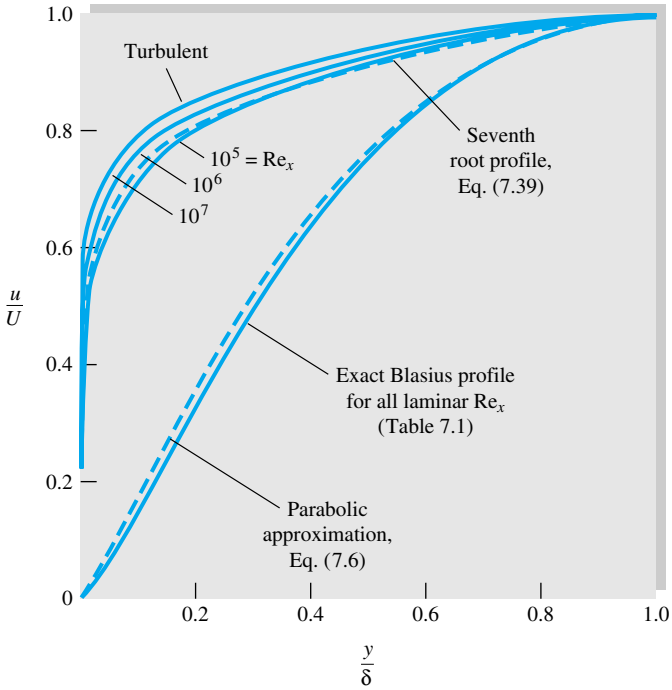

Fig. 7.5 Comparison of dimensionless laminar and turbulent flat-plate velocity profiles.

If we plot the Blasius velocity profile from Table 7.1 in the form of u/U versus y/δ, we can see why the simple integral-theory guess, Eq. (7.6), was such a great success. This is done in Fig. 7.5. The simple parabolic approximation is not far from the true Blasius profile; hence its momentum thickness is within 10 percent of the true value. Also shown in Fig. 7.5 are three typical turbulent flat-plate velocity profiles. Notice how strikingly different in shape they are from the laminar profiles. Instead of decreasing monotonically to zero, the turbulent profiles are very flat and then drop off sharply at the wall. As you might guess, they follow the logarithmic-law shape and thus can be analyzed by momentum-integral theory if this shape is properly represented.

Transition to Turbulence

The laminar flat-plate boundary layer eventually becomes turbulent, but there is no unique value for this change to occur. With care in polishing the wall and keeping the free stream quiet, one can delay the transition Reynolds number to $\mathrm{Re}_{x,\mathrm{tr}} \approx 3$ E6 [8]. However, for typical commercial surfaces and gusty free streams, a more realistic value is $\mathrm{Re}_{x,\mathrm{tr}} \approx 5$ E5.

EXAMPLE 7.3

A sharp flat plate with $L = 1$ m and $b = 3$ m is immersed parallel to a stream of velocity 2 m/s. Find the drag on one side of the plate, and at the trailing edge find the thicknesses δ, δ^*, and θ for (*a*) air, $\rho = 1.23$ kg/m^3 and $\nu = 1.46 \times 10^{-5}$ m^2/s, and (*b*) water, $\rho = 1000$ kg/m^3 and $\nu = 1.02 \times 10^{-6}$ m^2/s.

Solution

Part (a) The airflow Reynolds number is

$$\frac{VL}{\nu} = \frac{(2.0 \text{ m/s})(1.0 \text{ m})}{1.46 \times 10^{-5} \text{ m}^2/\text{s}} = 137{,}000$$

Since this is less than 3×10^6, we assume that the boundary layer is laminar. From Eq. (7.27), the drag coefficient is

$$C_D = \frac{1.328}{(137{,}000)^{1/2}} = 0.00359$$

Thus the drag on one side in the airflow is

$$D = C_D \tfrac{1}{2}\rho U^2 bL = 0.00359(\tfrac{1}{2})(1.23)(2.0)^2(3.0)(1.0) = 0.0265 \text{ N} \quad \textit{Ans. (a)}$$

The boundary-layer thickness at the end of the plate is

$$\frac{\delta}{L} = \frac{5.0}{\text{Re}_L^{1/2}} = \frac{5.0}{(137{,}000)^{1/2}} = 0.0135$$

or

$$\delta = 0.0135(1.0) = 0.0135 \text{ m} = 13.5 \text{ mm} \quad \textit{Ans. (a)}$$

We find the other two thicknesses simply by ratios:

$$\delta^* = \frac{1.721}{5.0}\,\delta = 4.65 \text{ mm} \qquad \theta = \frac{\delta^*}{2.59} = 1.79 \text{ mm} \quad \textit{Ans. (a)}$$

Notice that no conversion factors are needed with SI units.

Part (b) The water Reynolds number is

$$\text{Re}_L = \frac{2.0(1.0)}{1.02 \times 10^{-6}} = 1.96 \times 10^6$$

This is rather close to the critical value of 3×10^6, so that a rough surface or noisy free stream might trigger transition to turbulence; but let us assume that the flow is laminar. The water drag coefficient is

$$C_D = \frac{1.328}{(1.96 \times 10^6)^{1/2}} = 0.000949$$

and

$$D = 0.000949(\tfrac{1}{2})(1000)(2.0)^2(3.0)(1.0) = 5.70 \text{ N} \quad \textit{Ans. (b)}$$

The drag is 215 times more for water in spite of the higher Reynolds number and lower drag coefficient because water is 57 times more viscous and 813 times denser than air. From Eq. (7.26), in laminar flow, it should have $(57)^{1/2}(813)^{1/2} = 7.53(28.5) = 215$ times more drag.

The boundary-layer thickness is given by

$$\frac{\delta}{L} = \frac{5.0}{(1.96 \times 10^6)^{1/2}} = 0.00357$$

or

$$\delta = 0.00357(1000 \text{ mm}) = 3.57 \text{ mm} \quad \textit{Ans. (b)}$$

By scaling down we have

$$\delta^* = \frac{1.721}{5.0}\,\delta = 1.23 \text{ mm} \qquad \theta = \frac{\delta^*}{2.59} = 0.48 \text{ mm} \qquad \textit{Ans. (b)}$$

The water layer is 3.8 times thinner than the air layer, which reflects the square root of the 14.3 ratio of air to water kinematic viscosity.

Turbulent Flow

There is no exact theory for turbulent flat-plate flow, although there are many elegant computer solutions of the boundary-layer equations using various empirical models for the turbulent eddy viscosity [9]. The most widely accepted result is simply an integal analysis similar to our study of the laminar-profile approximation (7.6).

We begin with Eq. (7.5), which is valid for laminar or turbulent flow. We write it here for convenient reference:

$$\tau_w(x) = \rho U^2 \frac{d\theta}{dx} \tag{7.32}$$

From the definition of c_f, Eq. (7.10), this can be rewritten as

$$c_f = 2\frac{d\theta}{dx} \tag{7.33}$$

Now recall from Fig. 7.5 that the turbulent profiles are nowhere near parabolic. Going back to Fig. 6.9, we see that flat-plate flow is very nearly logarithmic, with a slight outer wake and a thin viscous sublayer. Therefore, just as in turbulent pipe flow, we assume that the logarithmic law (6.21) holds all the way across the boundary layer

$$\frac{u}{u^*} \approx \frac{1}{\kappa}\ln\frac{yu^*}{\nu} + B \qquad u^* = \left(\frac{\tau_w}{\rho}\right)^{1/2} \tag{7.34}$$

with, as usual, $\kappa = 0.41$ and $B = 5.0$. At the outer edge of the boundary layer, $y = \delta$ and $u = U$, and Eq. (7.34) becomes

$$\frac{U}{u^*} = \frac{1}{\kappa}\ln\frac{\delta u^*}{\nu} + B \tag{7.35}$$

But the definition of the skin-friction coefficient, Eq. (7.10), is such that the following identities hold:

$$\frac{U}{u^*} \equiv \left(\frac{2}{c_f}\right)^{1/2} \qquad \frac{\delta u^*}{\nu} \equiv \mathrm{Re}_\delta\left(\frac{c_f}{2}\right)^{1/2} \tag{7.36}$$

Therefore Eq. (7.35) is a *skin-friction law* for turbulent flat-plate flow

$$\left(\frac{2}{c_f}\right)^{1/2} \approx 2.44\ln\left[\mathrm{Re}_\delta\left(\frac{c_f}{2}\right)^{1/2}\right] + 5.0 \tag{7.37}$$

It is a complicated law, but we can at least solve for a few values and list them:

Re_δ	10^4	10^5	10^6	10^7
c_f	0.00493	0.00315	0.00217	0.00158

Following a suggestion of Prandtl, we can forget the complex log friction law (7.37) and simply fit the numbers in the table to a power-law approximation

$$c_f \approx 0.02\ \mathrm{Re}_\delta^{-1/6} \tag{7.38}$$

This we shall use as the left-hand side of Eq. (7.33). For the right-hand side, we need an estimate for $\theta(x)$ in terms of $\delta(x)$. If we use the logarithmic-law profile (7.34), we shall be up to our hips in logarithmic integrations for the momentum thickness. Instead we follow another suggestion of Prandtl, who pointed out that the turbulent profiles in Fig. 7.5 can be approximated by a one-seventh-power law

$$\left(\frac{u}{U}\right)_{\text{turb}} \approx \left(\frac{y}{\delta}\right)^{1/7} \tag{7.39}$$

This is shown as a dashed line in Fig. 7.5. It is an excellent fit to the low-Reynolds-number turbulent data, which were all that were available to Prandtl at the time. With this simple approximation, the momentum thickness (7.28) can easily be evaluated:

$$\theta \approx \int_0^\delta \left(\frac{y}{\delta}\right)^{1/7}\left[1 - \left(\frac{y}{\delta}\right)^{1/7}\right] dy = \frac{7}{72}\,\delta \tag{7.40}$$

We accept this result and substitute Eqs. (7.38) and (7.40) into Kármán's momentum law (7.33)

$$c_f = 0.02\ \mathrm{Re}_\delta^{-1/6} = 2\,\frac{d}{dx}\left(\frac{7}{72}\,\delta\right)$$

or

$$\mathrm{Re}_\delta^{-1/6} = 9.72\,\frac{d\delta}{dx} = 9.72\,\frac{d(\mathrm{Re}\delta)}{d(\mathrm{Re}_x)} \tag{7.41}$$

Separate the variables and integrate, assuming $\delta = 0$ at $x = 0$:

$$\mathrm{Re}_\delta \approx 0.16\ \mathrm{Re}_x^{6/7} \qquad \text{or} \qquad \frac{\delta}{x} \approx \frac{0.16}{\mathrm{Re}_x^{1/7}} \tag{7.42}$$

Thus the thickness of a turbulent boundary layer increases as $x^{6/7}$, far more rapidly than the laminar increase $x^{1/2}$. Equation (7.42) is the solution to the problem, because all other parameters are now available. For example, combining Eqs. (7.42) and (7.38), we obtain the friction variation

$$c_f \approx \frac{0.027}{\mathrm{Re}_x^{1/7}} \tag{7.43}$$

Writing this out in dimensional form, we have

$$\tau_{w,\text{turb}} \approx \frac{0.0135\mu^{1/7}\rho^{6/7}U^{13/7}}{x^{1/7}} \tag{7.44}$$

Turbulent plate friction drops slowly with x, increases nearly as ρ and U^2, and is rather insensitive to viscosity.

We can evaluate the drag coefficient from Eq. (7.29)

$$C_D = \frac{0.031}{\mathrm{Re}_L^{1/7}} = \frac{7}{6}\,c_f(L) \tag{7.45}$$

Then C_D is only 16 percent greater than the trailing-edge skin friction [compare with Eq. (7.27) for laminar flow].

The displacement thickness can be estimated from the one-seventh-power law and Eq. (7.12):

$$\delta^* \approx \int_0^\delta \left[1 - \left(\frac{y}{\delta}\right)^{1/7}\right] dy = \frac{1}{8}\,\delta \tag{7.46}$$

The turbulent flat-plate shape factor is approximately

$$H = \frac{\delta^*}{\theta} = \frac{\frac{1}{8}}{\frac{7}{72}} = 1.3 \tag{7.47}$$

These are the basic results of turbulent flat-plate theory.

Figure 7.6 shows flat-plate drag coefficients for both laminar-and turbulent-flow conditions. The smooth-wall relations (7.27) and (7.45) are shown, along with the effect of wall roughness, which is quite strong. The proper roughness parameter here is x/ϵ or L/ϵ, by analogy with the pipe parameter ϵ/d. In the fully rough regime, C_D is independent of the Reynolds number, so that the drag varies exactly as U^2 and is inde-

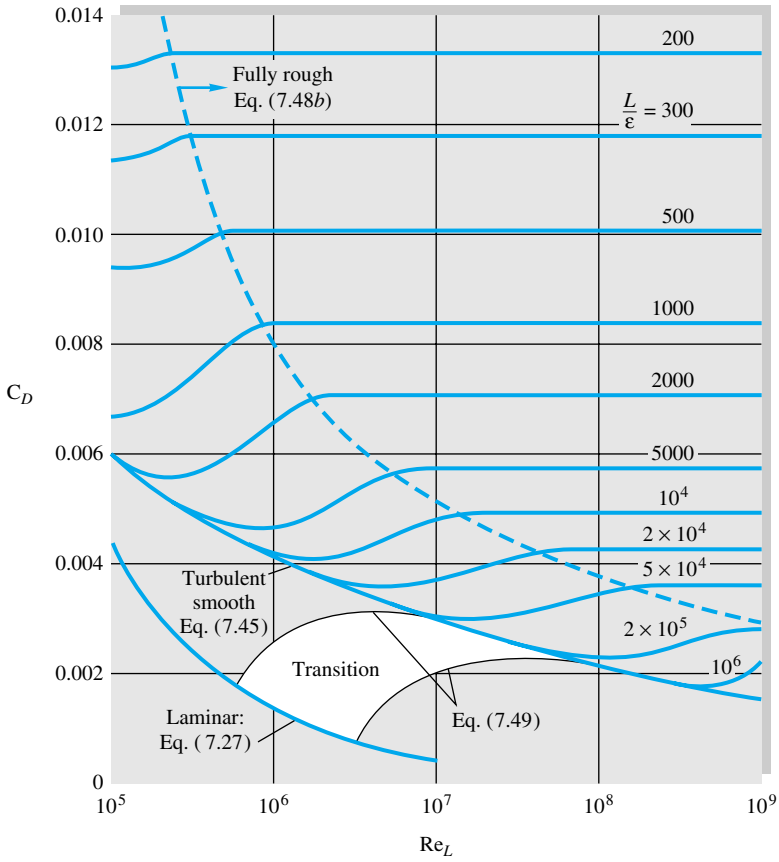

Fig. 7.6 Drag coefficient of laminar and turbulent boundary layers on smooth and rough flat plates. This chart is the flat-plate analog of the Moody diagram of Fig. 6.13.

pendent of μ. Reference 2 presents a theory of rough flat-plate flow, and Ref. 1 gives a curve fit for skin friction and drag in the fully rough regime:

$$c_f \approx \left(2.87 + 1.58 \log \frac{x}{\epsilon}\right)^{-2.5} \tag{7.48a}$$

$$C_D \approx \left(1.89 + 1.62 \log \frac{L}{\epsilon}\right)^{-2.5} \tag{7.48b}$$

Equation (7.48*b*) is plotted to the right of the dashed line in Fig. 7.6. The figure also shows the behavior of the drag coefficient in the transition region $5 \times 10^5 < \mathrm{Re}_L < 8 \times 10^7$, where the laminar drag at the leading edge is an appreciable fraction of the total drag. Schlichting [1] suggests the following curve fits for these transition drag curves depending upon the Reynolds number $\mathrm{Re}_{\mathrm{trans}}$ where transition begins:

$$C_D \approx \begin{cases} \dfrac{0.031}{\mathrm{Re}_L^{1/7}} - \dfrac{1440}{\mathrm{Re}_L} & \mathrm{Re}_{\mathrm{trans}} = 5 \times 10^5 \quad (7.49a) \\ \dfrac{0.031}{\mathrm{Re}_L^{1/7}} - \dfrac{8700}{\mathrm{Re}_L} & \mathrm{Re}_{\mathrm{trans}} = 3 \times 10^6 \quad (7.49b) \end{cases}$$

EXAMPLE 7.4

A hydrofoil 1.2 ft long and 6 ft wide is placed in a water flow of 40 ft/s, with $\rho = 1.99$ slugs/ft^3 and $\nu = 0.000011$ ft^2/s. (*a*) Estimate the boundary-layer thickness at the end of the plate. Estimate the friction drag for (*b*) turbulent smooth-wall flow from the leading edge, (*c*) laminar turbulent flow with $\mathrm{Re}_{\mathrm{trans}} = 5 \times 10^5$, and (*d*) turbulent rough-wall flow with $\epsilon = 0.0004$ ft.

Solution

Part (a) The Reynolds number is

$$\mathrm{Re}_L = \frac{UL}{\nu} = \frac{(40 \text{ ft/s})(1.2 \text{ ft})}{0.000011 \text{ ft}^2/\text{s}} = 4.36 \times 10^6$$

Thus the trailing-edge flow is certainly turbulent. The maximum boundary-layer thickness would occur for turbulent flow starting at the leading edge. From Eq. (7.42),

$$\frac{\delta(L)}{L} = \frac{0.16}{(4.36 \times 10^6)^{1/7}} = 0.018$$

or

$$\delta = 0.018(1.2 \text{ ft}) = 0.0216 \text{ ft} \qquad \textit{Ans. (a)}$$

This is 7.5 times thicker than a fully laminar boundary layer at the same Reynolds number.

Part (b) For fully turbulent smooth-wall flow, the drag coefficient on one side of the plate is, from Eq. (7.45),

$$C_D = \frac{0.031}{(4.36 \times 10^6)^{1/7}} = 0.00349$$

Then the drag on both sides of the foil is approximately

$$D = 2C_D(\tfrac{1}{2}\rho U^2)bL = 2(0.00349)(\tfrac{1}{2})(1.99)(40)^2(6.0)(1.2) = 80 \text{ lb} \qquad \textit{Ans. (b)}$$

Part (c) With a laminar leading edge and $\text{Re}_{\text{trans}} = 5 \times 10^5$, Eq. (7.49*a*) applies:

$$C_D = 0.00349 - \frac{1440}{4.36 \times 10^6} = 0.00316$$

The drag can be recomputed for this lower drag coefficient:

$$D = 2C_D(\tfrac{1}{2}\rho U^2)bL = 72 \text{ lbf} \qquad \textit{Ans. (c)}$$

Part (d) Finally, for the rough wall, we calculate

$$\frac{L}{\epsilon} = \frac{1.2 \text{ ft}}{0.0004 \text{ ft}} = 3000$$

From Fig. 7.6 at $\text{Re}_L = 4.36 \times 10^6$, this condition is just inside the fully rough regime. Equation (7.48*b*) applies:

$$C_D = (1.89 + 1.62 \log 3000)^{-2.5} = 0.00644$$

and the drag estimate is

$$D = 2C_D(\tfrac{1}{2}\rho U^2)bL = 148 \text{ lbf} \qquad \textit{Ans. (d)}$$

This small roughness nearly doubles the drag. It is probable that the total hydrofoil drag is still another factor of 2 larger because of trailing-edge flow-separation effects.

7.5 Boundary Layers with Pressure Gradient[3]

The flat-plate analysis of the previous section should give us a good feeling for the behavior of both laminar and turbulent boundary layers, except for one important effect: flow separation. Prandtl showed that separation like that in Fig. 7.2*b* is caused by excessive momentum loss near the wall in a boundary layer trying to move downstream against increasing pressure, $dp/dx > 0$, which is called an *adverse pressure gradient*. The opposite case of decreasing pressure, $dp/dx < 0$, is called a *favorable gradient,* where flow separation can never occur. In a typical immersed-body flow, e.g., Fig. 7.2*b*, the favorable gradient is on the front of the body and the adverse gradient is in the rear, as discussed in detail in Chap. 8.

We can explain flow separation with a geometric argument about the second derivative of velocity u at the wall. From the momentum equation (7.19*b*) at the wall, where $u = v = 0$, we obtain

$$\left.\frac{\partial \tau}{\partial y}\right|_{\text{wall}} = \mu \left.\frac{\partial^2 u}{\partial y^2}\right|_{\text{wall}} = -\rho U \frac{dU}{dx} = \frac{dp}{dx}$$

or

$$\left.\frac{\partial^2 u}{\partial y^2}\right|_{\text{wall}} = \frac{1}{\mu}\frac{dp}{dx} \tag{7.50}$$

[3]This section may be omitted without loss of continuity.

for either laminar or turbulent flow. Thus in an adverse gradient the second derivative of velocity is positive at the wall; yet it must be negative at the outer layer ($y = \delta$) to merge smoothly with the mainstream flow $U(x)$. It follows that the second derivative must pass through zero somewhere in between, at a point of inflection, and any boundary-layer profile in an adverse gradient must exhibit a characteristic S shape.

Figure 7.7 illustrates the general case. In a favorable gradient (Fig. 7.7*a*) the profile

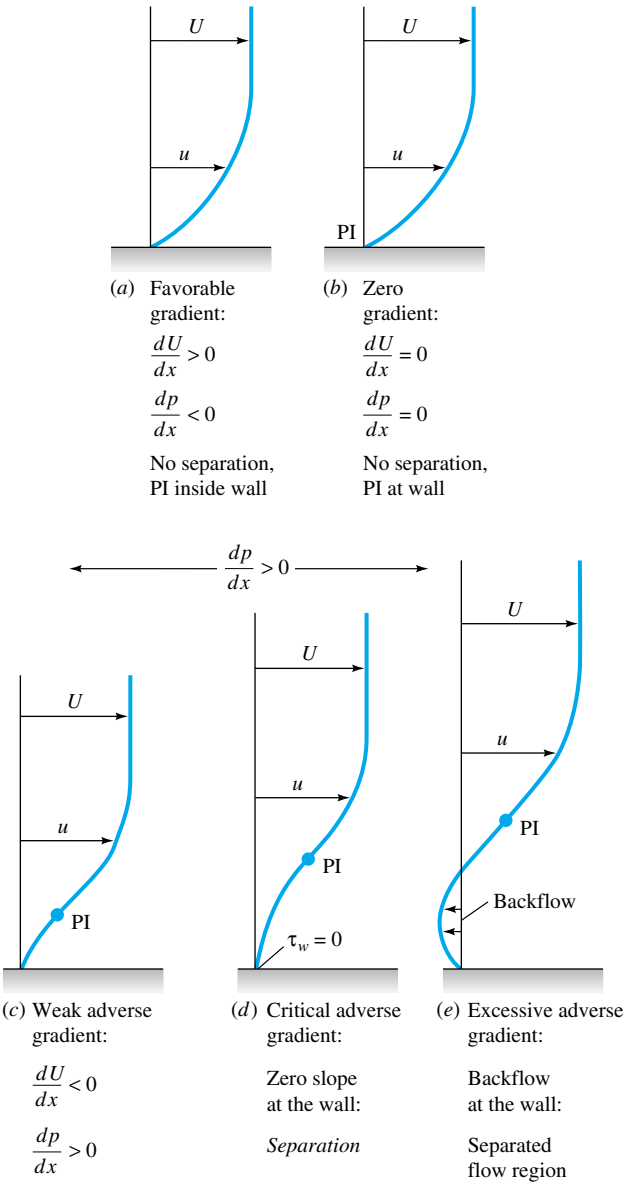

Fig. 7.7 Effect of pressure gradient on boundary-layer profiles; PI = point of inflection.

is very rounded, there is no point of inflection, there can be no separation, and laminar profiles of this type are very resistant to a transition to turbulence [1 to 3].

In a zero pressure gradient (Fig. 7.7*b*), e.g., flat-plate flow, the point of inflection is at the wall itself. There can be no separation, and the flow will undergo transition at Re_x no greater than about 3×10^6, as discussed earlier.

In an adverse gradient (Fig. 7.7*c* to *e*), a point of inflection (PI) occurs in the boundary layer, its distance from the wall increasing with the strength of the adverse gradient. For a weak gradient (Fig. 7.7*c*) the flow does not actually separate, but it is vulnerable to transition to turbulence at Re_x as low as 10^5 [1, 2]. At a moderate gradient, a critical condition (Fig. 7.7*d*) is reached where the wall shear is exactly zero ($\partial u/\partial y = 0$). This is defined as the *separation point* ($\tau_w = 0$), because any stronger gradient will actually cause backflow at the wall (Fig. 7.7*e*): the boundary layer thickens greatly, and the main flow breaks away, or separates, from the wall (Fig. 7.2*b*).

The flow profiles of Fig. 7.7 usually occur in sequence as the boundary layer progresses along the wall of a body. For example, in Fig. 7.2*a*, a favorable gradient occurs on the front of the body, zero pressure gradient occurs just upstream of the shoulder, and an adverse gradient occurs successively as we move around the rear of the body.

A second practical example is the flow in a duct consisting of a nozzle, throat, and diffuser, as in Fig. 7.8. The nozzle flow is a favorable gradient and never separates, nor

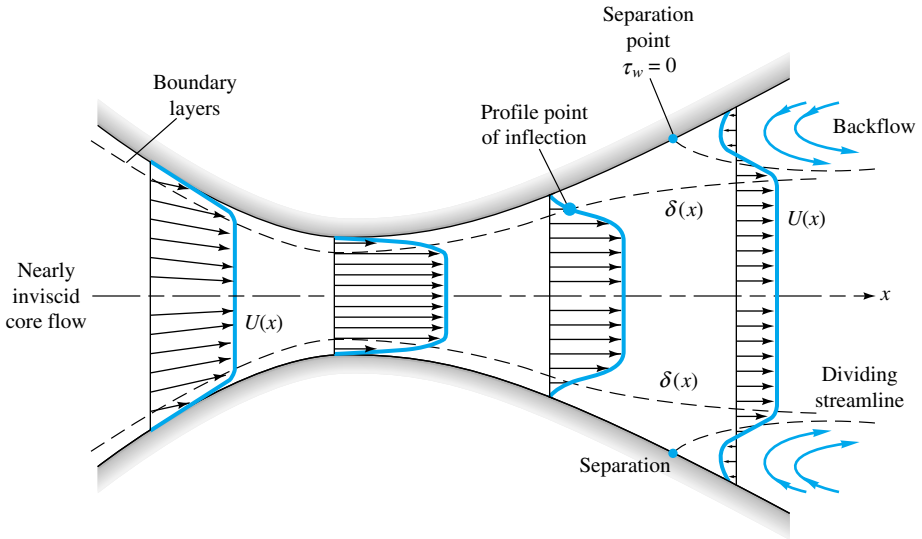

Fig. 7.8 Boundary-layer growth and separation in a nozzle-diffuser configuration.

does the throat flow where the pressure gradient is approximately zero. But the expanding-area diffuser produces low velocity and increasing pressure, an adverse gradient. If the diffuser angle is too large, the adverse gradient is excessive, and the boundary layer will separate at one or both walls, with backflow, increased losses, and poor pressure recovery. In the diffuser literature [10] this condition is called *diffuser stall,* a term used also in airfoil aerodynamics (Sec. 7.6) to denote airfoil boundary-layer separation. Thus the boundary-layer behavior explains why a large-angle diffuser has heavy flow losses (Fig. 6.23) and poor performance (Fig. 6.28).

Presently boundary-layer theory can compute only up to the separation point, after which it is invalid. New techniques are now developed for analyzing the strong interaction effects caused by separated flows [5, 6].

Laminar Integral Theory

Both laminar and turbulent theories can be developed from Kármán's general two-dimensional boundary-layer integral relation [7], which extends Eq. (7.33) to variable $U(x)$

$$\frac{\tau_w}{\rho U^2} = \frac{1}{2} c_f = \frac{d\theta}{dx} + (2 + H) \frac{\theta}{U} \frac{dU}{dx} \tag{7.51}$$

where $\theta(x)$ is the momentum thickness and $H(x) = \delta^*(x)/\theta(x)$ is the shape factor. From Eq. (7.17) negative dU/dx is equivalent to positive dp/dx, that is, an adverse gradient.

We can integrate Eq. (7.51) to determine $\theta(x)$ for a given $U(x)$ if we correlate c_f and H with the momentum thickness. This has been done by examining typical velocity profiles of laminar and turbulent boundary-layer flows for various pressure gradients. Some examples are given in Fig. 7.9, showing that the shape factor H is a good indicator of the pressure gradient. The higher the H, the stronger the adverse gradient, and separation occurs approximately at

$$H \approx \begin{cases} 3.5 & \text{laminar flow} \\ 2.4 & \text{turbulent flow} \end{cases} \tag{7.52}$$

The laminar profiles (Fig. 7.9*a*) clearly exhibit the S shape and a point of inflection with an adverse gradient. But in the turbulent profiles (Fig. 7.9*b*) the points of inflection are typically buried deep within the thin viscous sublayer, which can hardly be seen on the scale of the figure.

There are scores of turbulent theories in the literature, but they are all complicated algebraically and will be omitted here. The reader is referred to advanced texts [1, 2, 9].

For laminar flow, a simple and effective method was developed by Thwaites [11], who found that Eq. (7.51) can be correlated by a single dimensionless momentum-thickness variable λ, defined as

$$\lambda = \frac{\theta^2}{\nu} \frac{dU}{dx} \tag{7.53}$$

Using a straight-line fit to his correlation, Thwaites was able to integrate Eq. (7.51) in closed form, with the result

$$\theta^2 = \theta_0^2 \left(\frac{U_0}{U}\right)^6 + \frac{0.45\nu}{U^6} \int_0^x U^5 \, dx \tag{7.54}$$

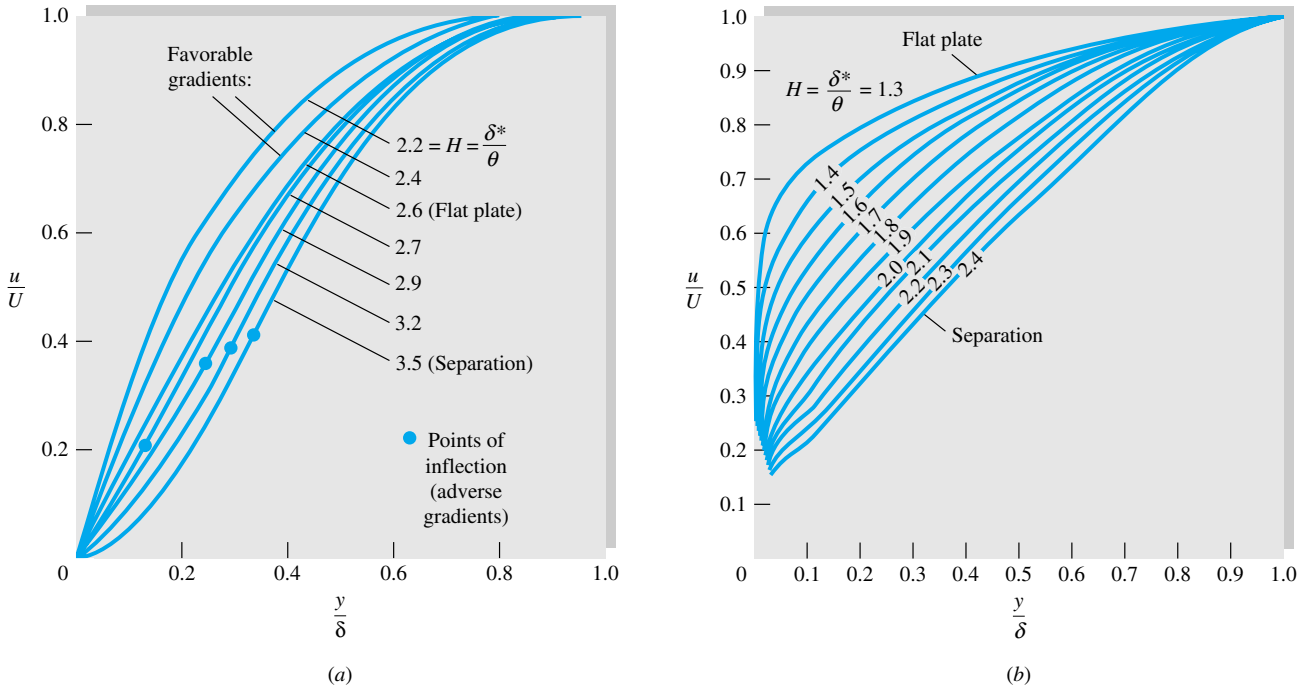

Fig. 7.9 Velocity profiles with pressure gradient: (*a*) laminar flow; (*b*) turbulent flow with adverse gradients.

where θ_0 is the momentum thickness at $x = 0$ (usually taken to be zero). Separation ($c_f = 0$) was found to occur at a particular value of λ

Separation: $$\lambda = -0.09 \tag{7.55}$$

Finally, Thwaites correlated values of the dimensionless shear stress $S = \tau_w\theta/(\mu U)$ with λ, and his graphed result can be curve-fitted as follows:

$$S(\lambda) = \frac{\tau_w \theta}{\mu U} \approx (\lambda + 0.09)^{0.62} \tag{7.56}$$

This parameter is related to the skin friction by the identity

$$S \equiv \tfrac{1}{2} c_f \, \mathrm{Re}_\theta \tag{7.57}$$

Equations (7.54) to (7.56) constitute a complete theory for the laminar boundary layer with variable $U(x)$, with an accuracy of ± 10 percent compared with exact digital-computer solutions of the laminar-boundary-layer equations (7.19). Complete details of Thwaites' and other laminar theories are given in Refs. 2 and 3.

As a demonstration of Thwaites' method, take a flat plate, where U = constant, $\lambda = 0$, and $\theta_0 = 0$. Equation (7.54) integrates to

$$\theta^2 = \frac{0.45\nu x}{U}$$

or
$$\frac{\theta}{x} = \frac{0.671}{\text{Re}_x^{1/2}} \tag{7.58}$$

This is within 1 percent of Blasius' exact solution, Eq. (7.30).

With $\lambda = 0$, Eq. (7.56) predicts the flat-plate shear to be

$$\frac{\tau_w \theta}{\mu U} = (0.09)^{0.62} = 0.225$$

or
$$c_f = \frac{2\tau_w}{\rho U^2} = \frac{0.671}{\text{Re}_x^{1/2}} \tag{7.59}$$

This is also within 1 percent of the Blasius result, Eq. (7.25). However, the general accuracy of this method is poorer than 1 percent because Thwaites actually "tuned" his correlation constants to make them agree with exact flat-plate theory.

We shall not compute any more boundary-layer details here, but as we go along, investigating various immersed-body flows, especially in Chap. 8, we shall use Thwaites' method to make qualitative assessments of the boundary-layer behavior.

EXAMPLE 7.5

In 1938 Howarth proposed a linearly decelerating external-velocity distribution

$$U(x) = U_0\left(1 - \frac{x}{L}\right) \tag{1}$$

as a theoretical model for laminar-boundary-layer study. (*a*) Use Thwaites' method to compute the separation point x_{sep} for $\theta_0 = 0$, and compare with the exact digital-computer solution $x_{\text{sep}}/L = 0.119863$ given by H. Wipperman in 1966. (*b*) Also compute the value of $c_f = 2\tau_w/(\rho U^2)$ at $x/L = 0.1$.

Solution

Part (a) First note that $dU/dx = -U_0/L$ = constant: Velocity decreases, pressure increases, and the pressure gradient is adverse throughout. Now integrate Eq. (7.54)

$$\theta^2 = \frac{0.45\nu}{U_0^6(1 - x/L)^6} \int_0^x U_0^5\left(1 - \frac{x}{L}\right)^5 dx = 0.075\,\frac{\nu L}{U_0}\left[\left(1 - \frac{x}{L}\right)^{-6} - 1\right] \tag{2}$$

Then the dimensionless factor λ is given by

$$\lambda = \frac{\theta^2}{\nu}\frac{dU}{dx} = -\frac{\theta^2 U_0}{\nu L} = -0.075\left[\left(1 - \frac{x}{L}\right)^{-6} - 1\right] \tag{3}$$

From Eq. (7.55) we set this equal to -0.09 for separation

$$\lambda_{\text{sep}} = -0.09 = -0.075\left[\left(1 - \frac{x_{\text{sep}}}{L}\right)^{-6} - 1\right]$$

or
$$\frac{x_{\text{sep}}}{L} = 1 - (2.2)^{-1/6} = 0.123 \qquad \textit{Ans. (a)}$$

This is less than 3 percent higher than Wipperman's exact solution, and the computational effort is very modest.

Part (b) To compute c_f at $x/L = 0.1$ (just before separation), we first compute λ at this point, using Eq. (3)

$$\lambda(x = 0.1L) = -0.075[(1 - 0.1)^{-6} - 1] = -0.0661$$

Then from Eq. (7.56) the shear parameter is

$$S(x = 0.1L) = (-0.0661 + 0.09)^{0.62} = 0.099 = \tfrac{1}{2}c_f \, \mathrm{Re}_\theta \tag{4}$$

We can compute Re_θ in terms of Re_L from Eq. (2) or (3)

$$\frac{\theta^2}{L^2} = \frac{0.0661}{UL/\nu} = \frac{0.0661}{\mathrm{Re}_L}$$

or

$$\mathrm{Re}_\theta = 0.257 \, \mathrm{Re}_L^{1/2} \qquad \text{at } \frac{x}{L} = 0.1$$

Substitute into Eq. (4):

$$0.099 = \tfrac{1}{2}c_f(0.257 \, \mathrm{Re}_L^{1/2})$$

or

$$c_f = \frac{0.77}{\mathrm{Re}_L^{1/2}} \qquad \mathrm{Re}_L = \frac{UL}{\nu} \qquad \textit{Ans. (b)}$$

We cannot actually compute c_f without the value of, say, U_0L/ν.

7.6 Experimental External Flows

Boundary-layer theory is very interesting and illuminating and gives us a great qualitative grasp of viscous-flow behavior, but, because of flow separation, the theory does not generally allow a quantitative computation of the complete flow field. In particular, there is at present no satisfactory theory for the forces on an arbitrary body immersed in a stream flowing at an arbitrary Reynolds number. Therefore experimentation is the key to treating external flows.

Literally thousands of papers in the literature report experimental data on specific external viscous flows. This section gives a brief description of the following external-flow problems:

1. Drag of two-and three-dimensional bodies
   - *a*. Blunt bodies
   - *b*. Streamlined shapes
2. Performance of lifting bodies
   - *a*. Airfoils and aircraft
   - *b*. Projectiles and finned bodies
   - *c*. Birds and insects

For further reading see the goldmine of data compiled in Hoerner [12]. In later chapters we shall study data on supersonic airfoils (Chap. 9), open-channel friction (Chap. 10), and turbomachinery performance (Chap. 11).

Drag of Immersed Bodies

Any body of any shape when immersed in a fluid stream will experience forces and moments from the flow. If the body has arbitrary shape and orientation, the flow will exert forces and moments about all three coordinate axes, as shown in Fig. 7.10. It is customary to choose one axis parallel to the free stream and positive downstream. The force on the body along this axis is called *drag,* and the moment about that axis the *rolling moment*. The drag is essentially a flow loss and must be overcome if the body is to move against the stream.

A second and very important force is perpendicular to the drag and usually performs a useful job, such as bearing the weight of the body. It is called the *lift*. The moment about the lift axis is called *yaw*.

The third component, neither a loss nor a gain, is the *side force,* and about this axis is the *pitching moment*. To deal with this three-dimensional force-moment situation is more properly the role of a textbook on aerodynamics [for example, 13]. We shall limit the discussion here to lift and drag.

When the body has symmetry about the lift-drag axis, e.g., airplanes, ships, and cars moving directly into a stream, the side force, yaw, and roll vanish, and the problem reduces to a two-dimensional case: two forces, lift and drag, and one moment, pitch.

A final simplification often occurs when the body has two planes of symmetry, as in Fig. 7.11. A wide variety of shapes such as cylinders, wings, and all bodies of revolution satisfy this requirement. If the free stream is parallel to the intersection of these two planes, called the *principal chord line of the body,* the body experiences drag only, with no lift, side force, or moments.[4] This type of degenerate one-force drag data is what is most commonly reported in the literature, but if the free stream is not parallel to the chord line, the body will have an unsymmetric orientation and all three forces and three moments can arise in principle.

In low-speed flow past geometrically similar bodies with identical orientation and relative roughness, the drag coefficient should be a function of the body Reynolds number

$$C_D = f(\text{Re}) \tag{7.60}$$

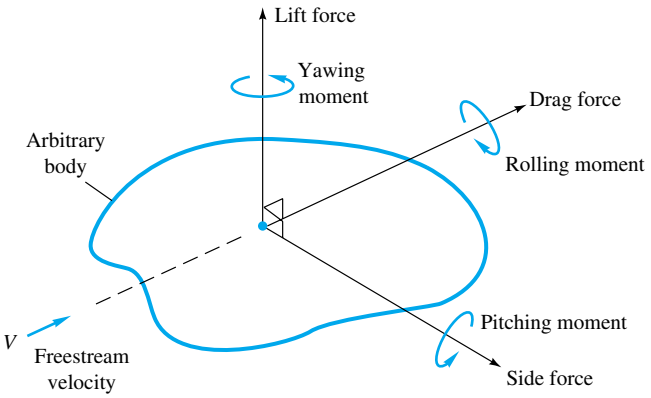

Fig. 7.10 Definition of forces and moments on a body immersed in a uniform flow.

[4]In bodies with shed vortices, such as the cylinder in Fig. 5.2, there may be *oscillating* lift, side force, and moments, but their mean value is zero.

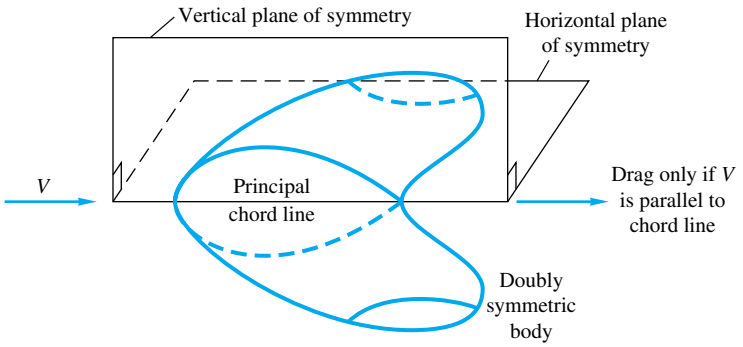

Fig. 7.11 Only the drag force occurs if the flow is parallel to both planes of symmetry.

The Reynolds number is based upon the free-stream velocity V and a characteristic length L of the body, usually the chord or body length parallel to the stream

$$\text{Re} = \frac{VL}{\nu} \tag{7.61}$$

For cylinders, spheres, and disks, the characteristic length is the diameter D.

Characteristic Area

Drag coefficients are defined by using a characteristic area A which may differ depending upon the body shape:

$$C_D = \frac{\text{drag}}{\frac{1}{2}\rho V^2 A} \tag{7.62}$$

The factor $\frac{1}{2}$ is our traditional tribute to Euler and Bernoulli. The area A is usually one of three types:

1. *Frontal area,* the body as seen from the stream; suitable for thick, stubby bodies, such as spheres, cylinders, cars, missiles, projectiles, and torpedoes.
2. *Planform area,* the body area as seen from above; suitable for wide, flat bodies such as wings and hydrofoils.
3. *Wetted area,* customary for surface ships and barges.

In using drag or other fluid-force data, it is important to note what length and area are being used to scale the measured coefficients.

Friction Drag and Pressure Drag

As we have mentioned, the theory of drag is weak and inadequate, except for the flat plate. This is because of flow separation. Boundary-layer theory can predict the separation point but cannot accurately estimate the (usually low) pressure distribution in the separated region. The difference between the high pressure in the front stagnation region and the low pressure in the rear separated region causes a large drag contribution called *pressure drag*. This is added to the integrated shear stress or *friction drag* of the body, which it often exceeds:

$$C_D = C_{D,\text{press}} + C_{D,\text{fric}} \tag{7.63}$$

The relative contribution of friction and pressure drag depends upon the body's shape, especially its thickness. Figure 7.12 shows drag data for a streamlined cylinder of very large depth into the paper. At zero thickness the body is a flat plate and exhibits 100 percent friction drag. At thickness equal to the chord length, simulating a circular cylinder, the friction drag is only about 3 percent. Friction and pressure drag are about equal at thickness $t/c = 0.25$. Note that C_D in Fig. 7.12*b* looks quite different when based upon frontal area instead of planform area, planform being the usual choice for this body shape. The two curves in Fig. 7.12*b* represent exactly the same drag data.

Figure 7.13 illustrates the dramatic effect of separated flow and the subsequent failure of boundary-layer theory. The theoretical inviscid pressure distribution on a circular cylinder (Chap. 8) is shown as the dashed line in Fig. 7.13*c*:

$$C_p = \frac{p - p_\infty}{\frac{1}{2}\rho V^2} = 1 - 4\sin^2\theta \tag{7.64}$$

where p_∞ and V are the pressure and velocity, respectively, in the free stream. The actual laminar and turbulent boundary-layer pressure distributions in Fig. 7.13*c* are startlingly different from those predicted by theory. Laminar flow is very vulnerable to the adverse gradient on the rear of the cylinder, and separation occurs at $\theta = 82°$, which

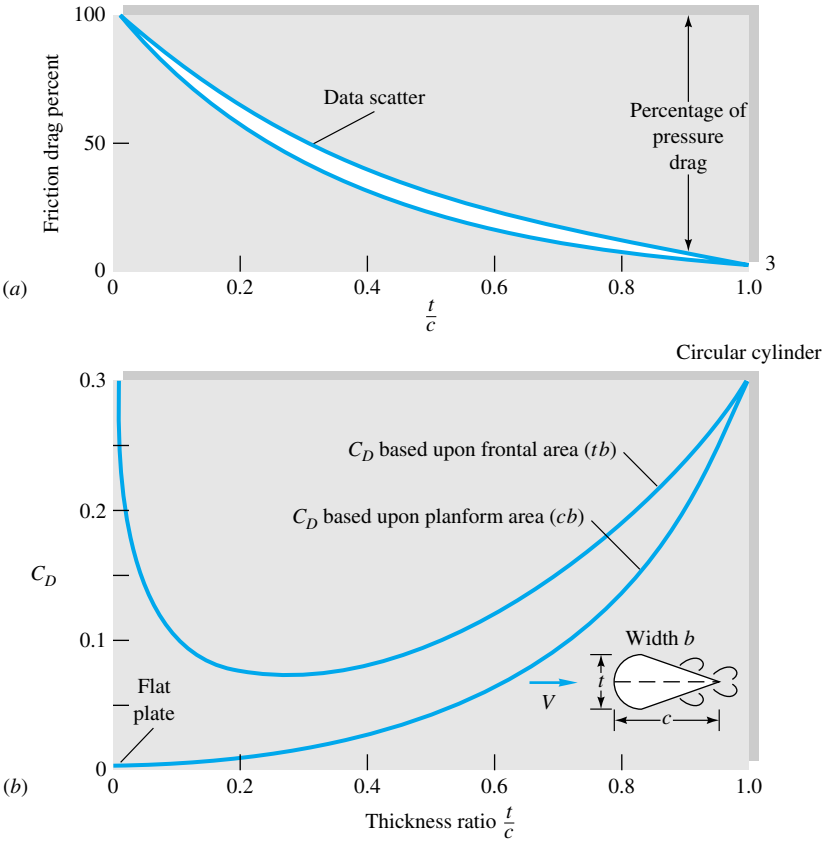

Fig. 7.12 Drag of a streamlined two-dimensional cylinder at $\mathrm{Re}_c = 10^6$: (*a*) effect of thickness ratio on percentage of friction drag; (*b*) total drag versus thickness when based upon two different areas.

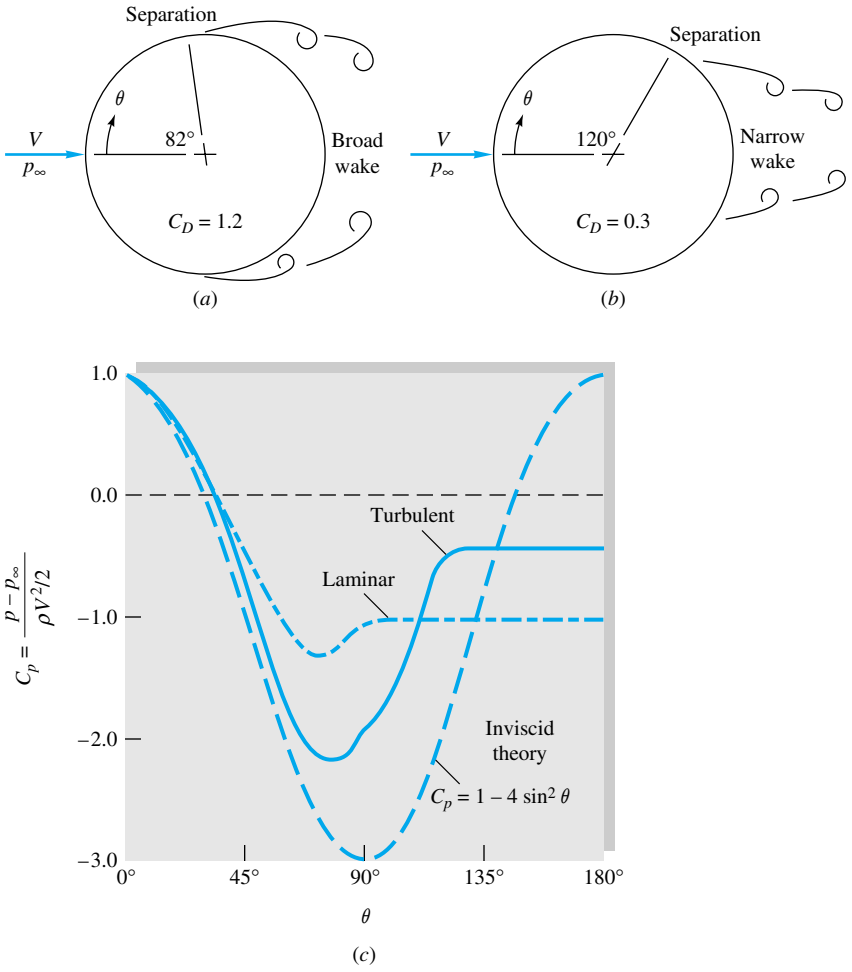

Fig. 7.13 Flow past a circular cylinder: (*a*) laminar separation; (*b*) turbulent separation; (*c*) theoretical and actual surface-pressure distributions.

certainly could not have been predicted from inviscid theory. The broad wake and very low pressure in the separated laminar region cause the large drag $C_D = 1.2$.

The turbulent boundary layer in Fig. 7.13*b* is more resistant, and separation is delayed until $\theta = 120°$, with a resulting smaller wake, higher pressure on the rear, and 75 percent less drag, $C_D = 0.3$. This explains the sharp drop in drag at transition in Fig. 5.3.

The same sharp difference between vulnerable laminar separation and resistant turbulent separation can be seen for a sphere in Fig. 7.14. The laminar flow (Fig. 7.14*a*) separates at about 80°, $C_D = 0.5$, while the turbulent flow (Fig. 7.14*b*) separates at 120°, $C_D = 0.2$. Here the Reynolds numbers are exactly the same, and the turbulent boundary layer is induced by a patch of sand roughness at the nose of the ball. Golf balls fly in this range of Reynolds numbers, which is why they are deliberately dimpled − to induce a turbulent boundary layer and lower drag. Again we would find the actual pressure distribution on the sphere to be quite different from that predicted by inviscid theory.

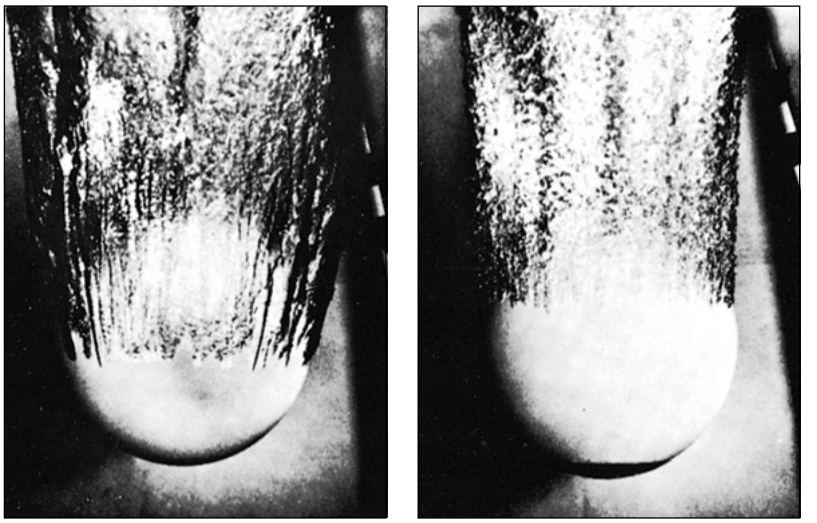

(*a*) (*b*)

Fig. 7.14 Strong differences in laminar and turbulent separation on an 8.5-in bowling ball entering water at 25 ft/s: (*a*) smooth ball, laminar boundary layer; (*b*) same entry, turbulent flow induced by patch of nose-sand roughness. (*U.S. Navy photograph, Ordnance Test Station, Pasadena Annex.*)

In general, we cannot overstress the importance of body streamlining to reduce drag at Reynolds numbers above about 100. This is illustrated in Fig. 7.15. The rectangular cylinder (Fig. 7.15*a*) has rampant separation at all sharp corners and very high drag. Rounding its nose (Fig. 7.15*b*) reduces drag by about 45 percent, but C_D is still high. Streamlining its rear to a sharp trailing edge (Fig. 7.15*c*) reduces its drag another 85 percent to a practical minimum for the given thickness. As a dramatic contrast, the circular cylinder (Fig. 7.15*d*) has one-eighth the thickness and one-three-hundredth the cross section (*c*) (Fig. 7.15*c*), yet it has the same drag. For high-performance vehicles and other moving bodies, the name of the game is drag reduction, for which intense research continues for both aerodynamic and hydrodynamic applications [20, 39].

The drag of some representative wide-span (nearly two-dimensional) bodies is shown versus the Reynolds number in Fig. 7.16*a*. All bodies have high C_D at very low (*creeping flow*) Re $\leq$ 1.0, while they spread apart at high Reynolds numbers according to

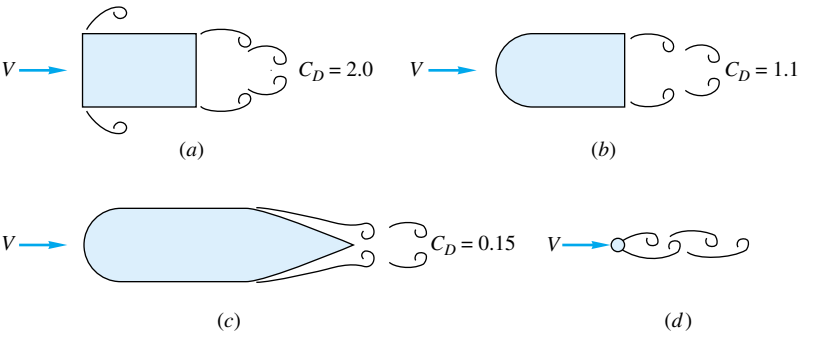

Fig. 7.15 The importance of streamlining in reducing drag of a body (C_D based on frontal area): (*a*) rectangular cylinder; (*b*) rounded nose; (*c*) rounded nose and streamlined sharp trailing edge; (*d*) circular cylinder with the same drag as case (*c*).

their degree of streamlining. All values of C_D are based on the planform area except the plate normal to the flow. The birds and the sailplane are, of course, not very two-dimensional, having only modest span length. Note that birds are not nearly as efficient as modern sailplanes or airfoils [14, 15].

Table 7.2 gives a few data on drag, based on frontal area, of two-dimensional bodies of various cross section, at Re $\geq 10^4$. The sharp-edged bodies, which tend to cause flow separation regardless of the character of the boundary layer, are insensitive to the Reynolds number. The elliptic cylinders, being smoothly rounded, have the laminar-to-turbulent transition effect of Figs. 7.13 and 7.14 and are therefore quite sensitive to whether the boundary layer is laminar or turbulent.

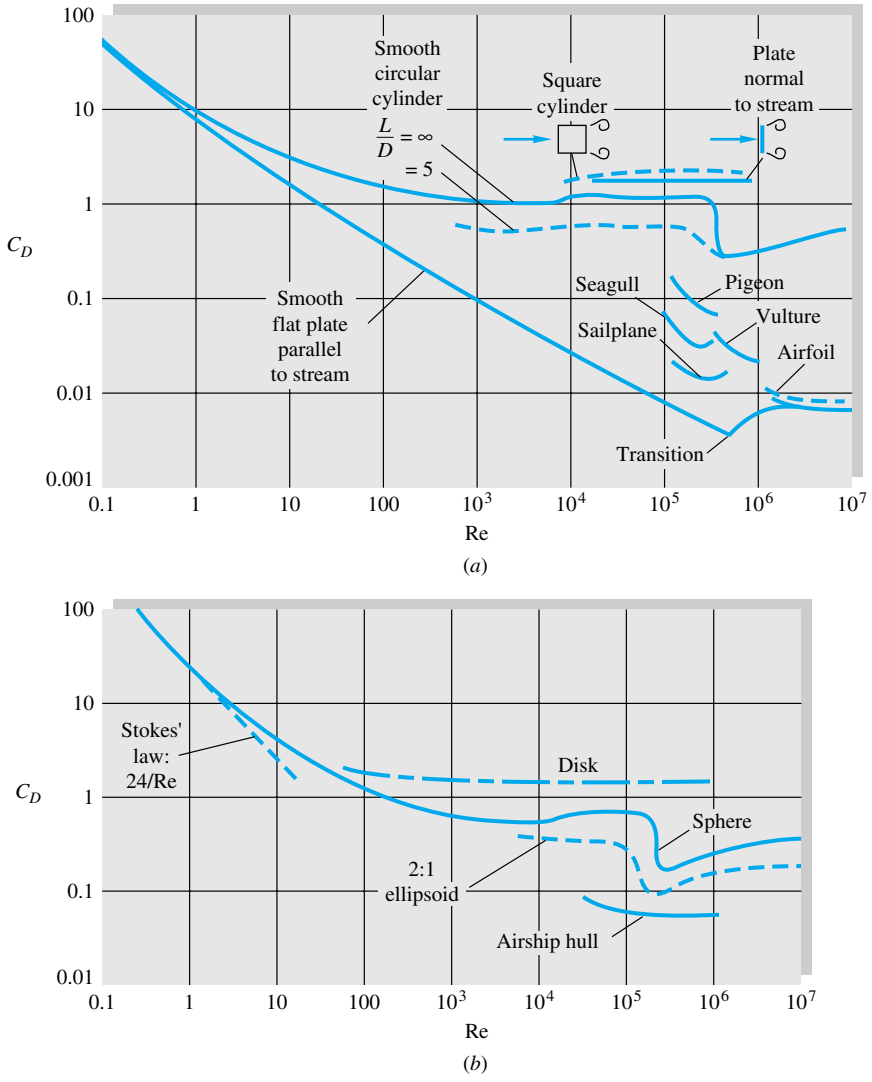

Fig. 7.16 Drag coefficients of smooth bodies at low Mach numbers: (*a*) two-dimensional bodies; (*b*) three-dimensional bodies. Note the Reynolds-number independence of blunt bodies at high Re.

Table 7.2 Drag of Two-Dimensional Bodies at Re $\geq 10^4$

Shape	C_D based on frontal area
Square cylinder: 	2.1
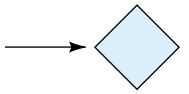	1.6
Half tube: 	1.2
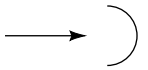	2.3
Half-cylinder: 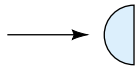	1.2
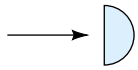	1.7
Equilateral triangle: 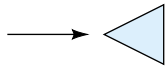	1.6
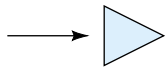	2.0
Plate: 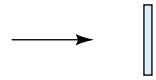	2.0
Thin plate normal to a wall: 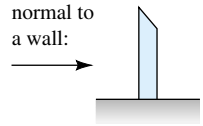	1.4
Hexagon: 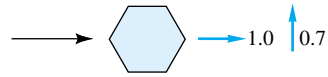	1.0 / 0.7

Shape	C_D based on frontal area
Rounded nose section: 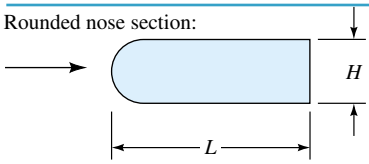	L/H: 0.5 / 1.0 / 2.0 / 4.0 / 6.0 C_D: 1.16 / 0.90 / 0.70 / 0.68 / 0.64
Flat nose section 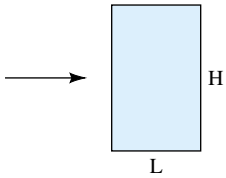	L/H: 0.1 / 0.4 / 0.7 / 1.2 / 2.0 / 2.5 / 3.0 / 6.0 C_D: 1.9 / 2.3 / 2.7 / 2.1 / 1.8 / 1.4 / 1.3 / 0.9

Elliptical cylinder:	Laminar	Turbulent
1:1 	1.2	0.3
2:1 	0.6	0.2
4:1 	0.35	0.15
8:1 	0.25	0.1

EXAMPLE 7.6

A square 6-in piling is acted on by a water flow of 5 ft/s that is 20 ft deep, as shown in Fig. E7.6. Estimate the maximum bending exerted by the flow on the bottom of the piling.

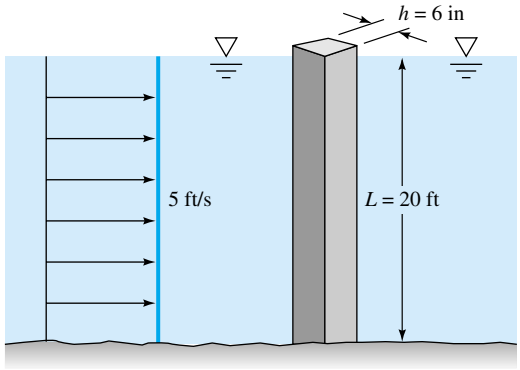

E7.6

Solution

Assume seawater with $\rho = 1.99$ slugs/ft^3 and kinematic viscosity $\nu = 0.000011$ ft^2/s. With a piling width of 0.5 ft, we have

$$\text{Re}_h = \frac{(5 \text{ ft/s})(0.5 \text{ ft})}{0.000011 \text{ ft}^2/\text{s}} = 2.3 \times 10^5$$

This is the range where Table 7.2 applies. The worst case occurs when the flow strikes the flat side of the piling, $C_D \approx 2.1$. The frontal area is $A = Lh = (20 \text{ ft})(0.5 \text{ ft}) = 10 \text{ ft}^2$. The drag is estimated by

$$F = C_D(\tfrac{1}{2}\rho V^2 A) \approx 2.1(\tfrac{1}{2})(1.99 \text{ slugs/ft}^3)(5 \text{ ft/s})^2(10 \text{ ft}^2) = 522 \text{ lbf}$$

If the flow is uniform, the center of this force should be at approximately middepth. Therefore the bottom bending moment is

$$M_0 \approx \frac{FL}{2} = 522(10) = 5220 \text{ ft} \cdot \text{lbf} \qquad \textit{Ans.}$$

According to the flexure formula from strength of materials, the bending stress at the bottom would be

$$S = \frac{M_0 y}{I} = \frac{(5220 \text{ ft} \cdot \text{lb})(0.25 \text{ ft})}{\frac{1}{12}(0.5 \text{ ft})^4} = 251{,}000 \text{ lbf/ft}^2 = 1740 \text{ lbf/in}^2$$

to be multiplied, of course, by the stress-concentration factor due to the built-in end conditions.

Some drag coefficients of three-dimensional bodies are listed in Table 7.3 and Fig. 7.16*b*. Again we can conclude that sharp edges always cause flow separation and high drag which is insensitive to the Reynolds number. Rounded bodies like the ellipsoid have drag which depends upon the point of separation, so that both the Reynolds num-

Table 7.3 Drag of Three-Dimensional Bodies at Re $\geq 10^4$

Body	C_D based on frontal area
Cube:	
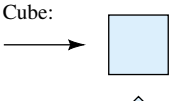	1.07
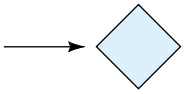	0.81
Cup:	
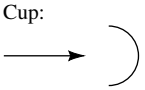	1.4
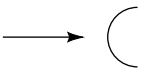	0.4
Disk:	
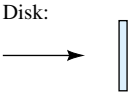	1.17
Parachute (Low porosity):	
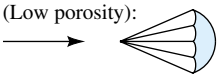	1.2

Body	C_D based on frontal area
Cone:	
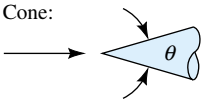	θ: 10° 20° 30° 40° 60° 75° 90° C_D: 0.30 0.40 0.55 0.65 0.80 1.05 1.15
Short cylinder, laminar flow:	
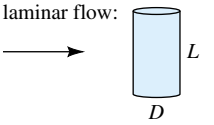	L/D: 1 2 3 5 10 20 40 ∞ C_D: 0.64 0.68 0.72 0.74 0.82 0.91 0.98 1.20
Porous parabolic dish [23]:	
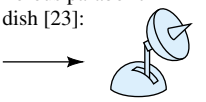	Porosity: 0 0.1 0.2 0.3 0.4 0.5 ← C_D: 1.42 1.33 1.20 1.05 0.95 0.82 → C_D: 0.95 0.92 0.90 0.86 0.83 0.80
Average person:	
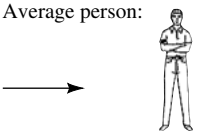	→ $C_DA \approx 9$ ft^2 ↑ $C_DA \approx 1.2$ ft^2
Pine and spruce trees [24]:	
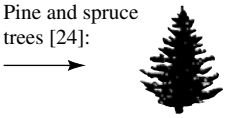	U, m/s: 10 20 30 40 C_D: 1.2 ± 0.2 1.0 ± 0.2 0.7 ± 0.2 0.5 ± 0.2

Body	Ratio	C_D based on frontal area
Rectangular plate:		
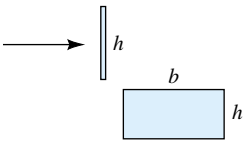	b/h 1	1.18
	5	1.2
	10	1.3
	20	1.5
	∞	2.0

Body	Ratio	C_D based on frontal area
Flat-faced cylinder:		
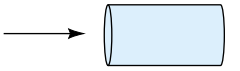	L/d 0.5	1.15
	1	0.90
	2	0.85
	4	0.87
	8	0.99

Body	Ratio	C_D based on frontal area	
		Laminar	Turbulent
Ellipsoid:			
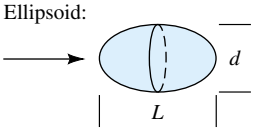	L/d 0.75	0.5	0.2
	1	0.47	0.2
	2	0.27	0.13
	4	0.25	0.1
	8	0.2	0.08

ber and the character of the boundary layer are important. Body length will generally decrease pressure drag by making the body relatively more slender, but sooner or later the friction drag will catch up. For the flat-faced cylinder in Table 7.3, pressure drag decreases with L/d but friction increases, so that minimum drag occurs at about $L/d = 2$.

Aerodynamic Forces on Road Vehicles

Automobiles and trucks are now the subject of much research on aerodynamic forces, both lift and drag [21]. At least one textbook is devoted to the subject [22]. Consumer, manufacturer, and government interest has cycled between high speed/high horsepower and lower speed/lower drag. Better streamlining of car shapes has resulted over the years in a large decrease in the automobile drag coefficient, as shown in Fig. 7.17*a*. Modern cars have an average drag coefficient of about 0.35, based upon the frontal

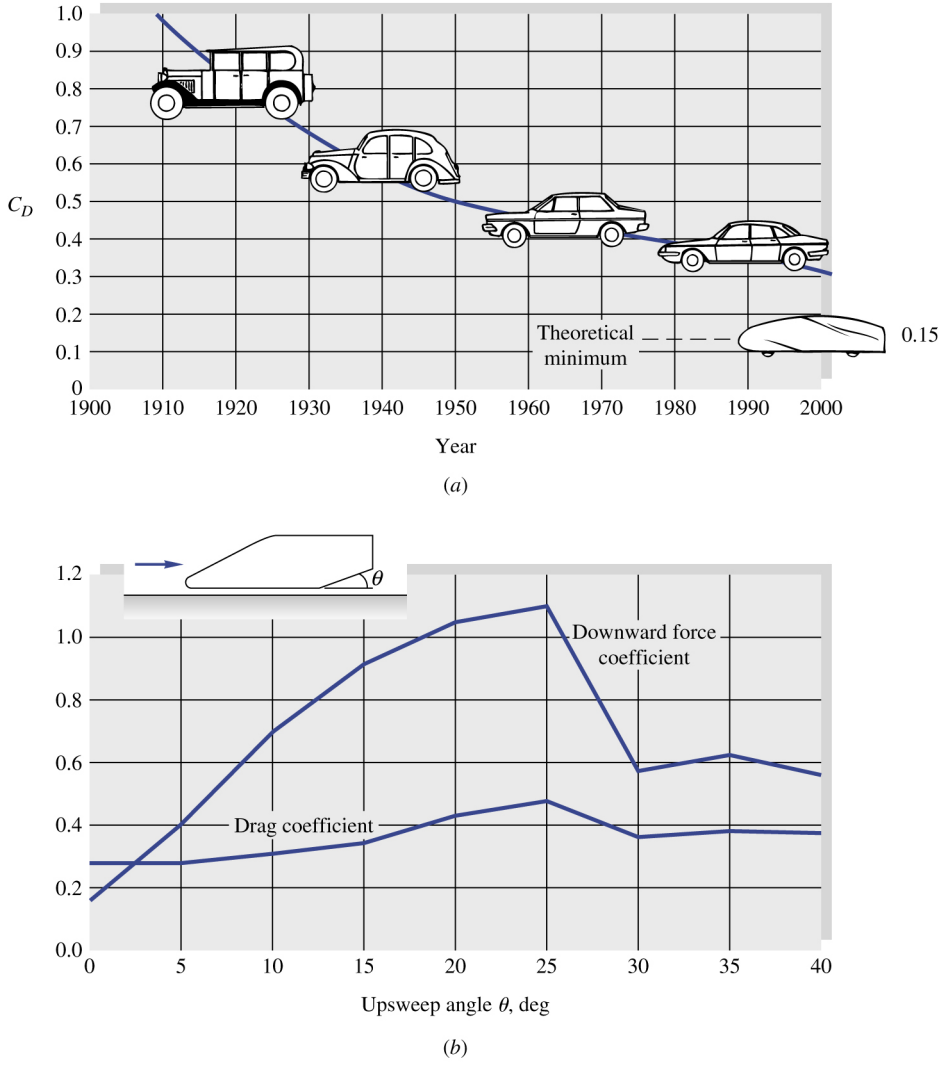

Fig. 7.17 Aerodynamics of automobiles: (*a*) the historical trend for drag coefficients [From Ref. 21]; (*b*) effect of bottom rear upsweep angle on drag and downward lift force [From Ref. 25].

area. Since the frontal area has also decreased sharply, the actual raw drag *force* on cars has dropped even more than indicated in Fig. 7.17*a*. The practical minimum, shown tentatively for the year 2000, is $C_D \approx 0.15$ for a tear-shaped vehicle, which can be achieved any time the public is willing to purchase such a shape. Note that basing C_D on the frontal area is awkward, since one would need an accurate drawing of the automobile to estimate its frontal area. For this reason, some technical articles simply report the raw drag in newtons or pound-force, or the product $C_D A$.

Many companies and laboratories have automotive wind tunnels, some full-scale and/or with moving floors to approximate actual kinematic similarity. The blunt shapes of most automobiles, together with their proximity to the ground, cause a wide variety of flow and geometric effects. Simple changes in part of the shape can have a large influence on aerodynamic forces. Figure 7.17*b* shows force data by Bearman et al. [25] for an idealized smooth automobile shape with upsweep in the rear of the bottom section. We see that by simply adding an upsweep angle of 25°, we can quadruple the downward force, gaining tire traction at the expense of doubling the drag. For this study, the effect of a moving floor was small—about a 10 percent increase in both drag and lift compared to a fixed floor.

It is difficult to quantify the exact effect of geometric changes on automotive forces, since, e.g., changes in a windshield shape might interact with downstream flow over the roof and trunk. Nevertheless, based on correlation of many model and full-scale tests, Ref. 26 proposes a formula for automobile drag which adds separate effects such as front ends, cowls, fenders, windshield, roofs, and rear ends.

Figure 7.18 shows the horsepower required to drive a typical tractor-trailer truck at speeds up to 80 mi/h (117 ft/s or 36 m/s). The rolling resistance increases linearly and the air drag quadratically with speed ($C_D \approx 1.0$). The two are about equally important at 55 mi/h, which is the nominal speed limit in the United States. As shown in Fig. 7.18*b*, air drag can be reduced by attaching a deflector to the top of the tractor. If the angle of the deflector is adjusted to carry the flow smoothly over the top and around the sides of the trailer, the reduction in C_D is about 20 percent. Thus, at 55 mi/h the total resistance is reduced 10 percent, with a corresponding reduction in

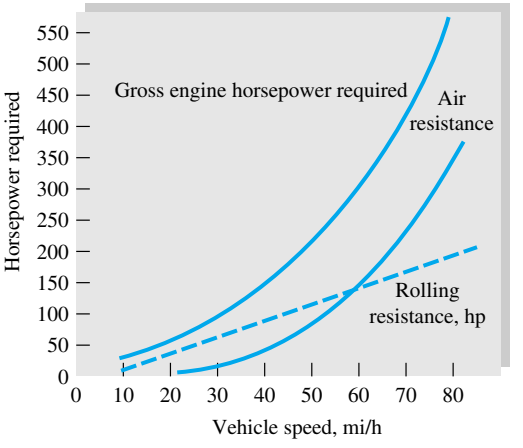

(*a*)

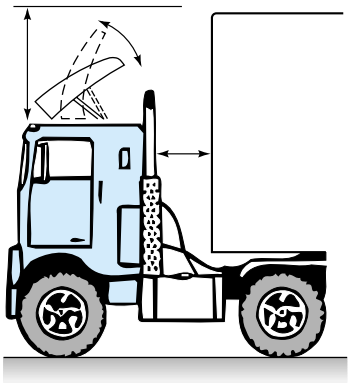

(*b*)

Fig. 7.18 Drag reduction of a tractor-trailer truck: (*a*) horsepower required to overcome resistance; (*b*) deflector added to cab reduces air drag by 20 percent. (*Uniroyal Inc.*)

fuel costs and/or trip time for the trucker. This type of applied fluids engineering can be a large factor in many of the conservation-oriented transportation problems of the future.

EXAMPLE 7.7

A high-speed car with $m = 2000$ kg, $C_D = 0.3$, and $A = 1$ m^2 deploys a 2-m parachute to slow down from an initial velocity of 100 m/s (Fig. E7.7). Assuming constant C_D, brakes free, and no rolling resistance, calculate the distance and velocity of the car after 1, 10, 100, and 1000 s. For air assume $\rho = 1.2$ kg/m^3, and neglect interference between the wake of the car and the parachute.

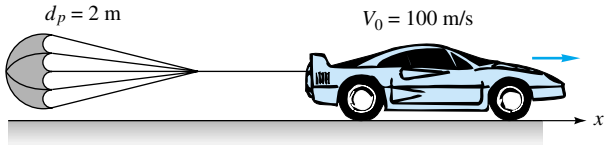

E7.7

Solution

Newton's law applied in the direction of motion gives

$$F_x = m\frac{dV}{dt} = -F_c - F_p = -\frac{1}{2}\rho V^2(C_{Dc}A_c + C_{Dp}A_p)$$

where subscript c denotes the car and subscript p the parachute. This is of the form

$$\frac{dV}{dt} = -\frac{K}{m}V^2 \qquad K = \sum C_D A\frac{\rho}{2}$$

Separate the variables and integrate

$$\int_{V_0}^{V}\frac{dV}{V^2} = -\frac{K}{m}\int_0^t dt$$

or

$$V_0^{-1} - V^{-1} = -\frac{K}{m}t$$

Rearrange and solve for the velocity V:

$$V = \frac{V_0}{1 + (K/m)V_0 t} \qquad K = \frac{(C_{Dc}A_c + C_{Dp}A_p)\rho}{2} \tag{1}$$

We can integrate this to find the distance traveled:

$$S = \frac{V_0}{\alpha}\ln(1 + \alpha t) \qquad \alpha = \frac{K}{m}V_0 \tag{2}$$

Now work out some numbers. From Table 7.3, $C_{Dp} \approx 1.2$; hence

$$C_{Dc}A_c + C_{Dp}A_p = 0.3(1\text{ m}^2) + 1.2\frac{\pi}{4}(2\text{ m})^2 = 4.07\text{ m}^2$$

Then $$\frac{K}{m} V_0 = \frac{\frac{1}{2}(4.07\ \text{m}^2)(1.2\ \text{kg/m}^3)(100\ \text{m/s})}{2000\ \text{kg}} = 0.122\ \text{s}^{-1} = \alpha$$

Now make a table of the results for V and S from Eqs. (1) and (2):

t, s	1	10	100	1000
V, m/s	89	45	7.6	0.8
S, m	94	654	2110	3940

Air resistance alone will not stop a body completely. If you don't apply the brakes, you'll be halfway to the Yukon Territory and still going.

Other Methods of Drag Reduction

Sometimes drag is good, for example, when using a parachute. Do not jump out of an airplane holding a flat plate parallel to your motion (see Prob. 7.81). Mostly, though, drag is bad and should be reduced. The classical method of drag reduction is *streamlining* (Figs. 7.15 and 7.18). For example, nose fairings and body panels have produced motorcycles which can travel over 200 mi/h. More recent research has uncovered other methods which hold great promise, especially for turbulent flows.

1. Oil pipelines introduce an *annular core* of water to reduce the pumping power [36]. The low-viscosity water rides the wall and reduces friction up to 60 percent.
2. Turbulent friction in liquid flows is reduced up to 60 percent by dissolving small amounts of a *high-molecular-weight polymer additive* [37]. Without changing pumps, the Trans-Alaska Pipeline System (TAPS) increased oil flow 50 percent by injecting small amounts of polymer dissolved in kerosene.
3. Stream-oriented surface *vee-groove microriblets* reduce turbulent friction up to 8 percent [38]. Riblet heights are of order 1 mm and were used on the Stars and Stripes yacht hull in the Americas Cup races. Riblets are also effective on aircraft skins.
4. Small, near-wall *large-eddy breakup devices* (LEBUs) reduce local turbulent friction up to 10 percent [39]. However, one must add these small structures to the surface.
5. Air *microbubbles* injected at the wall of a water flow create a low-shear bubble blanket [40]. At high void fractions, drag reduction can be 80 percent.
6. Spanwise (transverse) *wall oscillation* may reduce turbulent friction up to 30 percent [41].

Drag reduction is presently an area of intense and fruitful research and applies to many types of airflows and water flows for both vehicles and conduits.

Drag of Surface Ships

The drag data above, such as Tables 7.2 and 7.3, are for bodies "fully immersed" in a free stream, i.e., with no free surface. If, however, the body moves at or near a free liquid surface, *wave-making drag* becomes important and is dependent upon both the Reynolds number and the Froude number. To move through a water surface, a ship

must create waves on both sides. This implies putting energy into the water surface and requires a finite drag force to keep the ship moving, even in a frictionless fluid. The total drag of a ship can then be approximated as the sum of friction drag and wave-making drag:

$$F \approx F_{\text{fric}} + F_{\text{wave}} \qquad \text{or} \qquad C_D \approx C_{D,\text{fric}} + C_{D,\text{wave}}$$

The friction drag can be estimated by the (turbulent) flat-plate formula, Eq. (7.45), based on the below-water or *wetted area* of the ship.

Reference 27 is an interesting review of both theory and experiment for wake-making surface ship drag. Generally speaking, the bow of the ship creates a wave system whose wavelength is related to the ship speed but not necessarily to the ship length. If the stern of the ship is a wave *trough,* the ship is essentially climbing uphill and has high wave drag. If the stern is a wave crest, the ship is nearly level and has lower drag. The criterion for these two conditions results in certain approximate Froude numbers [27]:

$$\text{Fr} = \frac{V}{\sqrt{gL}} \approx \frac{0.53}{\sqrt{N}} \qquad \begin{array}{l}\text{high drag if } N = 1, 3, 5, 7, \ldots; \\ \text{low drag if } N = 2, 4, 6, 8, \ldots\end{array} \tag{7.65}$$

where V is the ship's speed, L is the ship's length along the centerline, and N is the number of half-lengths, from bow to stern, of the drag-making wave system. The wave drag will increase with the Froude number and oscillate between lower drag (Fr $\approx$ 0.38, 0.27, 0.22, . . .) and higher drag (Fr $\approx$ 0.53, 0.31, 0.24, . . .) with negligible variation for Fr < 0.2. Thus it is best to design a ship to cruise at $N = 2, 4, 6, 8$. Shaping the bow and stern can further reduce wave-making drag.

Figure 7.19 shows the data of Inui [27] for a model ship. The main hull, curve A, shows peaks and valleys in wave drag at the appropriate Froude numbers > 0.2. Introduction of a *bulb* protrusion on the bow, curve B, greatly reduces the drag. Adding a second bulb to the stern, curve C, is still better, and Inui recommends that the design speed of this two-bulb ship be at $N = 4$, Fr ≈ 0.27, which is a nearly "waveless" condition. In this figure $C_{D,\text{wave}}$ is defined as $2F_{\text{wave}}/(\rho V^2 L^2)$ instead of using the wetted area.

The solid curves in Fig. 7.19 are based on potential-flow theory for the below-water hull shape. Chapter 8 is an introduction to potential-flow theory. Modern digital computers can be programmed for numerical CFD solutions of potential flow over the hulls of ships, submarines, yachts, and sailboats, including boundary-layer effects driven by the potential flow [28]. Thus theoretical prediction of flow past surface ships is now at a fairly high level. See also Ref. 15.

Body Drag at High Mach Numbers

All the data presented above are for nearly incompressible flows, with Mach numbers assumed less than about 0.5. Beyond this value compressibility can be very important, with $C_D = \text{fcn}(\text{Re}, \text{Ma})$. As the stream Mach number increases, at some subsonic value $M_{\text{crit}} < 1$ which depends upon the body's bluntness and thickness, the local velocity at some point near the body surface will become sonic. If Ma increases beyond Ma_{crit}, shock waves form, intensify, and spread, raising surface pressures near the front of the body and therefore increasing the pressure drag. The effect can be dramatic with C_D

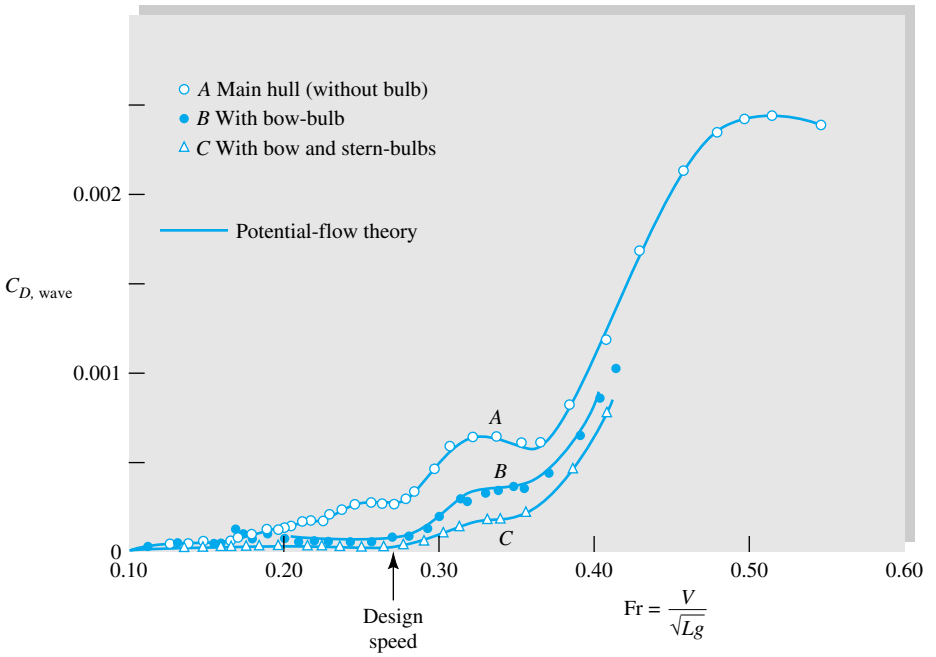

Fig. 7.19 Wave-making drag on a ship model. (*After Inui* [27].) *Note:* The drag coefficient is defined as $C_{DW} = 2F/(\rho V^2 L^2)$.

increasing tenfold, and 70 years ago this sharp increase was called the *sonic barrier,* implying that it could not be surmounted. Of course, it can be—the rise in C_D is finite, as supersonic bullets have proved for centuries.

Figure 7.20 shows the effect of the Mach number on the drag coefficient of various body shapes tested in air.[5] We see that compressibility affects blunt bodies earlier, with Ma_{crit} equal to 0.4 for cylinders, 0.6 for spheres, and 0.7 for airfoils and pointed projectiles. Also the Reynolds number (laminar versus turbulent boundary-layer flow) has a large effect below Ma_{crit} for spheres and cylinders but becomes unimportant above $\text{Ma} \approx 1$. In contrast, the effect of the Reynolds number is small for airfoils and projectiles and is not shown in Fig. 7.20. A general statement might divide Reynolds- and Mach-number effects as follows:

$\text{Ma} \leq 0.4$:	Reynolds number important, Mach number unimportant
$0.4 < \text{Ma} < 1$:	both Reynolds and Mach numbers important
$\text{Ma} > 1.0$:	Reynolds number unimportant, Mach number important

At supersonic speeds, a broad *bow shock wave* forms in front of the body (see Figs. 9.10*b* and 9.19), and the drag is mainly due to high shock-induced pressures on the front. Making the bow a sharp point can sharply reduce the drag (Fig. 9.28) but does not eliminate the bow shock. Chapter 9 gives a brief treatment of compressibility. References 30 and 31 are more advanced textbooks devoted entirely to compressible flow.

[5]There is a slight effect of the specific-heat ratio k which would appear if other gases were tested.

Biological Drag Reduction

A great deal of engineering effort goes into designing immersed bodies to reduce their drag. Most such effort concentrates on rigid-body shapes. A different process occurs in nature, as organisms adapt to survive high winds or currents, as reported in a series of papers by S. Vogel [33, 34]. A good example is a tree, whose flexible structure allows it to reconfigure in high winds and thus reduce drag and damage. Tree root systems have evolved in several ways to resist wind-induced bending moments, and trunk cross sections have become resistant to bending but relatively easy to twist and reconfigure. We saw this in Table 7.3, where tree drag coefficients [24] reduced by 60 percent as wind velocity increased. The shape of the tree changes to offer less resistance.

The individual branches and leaves of a tree also curl and cluster to reduce drag. Figure 7.21 shows the results of wind tunnel experiments by Vogel [33]. A tulip tree leaf, Fig. 7.21(*a*), broad and open in low wind, curls into a conical low-drag shape as wind increases. A compound black walnut leaf group, Fig. 7.21(*b*), clusters into a low-drag shape at high wind speed. Although drag coefficients were reduced up to 50 percent by flexibility, Vogel points out that rigid structures are sometimes just as effective. An interesting recent symposium [35] was devoted entirely to the solid mechanics and fluid mechanics of biological organisms.

Forces on Lifting Bodies

Lifting bodies (airfoils, hydrofoils, or vanes) are intended to provide a large force normal to the free stream and as little drag as possible. Conventional design practice has evolved a shape not unlike a bird's wing, i.e., relatively thin ($t/c \leq 0/18$) with a rounded leading edge and a sharp trailing edge. A typical shape is sketched in Fig. 7.22.

For our purposes we consider the body to be symmetric, as in Fig. 7.11, with the

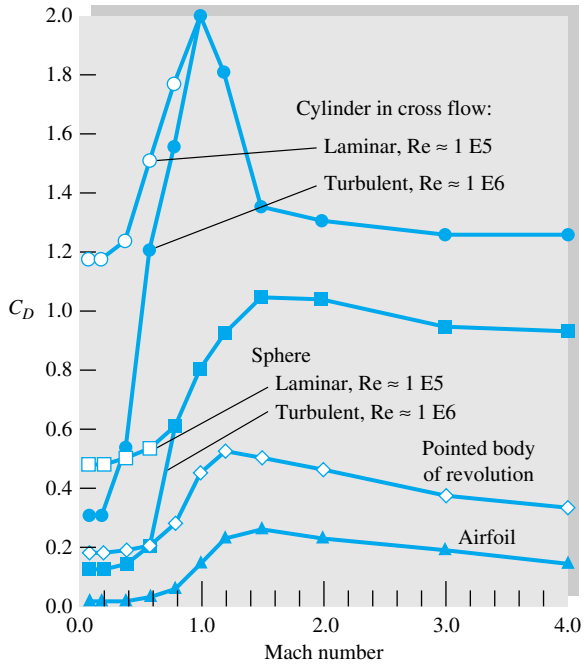

Fig. 7.20 Effect of the Mach number on the drag of various body shapes. (*Data from Refs. 23 and 29.*)

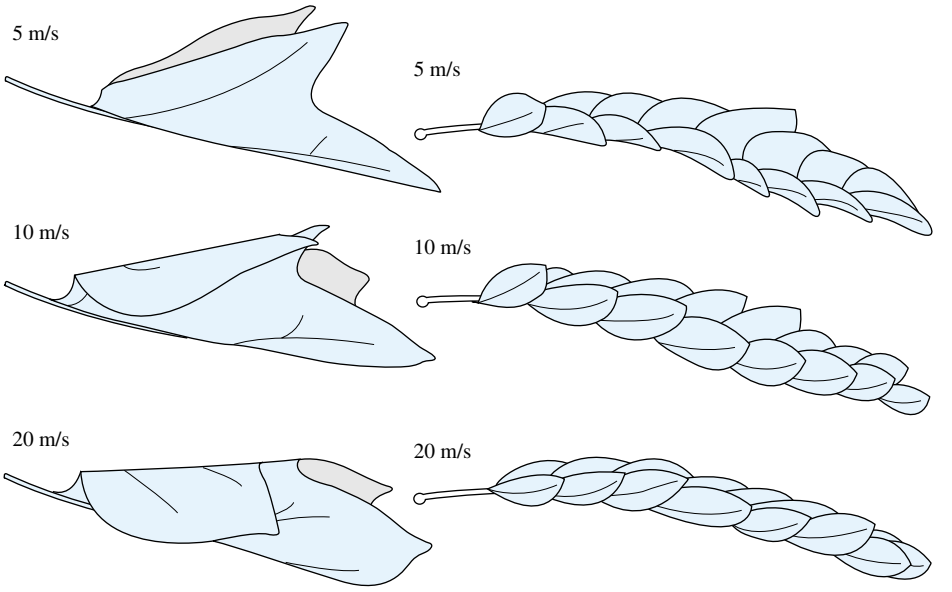

Fig. 7.21 Biological adaptation to wind forces: (*a*) a tulip tree leaf curls into a conical shape at high velocity; (*b*) black walnut leaves cluster into a low-drag shape as wind increases. (*From Vogel, Ref. 33.*)

free-stream velocity in the vertical plane. If the chord line between the leading and trailing edge is not a line of symmetry, the airfoil is said to be *cambered*. The camber line is the line midway between the upper and lower surfaces of the vane.

The angle between the free stream and the chord line is called the *angle of attack* α. The lift L and the drag D vary with this angle. The dimensionless forces are defined with respect to the planform area $A_p = bc$:

Lift coefficient: $$C_L = \frac{L}{\frac{1}{2}\rho V^2 A_p} \tag{7.66a}$$

Drag coefficient: $$C_D = \frac{D}{\frac{1}{2}\rho V^2 A_p} \tag{7.66b}$$

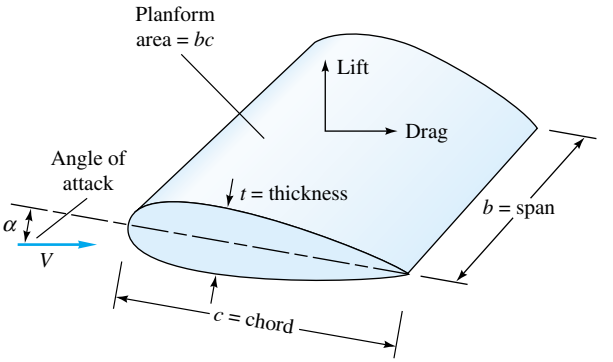

Fig. 7.22 Definition sketch for a lifting vane.

If the chord length is not constant, as in the tapered wings of modern aircraft, $A_p = \int c\, db$.

For low-speed flow with a given roughness ratio, C_L and C_D should vary with α and the chord Reynolds number

$$C_L = f(\alpha, \mathrm{Re}_c) \qquad \text{or} \qquad C_D = f(\alpha, \mathrm{Re}_c)$$

where $\mathrm{Re}_c = Vc/\nu$. The Reynolds numbers are commonly in the turbulent-boundary-layer range and have a modest effect.

The rounded leading edge prevents flow separation there, but the sharp trailing edge causes a separation which generates the lift. Figure 7.23 shows what happens when a flow starts up past a lifting vane or an airfoil.

Just after start-up in Fig. 7.23*a* the streamline motion is irrotational and inviscid. The rear stagnation point, assuming a positive angle of attack, is on the upper surface, and there is no lift; but the flow cannot long negotiate the sharp turn at the trailing edge: it separates, and a *starting vortex* forms in Fig. 7.23*b*. This starting vortex is shed downstream in Fig. 7.23*c* and *d*, and a smooth streamline flow develops over the wing, leaving the foil in a direction approximately parallel to the chord line. Lift at this time is fully developed, and the starting vortex is gone. Should the flow now cease, a *stopping vortex* of opposite (clockwise) sense will form and be shed. During flight, increases or decreases in lift will cause incremental starting or stopping vortices, always with the effect of maintaining a smooth parallel flow at the trailing edge. We pursue this idea mathematically in Chap. 8.

At a low angle of attack, the rear surfaces have an adverse pressure gradient but not enough to cause significant boundary-layer separation. The flow pattern is smooth, as in Fig. 7.23*d*, and drag is small and lift excellent. As the angle of attack is increased, the upper-surface adverse gradient becomes stronger, and generally a *separation bub-*

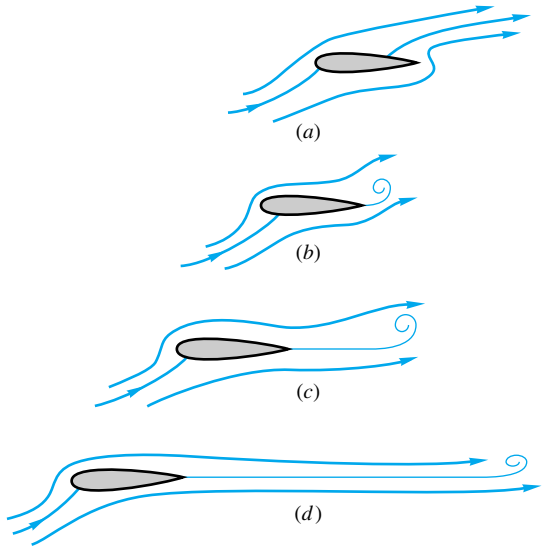

Fig. 7.23 Transient stages in the development of lift: (*a*) start-up: rear stagnation point on the upper surface: no lift; (*b*) sharp trailing edge induces separation, and a starting vortex forms: slight lift; (*c*) starting vortex is shed, and streamlines flow smoothly from trailing edge: lift is now 80 percent developed; (*d*) starting vortex now shed far behind, trailing edge now very smooth: lift fully developed.

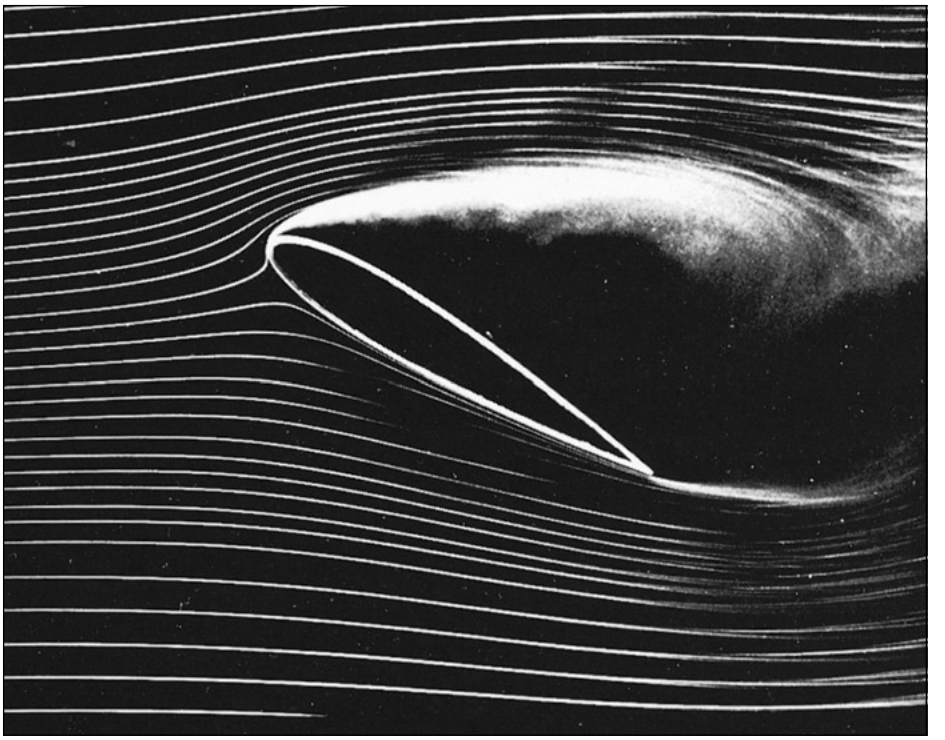

Fig. 7.24 At high angle of attack, smoke-flow visualization shows stalled flow on the upper surface of a lifting vane. *[From Ref. 19,* Illustrated Experiments in Fluid Mechanics (*The NCFMF Book of Film Notes*), *National Committee for Fluid Mechanics Films, Education Development Center, Inc., copyright 1972.]*

ble begins to creep forward on the upper surface.[6] At a certain angle $\alpha = 15$ to 20°, the flow is separated completely from the upper surface, as in Fig. 7.24. The airfoil is said to be *stalled*: Lift drops off markedly, drag increases markedly, and the foil is no longer flyable.

Early airfoils were thin, modeled after birds' wings. The German engineer Otto Lilienthal (1848–1896) experimented with flat and cambered plates on a rotating arm. He and his brother Gustav flew the world's first glider in 1891. Horatio Frederick Phillips (1845–1912) built the first wind tunnel in 1884 and measured the lift and drag of cambered vanes. The first theory of lift was proposed by Frederick W. Lanchester shortly afterward. Modern airfoil theory dates from 1905, when the Russian hydrodynamicist N. E. Joukowsky (1847–1921) developed a circulation theorem (Chap. 8) for computing airfoil lift for arbitrary camber and thickness. With this basic theory, as extended and developed by Prandtl and Kármán and their students, it is now possible to design a low-speed airfoil to satisfy particular surface-pressure distributions and boundary-layer characteristics. There are whole families of airfoil designs, notably those developed in the United States under the sponsorship of the NACA (now NASA). Extensive theory and data on these airfoils are contained in Ref. 16. We shall discuss this further in Chap. 8.

Figure 7.25 shows the lift and drag on a symmetric airfoil denoted as the NACA 0009 foil, the last digit indicating the thickness of 9 percent. With no flap extended,

[6]For some airfoils the bubble leaps, not creeps, forward, and stall occurs rapidly and dangerously.

this airfoil, as expected, has zero lift at zero angle of attack. Up to about 12° the lift coefficient increases linearly with a slope of 0.1 per degree, or 6.0 per radian. This is in agreement with the theory outlined in Chap. 8:

$$C_{L,\text{theory}} \approx 2\pi \sin\left(\alpha + \frac{2h}{c}\right) \tag{7.67}$$

where h/c is the maximum camber expressed as a fraction of the chord. The NACA 0009 has zero camber; hence $C_L = 2\pi \sin \alpha \approx 0.11\alpha$, where α is in degrees. This is excellent agreement.

The drag coefficient of the smooth-model airfoils in Fig. 7.25 is as low as 0.005, which is actually lower than both sides of a flat plate in turbulent flow. This is misleading inasmuch as a commercial foil will have roughness effects; e.g., a paint job will double the drag coefficient.

The effect of increasing Reynolds number in Fig. 7.25 is to increase the maximum lift and stall angle (without changing the slope appreciably) and to reduce the drag coefficient. This is a salutary effect, since the prototype will probably be at a higher Reynolds number than the model (10^7 or more).

For takeoff and landing, the lift is greatly increased by deflecting a split flap, as shown in Fig. 7.25. This makes the airfoil unsymmetric (or effectively cambered) and changes the zero-lift point to $\alpha = -12°$. The drag is also greatly increased by the flap, but the reduction in takeoff and landing distance is worth the extra power needed.

A lifting craft cruises at low angle of attack, where the lift is much larger than the drag. Maximum lift-to-drag ratios for the common airfoils lie between 20 and 50.

Some airfoils, such as the NACA 6 series, are shaped to provide favorable gradients over much of the upper surface at low angles. Thus separation is small, and transition to turbulence is delayed; the airfoil retains a good length of laminar flow even

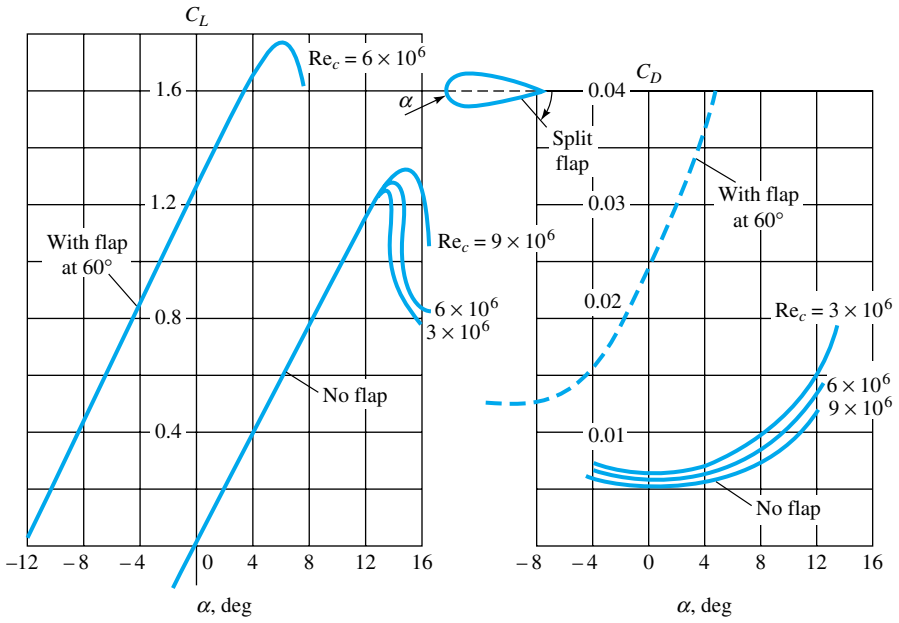

Fig. 7.25 Lift and drag of a symmetric NACA 0009 airfoil of infinite span, including effect of a split-flap deflection. Note that roughness can increase C_D from 100 to 300 percent.

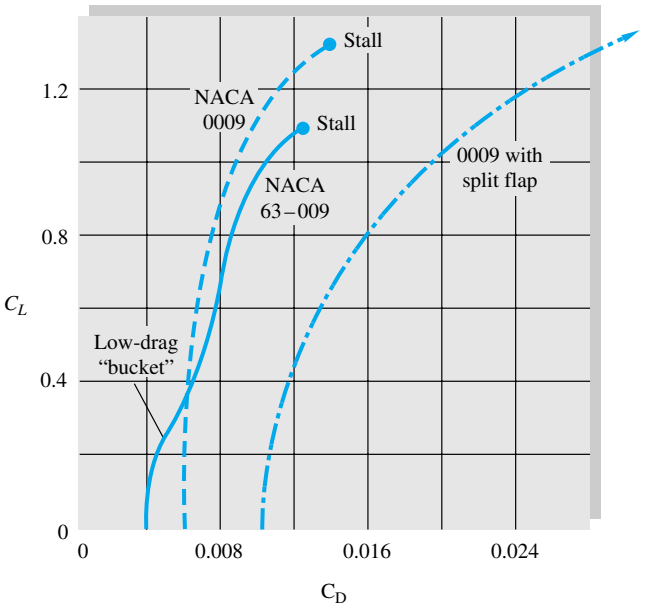

Fig. 7.26 Lift-drag polar plot for standard (0009) and a laminar-flow (63-009) NACA airfoil.

at high Reynolds numbers. The lift-drag polar plot in Fig. 7.26 shows the NACA 0009 data from Fig. 7.25 and a laminar-flow airfoil, NACA 63–009, of the same thickness. The laminar-flow airfoil has a low-drag bucket at small angles but also suffers lower stall angle and lower maximum lift coefficient. The drag is 30 percent less in the bucket, but the bucket disappears if there is significant surface roughness.

All the data in Figs. 7.25 and 7.26 are for infinite span, i.e., a two-dimensional flow pattern about wings without tips. The effect of finite span can be correlated with the dimensionless slenderness, or *aspect ratio,* denoted (AR),

$$\text{AR} = \frac{b^2}{A_p} = \frac{b}{\bar{c}} \tag{7.68}$$

where $\bar{c}$ is the average chord length. Finite-span effects are shown in Fig. 7.27. The lift slope decreases, but the zero-lift angle is the same; and the drag increases, but the zero-lift drag is the same. The theory of finite-span airfoils [16] predicts that the effective angle of attack increases, as in Fig. 7.27, by the amount

$$\Delta\alpha \approx \frac{C_L}{\pi \text{AR}} \tag{7.69}$$

When applied to Eq. (7.67), the finite-span lift becomes

$$C_L \approx \frac{2\pi \sin(\alpha + 2h/c)}{1 + 2/\text{AR}} \tag{7.70}$$

The associated drag increase is $\Delta C_D \approx C_L \sin \Delta\alpha \approx C_L \, \Delta\alpha$, or

$$C_D \approx C_{D\infty} + \frac{C_L^2}{\pi \text{AR}} \tag{7.71}$$

where $C_{D\infty}$ is the drag of the infinite-span airfoil, as sketched in Fig. 7.25. These correlations are in good agreement with experiments on finite-span wings [16].

The existence of a maximum lift coefficient implies the existence of a minimum speed, or *stall speed,* for a craft whose lift supports its weight

$$L = W = C_{L,\max}(\tfrac{1}{2}\rho V_s^2 A_p)$$

or

$$V_s = \left(\frac{2W}{C_{L,\max}\rho A_p}\right)^{1/2} \tag{7.72}$$

The stall speed of typical aircraft varies between 60 and 200 ft/s, depending upon the weight and value of $C_{L,\max}$. The pilot must hold the speed greater than about $1.2V_s$ to avoid the instability associated with complete stall.

The split flap in Fig. 7.25 is only one of many devices used to secure high lift at low speeds. Figure 7.28a shows six such devices whose lift performance is given in 7.28b along with a standard (A) and laminar-flow (B) airfoil. The double-slotted flap achieves $C_{L,\max} \approx 3.4$, and a combination of this plus a leading-edge slat can achieve $C_{L,\max} \approx 4.0$. These are not scientific curiosities; e.g., the Boeing 727 commercial jet aircraft uses a triple-slotted flap plus a leading-edge slat during landing.

Also shown as C in Fig. 7.28b is the Kline-Fogleman airfoil [17], not yet a reality. The designers are amateur model-plane enthusiasts who did not know that conventional aerodynamic wisdom forbids a sharp leading edge and a step cutout from the trailing edge. The Kline-Fogleman airfoil has relatively high drag but shows an amazing continual increase in lift out to $\alpha = 45°$. In fact, we may fairly say that this airfoil does not stall and provides smooth performance over a tremendous range of flight conditions. No explanation for this behavior has yet been published by any aerodynamicist. This airfoil is under study and may or may not have any commercial value.

Another violation of conventional aerodynamic wisdom is that military aircraft are beginning to fly, briefly, *above the stall point.* Fighter pilots are learning to make quick maneuvers in the stalled region as detailed in Ref. 32. Some planes can even *fly continuously* while stalled—the Grumman X-29 experimental aircraft recently set a record by flying at $\alpha = 67°$.

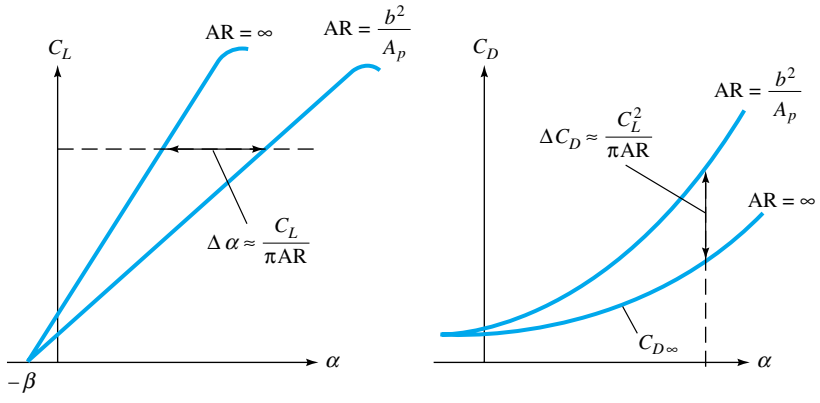

Fig. 7.27 Effect of finite aspect ratio on lift and drag of an airfoil: (*a*) effective angle increase; (*b*) induced drag increase.

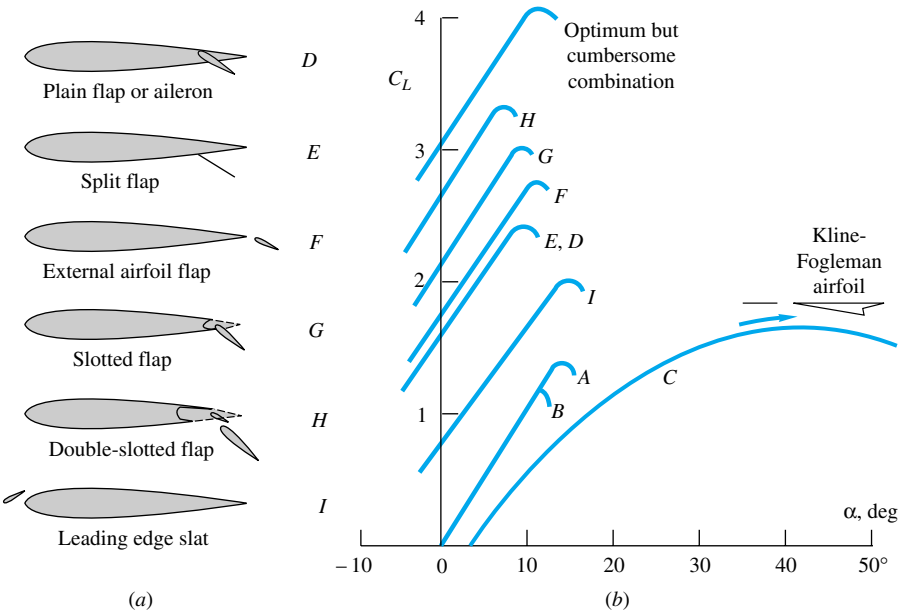

Fig. 7.28 Performance of airfoils with and without high-lift devices: A = NACA 0009; B = NACA 63-009; C = Kline-Fogleman airfoil (*from Ref. 17*); D to I shown in (*a*): (*a*) types of high-lift devices; (*b*) lift coefficients for various devices.

New Aircraft Designs

The Kline-Fogleman airfoil in Fig. 7.28 is a departure from conventional aerodynamics, but there have been other striking departures, as detailed in a recent article [42]. These new aircraft, conceived presently as small models, have a variety of configurations, as shown in Fig. 7.29: ring-wing, cruciform, flying saucer, and flap-wing. A saucer configuration (Fig. 7.29*c*), with a diameter of 40 in, has been successfully flown by radio control, and its inventor, Jack M. Jones, plans for a 20-ft two-passenger version. Another 18-in-span microplane called the Bat (not shown), made by MLB Co., flies for 20 min at 40 mi/h and contains a video camera for surveillance. New engines have been reduced to a 10- by 3-mm size, producing 20 W of power. At the other end of the size spectrum, Boeing and NASA engineers have proposed a jumbo flying-wing jetliner, similar in shape to the stealth bomber, which would carry 800 passengers for a range of 7000 mi.

Further information on the performance of lifting craft can be found in Refs. 12, 13, and 16. We discuss this matter again briefly in Chap. 8.

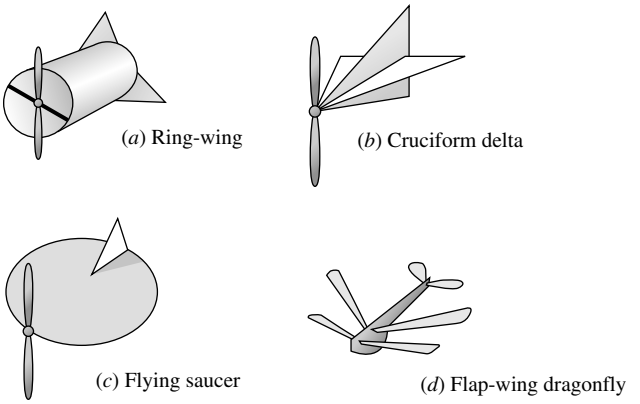

Fig. 7.29 New aircraft designs do not necessarily look like your typical jetliner. *(From Ref. 42.)*

EXAMPLE 7.8

An aircraft weighs 75,000 lb, has a planform area of 2500 ft^2, and can deliver a constant thrust of 12,000 lb. It has an aspect ratio of 7, and $C_{D\infty} \approx 0.02$. Neglecting rolling resistance, estimate the takeoff distance at sea level if takeoff speed equals 1.2 times stall speed. Take $C_{L,\max} = 2.0$.

Solution

The stall speed from Eq. (7.72), with sea-level density $\rho = 0.00237$ slug/ft^3, is

$$V_s = \left(\frac{2W}{C_{L,\max}\rho A_p}\right)^{1/2} = \left[\frac{2(75{,}000)}{2.0(0.00237)(2500)}\right]^{1/2} = 112.5 \text{ ft/s}$$

Hence takeoff speed $V_0 = 1.2V_s = 135$ ft/s. The drag is estimated from Eq. (7.71) for AR = 7 as

$$C_D \approx 0.02 + \frac{C_L^2}{7\pi} = 0.02 + 0.0455C_L^2$$

A force balance in the direction of takeoff gives

$$F_s = m\frac{dV}{dt} = \text{thrust} - \text{drag} = T - kV^2 \qquad k = \tfrac{1}{2}C_D\rho A_p \tag{1}$$

Since we are looking for distance, not time, we introduce $dV/dt = V\,dV/ds$ into Eq. (1), separate variables, and integrate

$$\int_0^{S_0} dS = \frac{m}{2}\int_0^{V_0} \frac{d(V^2)}{T - kV^2} \qquad k \approx \text{const}$$

or

$$S_0 = \frac{m}{2k}\ln\frac{T}{T - kV_0^2} = \frac{m}{2k}\ln\frac{T}{T - D_0} \tag{2}$$

where $D_0 = kV_0^2$ is the takeoff drag. Equation (2) is the desired theoretical relation for takeoff distance. For the particular numerical values, take

$$m = \frac{75{,}000}{32.2} = 2329 \text{ slugs}$$

$$C_{L_0} = \frac{W}{\frac{1}{2}\rho V_0^2 A_p} = \frac{75{,}000}{\frac{1}{2}(0.00237)(135)^2(2500)} = 1.39$$

$$C_{D_0} = 0.02 + 0.0455(C_{L_0})^2 = 0.108$$

$$k \approx \tfrac{1}{2}C_{D_0}\rho A_p = (\tfrac{1}{2})(0.108)(0.00237)(2500) = 0.319 \text{ slug/ft}$$

$$D_0 = kV_0^2 = 5820 \text{ lb}$$

Then Eq. (2) predicts that

$$S_0 = \frac{2329 \text{ slugs}}{2(0.319 \text{ slug/ft})}\ln\frac{12{,}000}{12{,}000 - 5820} = 3650 \ln 1.94 = 2420 \text{ ft} \qquad \textit{Ans.}$$

A more exact analysis accounting for variable k [13] gives the same result to within 1 percent.

Summary

This chapter has dealt with viscous effects in external flow past bodies immersed in a stream. When the Reynolds number is large, viscous forces are confined to a thin boundary layer and wake in the vicinity of the body. Flow outside these "shear layers" is essentially inviscid and can be predicted by potential theory and Bernoulli's equation.

The chapter begins with a discussion of the flat-plate boundary layer and the use of momentum-integral estimates to predict the wall shear, friction drag, and thickness of such layers. These approximations suggest how to eliminate certain small terms in the Navier-Stokes equations, resulting in Prandtl's boundary-layer equations for laminar and turbulent flow. Section 7.4 then solves the boundary-layer equations to give very accurate formulas for flat-plate flow at high Reynolds numbers. Rough-wall effects are included, and Sec. 7.5 gives a brief introduction to pressure-gradient effects. An adverse (decelerating) gradient is seen to cause flow separation, where the boundary layer breaks away from the surface and forms a broad, low-pressure wake.

Boundary-layer theory fails in separated flows, which are commonly studied by experiment. Section 7.6 gives data on drag coefficients of various two- and three-dimensional body shapes. The chapter ends with a brief discussion of lift forces generated by lifting bodies such as airfoils and hydrofoils. Airfoils also suffer flow separation or *stall* at high angles of incidence.

Problems

Most of the problems herein are fairly straightforward. More difficult or open-ended assignments are labeled with an asterisk. Problems labeled with an EES icon will benefit from the use of the Engineering Equation Solver (EES), while problems labeled with a computer disk may require the use of a computer. The standard end-of-chapter problems 7.1 to 7.124 (categorized in the problem list below) are followed by word problems W7.1 to W7.12, fundamentals of engineering exam problems FE7.1 to FE7.10, comprehensive problems C7.1 to C7.4, and design project D7.1.

Problem Distribution

Section	Topic	Problems
7.1	Reynolds-number and geometry	7.1–7.5
7.2	Momentum-integral estimates	7.6–7.12
7.3	The boundary-layer equations	7.13–7.15
7.4	Laminar flat-plate flow	7.16–7.29
7.4	Turbulent flat-plate flow	7.30–7.46
7.5	Boundary layers with pressure gradient	7.47–7.52
7.6	Drag of two-dimensional bodies	7.53–7.63
7.6	Drag of three-dimensional bodies	7.64–7.114
7.6	Lifting bodies—airfoils	7.115–7.124

P7.1 For flow at 20 m/s past a thin flat plate, estimate the distances x from the leading edge at which the boundary-layer thickness will be either 1 mm or 10 cm for (*a*) air and (*b*) water at 20°C and 1 atm.

P7.2 Air, equivalent to that at a standard altitude of 4000 m, flows at 450 mi/h past a wing which has a thickness of 18 cm, a chord length of 1.5 m, and a wingspan of 12 m. What is the appropriate value of the Reynolds number for correlating the lift and drag of this wing? Explain your selection.

P7.3 Equation (7.1*b*) assumes that the boundary layer on the plate is turbulent from the leading edge onward. Devise a scheme for determining the boundary-layer thickness more accurately when the flow is laminar up to a point $\mathrm{Re}_{x,\mathrm{crit}}$ and turbulent thereafter. Apply this scheme to computation of the boundary-layer thickness at $x = 1.5$ m in 40 m/s flow of air at 20°C and 1 atm past a flat plate. Compare your result with Eq. (7.1*b*). Assume $\mathrm{Re}_{x,\mathrm{crit}} \approx 1.2$ E6.

P7.4 Air at 20°C and 1 atm flows at 15 m/s past a flat plate with $\mathrm{Re}_{x,\mathrm{crit}} \approx 1$ E6. At what point x will the boundary-layer thickness be 8 mm? Why do Eqs. (7.1) seem to fail? Make a sketch illustrating the discrepancy; then use the ideas in Prob. 7.3 to complete this problem correctly.

P7.5 SAE 30 oil at 20°C flows at 1.8 ft^3/s from a reservoir into a 6-in-diameter pipe. Use flat-plate theory to estimate the position x where the pipe-wall boundary layers meet in the center. Compare with Eq. (6.5), and give some explanations for the discrepancy.

P7.6 For the laminar parabolic boundary-layer profile of Eq. (7.6), compute the shape factor H and compare with the exact Blasius result, Eq. (7.31).

P7.7 Air at 20°C and 1 atm enters a 40-cm-square duct as in Fig. P7.7. Using the "displacement thickness" concept of Fig. 7.4, estimate (*a*) the mean velocity and (*b*) the mean pressure in the core of the flow at the position $x =$

3 m. (*c*) What is the average gradient, in Pa/m, in this section?

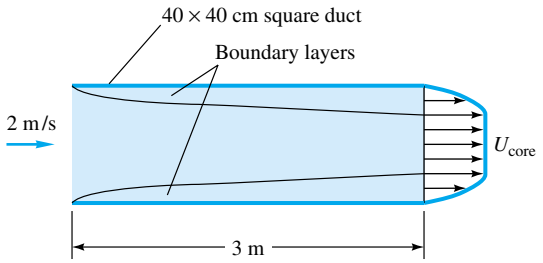

P7.7

P7.8 Air, $\rho = 1.2$ kg/m^3 and $\mu = 1.8$ E-5 kg/(m · s), flows at 10 m/s past a flat plate. At the trailing edge of the plate, the following velocity profile data are measured:

y, mm	0	0.5	1.0	2.0	3.0	4.0	5.0	6.0
u, m/s	0	1.75	3.47	6.58	8.70	9.68	10.0	10.0

If the upper surface has an area of 0.6 m^2, estimate, using momentum concepts, the friction drag, in N, on the upper surface.

P7.9 Repeat the flat-plate momentum analysis of Sec. 7.2 by replacing the parabolic profile, Eq. (7.6), with a more accurate sinusoidal profile:

$$\frac{u}{U} = \sin\frac{\pi y}{2\delta}$$

Compute momentum-integral estimates of c_f, θ/x, δ^*/x, and H.

P7.10 Repeat Prob. 7.9, using the polynomial profile suggested by K. Pohlhausen in 1921:

$$\frac{u}{U} \approx 2\frac{y}{\delta} - 2\frac{y^3}{\delta^3} + \frac{y^4}{\delta^4}$$

Does this profile satisfy the boundary conditions of laminar flat-plate flow?

P7.11 Find the correct form for a cubic velocity-profile polynomial

$$u = A + By + Cy^2 + Dy^3$$

to replace Eq. (7.6) in a flat-plate momentum analysis. Find the value of θ/δ for this profile, but do not pursue the analysis further.

P7.12 The velocity profile shape $u/U \approx 1 - \exp(-4.605y/\delta)$ is a smooth curve with $u = 0$ at $y = 0$ and $u = 0.99U$ at $y = \delta$ and thus would seem to be a reasonable substitute for the parabolic flat-plate profile of Eq. (7.3). Yet when this new profile is used in the integral analysis of Sec. 7.3, we get the lousy result $\delta/x \approx 9.2/\mathrm{Re}_x^{1/2}$, which is 80 percent high. What is the reason for the inaccuracy? [*Hint:* The answer lies in evaluating the laminar boundary-layer momentum equation (7.19*b*) at the wall, $y = 0$.]

P7.13 Derive modified forms of the laminar boundary-layer equations (7.19) for the case of axisymmetric flow along the outside of a circular cylinder of constant radius R, as in Fig. P7.13. Consider the two special cases (*a*) $\delta \ll R$ and (*b*) $\delta \approx R$. What are the proper boundary conditions?

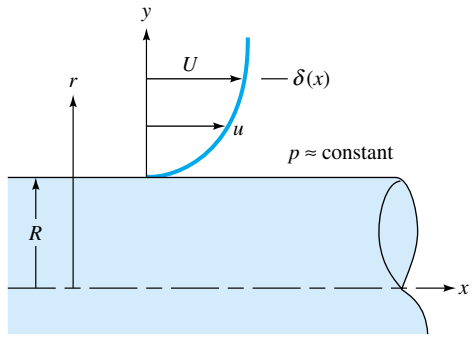

P7.13

P7.14 Show that the two-dimensional laminar-flow pattern with $dp/dx = 0$

$$u = U_0(1 - e^{Cy}) \qquad v = v_0 < 0$$

is an exact solution to the boundary-layer equations (7.19). Find the value of the constant C in terms of the flow parameters. Are the boundary conditions satisfied? What might this flow represent?

P7.15 Discuss whether fully developed laminar incompressible flow between parallel plates, Eq. (4.143) and Fig. 4.16*b*, represents an exact solution to the boundary-layer equations (7.19) and the boundary conditions (7.20). In what sense, if any, are duct flows also boundary-layer flows?

P7.16 A thin flat plate 55 by 110 cm is immersed in a 6-m/s stream of SAE 10 oil at 20°C. Compute the total friction drag if the stream is parallel to (*a*) the long side and (*b*) the short side.

P7.17 Helium at 20°C and low pressure flows past a thin flat plate 1 m long and 2 m wide. It is desired that the total friction drag of the plate be 0.5 N. What is the appropriate absolute pressure of the helium if U = 35 m/s?

P7.18 In Prob. 7.7, when the duct is perfectly square, the core velocity speeds up. Suppose we wish to hold the core velocity constant by slanting the upper and lower walls while keeping the front and rear walls parallel. What angle of slant will be the best approximation? For this condition, what will be the total friction drag on the duct walls?

P7.19 Program a method of numerical solution of the Blasius flat-plate relation, Eq. (7.22), subject to the conditions in (7.23). You will find that you cannot get started without knowing the initial second derivative $f''(0)$, which lies between 0.2 and 0.5. Devise an iteration scheme which starts at $f''(0) \approx 0.2$ and converges to the correct value. Print out $u/U = f'(\eta)$ and compare with Table 7.1.

P7.20 Air at 20°C and 1 atm flows at 20 m/s past the flat plate in Fig. P7.20. A pitot stagnation tube, placed 2 mm from the wall, develops a manometer head $h = 16$ mm of Meriam red oil, SG = 0.827. Use this information to estimate the downstream position x of the pitot tube. Assume laminar flow.

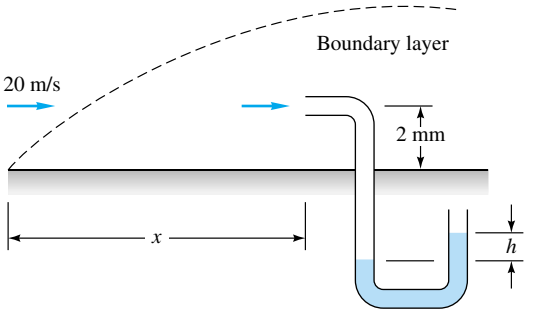

P7.20

P7.21 For the experimental setup of Fig. P7.20, suppose the stream velocity is unknown and the pitot stagnation tube is traversed across the boundary layer of air at 1 atm and 20°C. The manometer fluid is Meriam red oil, and the following readings are made:

y, mm	0.5	1.0	1.5	2.0	2.5	3.0	3.5	4.0	4.5	5.0
h, mm	1.2	4.6	9.8	15.8	21.2	25.3	27.8	29.0	29.7	29.7

Using these data only (not the Blasius theory) estimate (*a*) the stream velocity, (*b*) the boundary-layer thickness, (*c*) the wall shear stress, and (*d*) the total friction drag between the leading edge and the position of the pitot tube.

P7.22 For the Blasius flat-plate problem, Eqs. (7.21) to (7.23), does a two-dimensional stream function $\psi(x, y)$ exist? If so, determine the correct *dimensionless* form for ψ, assuming that $\psi = 0$ at the wall, $y = 0$.

P7.23 Suppose you buy a 4- by 8-ft sheet of plywood and put it on your roof rack. (See Fig. P7.23.) You drive home at 35 mi/h. (*a*) Assuming the board is perfectly aligned with the airflow, how thick is the boundary layer at the end of the board? (*b*) Estimate the drag on the sheet of plywood if the boundary layer remains laminar. (*c*) Estimate the drag on the sheet of plywood if the boundary-layer is turbulent (assume the wood is smooth), and compare the result to that of the laminar boundary-layer case.

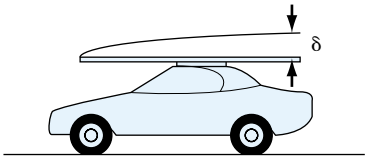

P7.23

***P7.24** Air at 20°C and 1 atm flows past the flat plate in Fig. P7.24 under laminar conditions. There are two equally spaced pitot stagnation tubes, each placed 2 mm from the wall. The manometer fluid is water at 20°C. If $U = 15$ m/s and $L = 50$ cm, determine the values of the manometer readings h_1 and h_2, in mm.

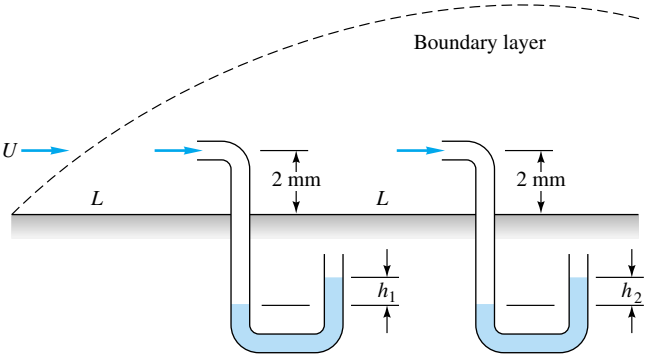

P7.24

P7.25 Modify Prob. 7.24 to the following somewhat more difficult scenario. Let the known data be $U = 15$ m/s and $h_1 = 8$ mm of water. Use this information to determine (*a*) L, in cm, (*b*) h_2, in mm.

P7.26 Consider laminar boundary-layer flow past the square-plate arrangements in Fig. P7.26. Compared to the friction drag of a single plate 1, how much larger is the drag of four plates together as in configurations (*a*) and (*b*)? Explain your results.

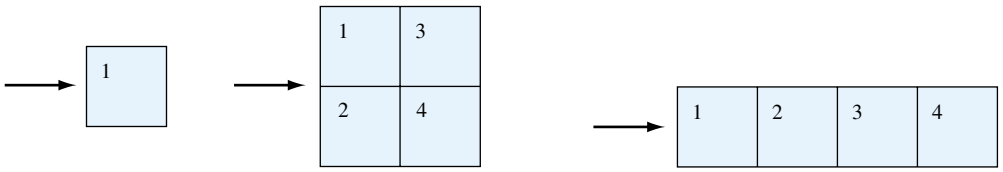

P7.26 (*a*) (*b*)

***P7.27** A thin smooth disk of diameter D is immersed parallel to a uniform stream of velocity U. Assuming laminar flow and using flat-plate theory as a guide, develop an approximate formula for the drag of the disk.

P7.28 Flow straighteners are arrays of narrow ducts placed in wind tunnels to remove swirl and other in-plane secondary velocities. They can be idealized as square boxes constructed by vertical and horizontal plates, as in Fig. P7.28. The cross section is a by a, and the box length is L. Assuming laminar flat-plate flow and an array of $N \times N$ boxes, derive a formula for (*a*) the total drag on the bundle of boxes and (*b*) the effective pressure drop across the bundle.

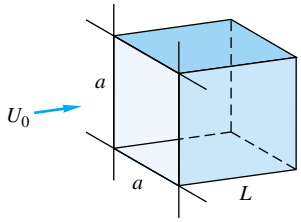

P7.28

P7.29 Let the flow straighteners in Fig. P7.28 form an array of 20×20 boxes of size $a = 4$ cm and $L = 25$ cm. If the approach velocity is $U_0 = 12$ m/s and the fluid is sea-level standard air, estimate (*a*) the total array drag and (*b*) the pressure drop across the array. Compare with Sec. 6.6.

P7.30 Repeat Prob. 7.16 if the fluid is water at 20°C and the plate surface is smooth.

P7.31 Repeat Prob. 7.16 if the fluid is water at 20°C and the plate has an average roughness height of 1.5 mm.

P7.32 A flat plate of length L and height δ is placed at a wall and is parallel to an approaching boundary layer, as in Fig. P7.32. Assume that the flow over the plate is fully turbulent and that the approaching flow is a one-seventh-power law

$$u(y) = U_0\left(\frac{y}{\delta}\right)^{1/7}$$

Using strip theory, derive a formula for the drag coefficient of this plate. Compare this result with the drag of the same plate immersed in a uniform stream U_0.

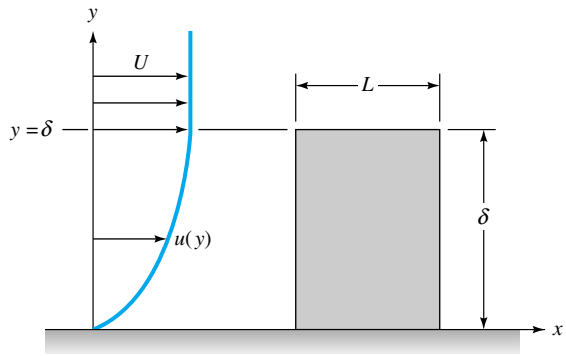

P7.32

P7.33 An alternate analysis of turbulent flat-plate flow was given by Prandtl in 1927, using a wall shear-stress formula from pipe flow

$$\tau_w = 0.0225\rho U^2\left(\frac{\nu}{U\delta}\right)^{1/4}$$

Show that this formula can be combined with Eqs. (7.33) and (7.40) to derive the following relations for turbulent flat-plate flow:

$$\frac{\delta}{x} = \frac{0.37}{\mathrm{Re}_x^{1/5}} \qquad c_f = \frac{0.0577}{\mathrm{Re}_x^{1/5}} \qquad C_D = \frac{0.072}{\mathrm{Re}_L^{1/5}}$$

These formulas are limited to Re_x between 5×10^5 and 10^7.

***P7.34** A thin equilateral-triangle plate is immersed parallel to a 12 m/s stream of water at 20°C, as in Fig. P7.34. Assuming $\mathrm{Re}_{tr} = 5 \times 10^5$, estimate the drag of this plate.

P7.35 The solutions to Prob. 7.26 are (*a*) $F = 2.83F_{1\text{-plate}}$ and (*b*) $F = 2.0F_{1\text{-plate}}$. Do not reveal these results to your friends. Repeat Prob. 7.26 assuming the boundary-layer flow is *turbulent*, and comment on the striking increase in numerical values.

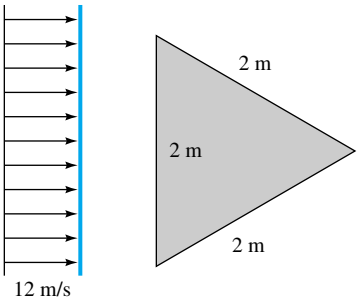

P7.34

P7.36 A ship is 125 m long and has a wetted area of 3500 m^2. Its propellers can deliver a maximum power of 1.1 MW to seawater at 20°C. If all drag is due to friction, estimate the maximum ship speed, in kn.

P7.37 A wind tunnel has a test section 1 m square and 6 m long with air at 20°C moving at an average velocity of 30 m/s. It is planned to slant the walls outward slightly to account for the growing boundary-layer displacement thickness on the four walls, thus keeping the test-section velocity constant. At what angle should they be slanted to keep V constant between $x = 2$ m and $x = 4$ m?

P7.38 Atmospheric boundary layers are very thick but follow formulas very similar to those of flat-plate theory. Consider wind blowing at 10 m/s at a height of 80 m above a smooth beach. Estimate the wind shear stress, in Pa, on the beach if the air is standard sea-level conditions. What will the wind velocity striking your nose be if (*a*) you are standing up and your nose is 170 cm off the ground and (*b*) you are lying on the beach and your nose is 17 cm off the ground?

P7.39 A hydrofoil 50 cm long and 4 m wide moves at 28 kn in seawater at 20°C. Using flat-plate theory with $\mathrm{Re}_{tr} = 5$ E5, estimate its drag, in N, for (*a*) a smooth wall and (*b*) a rough wall, $\epsilon = 0.3$ mm.

P7.40 Hoerner [12, p. 3.25] states that the drag coefficient of a flag in winds, based on total wetted area $2bL$, is approximated by $C_D \approx 0.01 + 0.05L/b$, where L is the flag length in the flow direction. Test Reynolds numbers Re_L were 1 E6 or greater. (*a*) Explain why, for $L/b \geq 1$, these drag values are much higher than for a flat plate. Assuming sea-level standard air at 50 mi/h, with area $bL = 4$ m^2, find (*b*) the proper flag dimensions for which the total drag is approximately 400 N.

P7.41 Repeat Prob. 7.20 with the sole change that the pitot probe is now 10 mm from the wall (5 times higher). Show that the flow there cannot possibly be laminar, and use smooth-wall turbulent-flow theory to estimate the position x of the probe, in m.

***P7.42** A four-bladed helicopter rotor rotates at n r/min in air with properties (ρ, μ). Each blade has chord length C and extends from the center of rotation out to radius R (the hub size is neglected). Assuming turbulent flow from the leading edge, develop an analytical estimate for the power P required to drive this rotor.

P7.43 In the flow of air at 20°C and 1 atm past a flat plate in Fig. P7.43, the wall shear is to be determined at position x by a *floating element* (a small area connected to a strain-gage force measurement). At $x = 2$ m, the element indicates a shear stress of 2.1 Pa. Assuming turbulent flow from the leading edge, estimate (*a*) the stream velocity U, (*b*) the boundary-layer thickness δ at the element, and (*c*) the boundary-layer velocity u, in m/s, at 5 mm above the element.

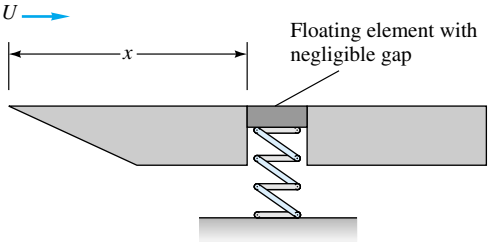

P7.43

P7.44 Extensive measurements of wall shear stress and local velocity for turbulent airflow on the flat surface of the University of Rhode Island wind tunnel have led to the following proposed correlation:

$$\frac{\rho y^2 \tau_w}{\mu^2} \approx 0.0207 \left(\frac{uy}{\nu}\right)^{1.77}$$

Thus, if y and $u(y)$ are known at a point in a flat-plate boundary layer, the wall shear may be computed directly. If the answer to part (*c*) of Prob. 7.43 is $u \approx 27$ m/s, determine whether the correlation is accurate for this case.

P7.45 A thin sheet of fiberboard weighs 90 N and lies on a rooftop, as shown in Fig. P7.45. Assume ambient air at 20°C and 1 atm. If the coefficient of solid friction between board and roof is $\sigma \approx 0.12$, what wind velocity will generate enough fluid friction to dislodge the board?

P7.46 A ship is 150 m long and has a wetted area of 5000 m^2. If it is encrusted with barnacles, the ship requires 7000 hp to overcome friction drag when moving in seawater at 15 kn and 20°C. What is the average roughness of the barnacles? How fast would the ship move with the same power if the surface were smooth? Neglect wave drag.

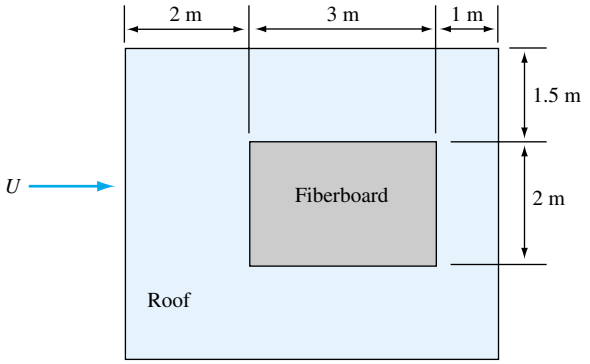

P7.45

P7.47 As a case similar to Example 7.5, Howarth also proposed the adverse-gradient velocity distribution $U = U_0(1 - x^2/L^2)$ and computed separation at $x_{sep}/L = 0.271$ by a series-expansion method. Compute separation by Thwaites' method and compare.

P7.48 In 1957 H. Görtler proposed the adverse-gradient test cases

$$U = \frac{U_0}{(1 + x/L)^n}$$

and computed separation for laminar flow at $n = 1$ to be $x_{sep}/L = 0.159$. Compare with Thwaites' method, assuming $\theta_0 = 0$.

P7.49 Based strictly upon your understanding of flat-plate theory plus adverse and favorable pressure gradients, explain the direction (left or right) for which airflow past the slender airfoil shape in Fig. P7.49 will have lower total (friction + pressure) drag.

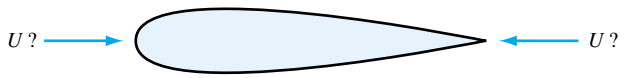

P7.49

***P7.50** For flow past a cylinder of radius R as in Fig. P7.50, the theoretical inviscid velocity distribution along the surface is $U = 2U_0 \sin(x/R)$, where U_0 is the oncoming stream velocity and x is the arc length measured from the nose (Chap. 8). Compute the laminar separation point x_{sep} and θ_{sep} by Thwaites' method, and compare with the digital-computer solution $x_{sep}/R = 1.823$ ($\theta_{sep} = 104.5°$) given by R. M. Terrill in 1960.

P7.51 Consider the flat-walled diffuser in Fig. P7.51, which is similar to that of Fig. 6.26*a* with constant width b. If x is measured from the inlet and the wall boundary layers are

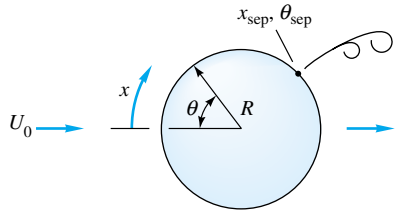

P7.50

thin, show that the core velocity $U(x)$ in the diffuser is given approximately by

$$U = \frac{U_0}{1 + (2x \tan \theta)/W}$$

where W is the inlet height. Use this velocity distribution with Thwaites' method to compute the wall angle θ for which laminar separation will occur in the exit plane when diffuser length $L = 2W$. Note that the result is independent of the Reynolds number.

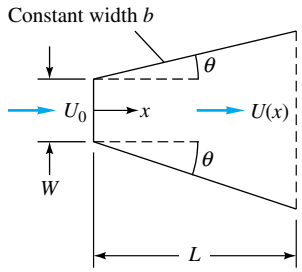

P7.51

***P7.52** In Fig. P7.52 a slanted upper wall creates a favorable pressure gradient on the upper surface of the flat plate. Use Thwaites' theory to estimate

$$C_D = \frac{F}{\frac{1}{2}\rho U_0^2 b L}$$

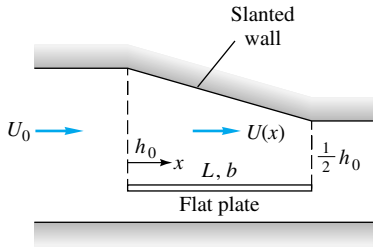

P7.52

on the upper plate surface if $U_0 L/\nu = 10^5$. Compare with Eq. (7.27).

P7.53 From Table 7.2, the drag coefficient of a wide plate normal to a stream is approximately 2.0. Let the stream conditions be U_∞ and p_∞. If the average pressure on the front of the plate is approximately equal to the free-stream stagnation pressure, what is the average pressure on the rear?

P7.54 A chimney at sea level is 2 m in diameter and 40 m high. When it is subjected to 50 mi/h storm winds, what is the estimated wind-induced bending moment about the bottom of the chimney?

P7.55 A ship tows a submerged cylinder, which is 1.5 m in diameter and 22 m long, at 5 m/s in fresh water at 20°C. Estimate the towing power, in kW, required if the cylinder is (*a*) parallel and (*b*) normal to the tow direction.

P7.56 A delivery vehicle carries a long sign on top, as in Fig. P7.56. If the sign is very thin and the vehicle moves at 55 mi/h, estimate the force on the sign (*a*) with no crosswind and (*b*) with a 10 mi/h crosswind.

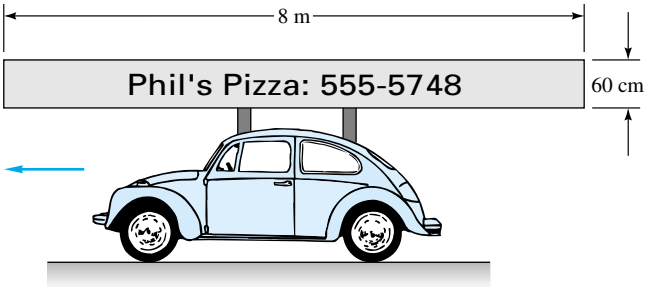

P7.56

P7.57 The main cross-cable between towers of a coastal suspension bridge is 60 cm in diameter and 90 m long. Estimate the total drag force on this cable in crosswinds of 50 mi/h. Are these laminar-flow conditions?

P7.58 A long cylinder of rectangular cross section, 5 cm high and 30 cm long, is immersed in water at 20°C flowing at 12 m/s parallel to the long side of the rectangle. Estimate the drag force on the cylinder, per unit length, if the rectangle (*a*) has a flat face or (*b*) has a rounded nose.

P7.59 Joe can pedal his bike at 10 m/s on a straight level road with no wind. The rolling resistance of his bike is 0.80 N · s/m, i.e., 0.80 N of force per m/s of speed. The drag area ($C_D A$) of Joe and his bike is 0.422 m^2. Joe's mass is 80 kg and that of the bike is 15 kg. He now encounters a head wind of 5.0 m/s. (*a*) Develop an equation for the speed at which Joe can pedal into the wind. [*Hint:* A cubic equation for V will result.] (*b*) Solve for V, i.e., how fast can Joe ride into the head wind? (*c*) Why is the result not simply $10 - 5.0 = 5.0$ m/s, as one might first suspect?

P7.60 A fishnet consists of 1-mm-diameter strings overlapped and knotted to form 1- by 1-cm squares. Estimate the drag of 1 m^2 of such a net when towed normal to its plane at 3 m/s in 20°C seawater. What horsepower is required to tow 400 ft^2 of this net?

P7.61 A filter may be idealized as an array of cylindrical fibers normal to the flow, as in Fig. P7.61. Assuming that the fibers are uniformly distributed and have drag coefficients given by Fig. 7.16*a*, derive an approximate expression for the pressure drop Δp through a filter of thickness L.

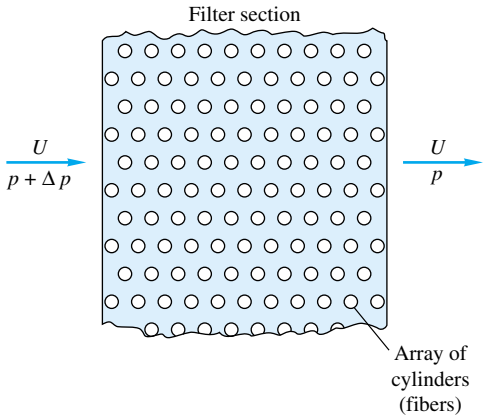

P7.61

P7.62 A sea-level smokestack is 52 m high and has a square cross section. Its supports can withstand a maximum side force of 90 kN. If the stack is to survive 90-mi/h hurricane winds, what is its maximum possible width?

P7.63 The cross section of a cylinder is shown in Fig. P7.63. Assume that on the front surface the velocity is given by potential theory (Sec. 8.4), $V = 2U_\infty \sin\theta$, from which the surface pressure is computed by Bernoulli's equation. In

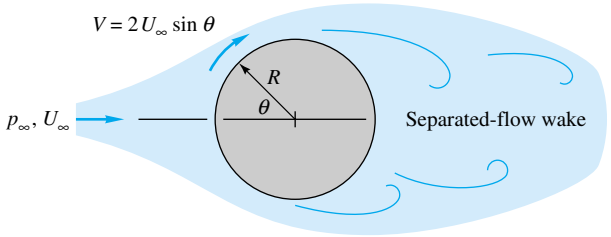

P7.63

the separated flow on the rear, the pressure is assumed equal to its value at $\theta = 90°$. Compute the theoretical drag coefficient and compare with Table 7.2.

P7.64 A parachutist jumps from a plane, using an 8.5-m-diameter chute in the standard atmosphere. The total mass of the chutist and the chute is 90 kg. Assuming an open chute and quasi-steady motion, estimate the time to fall from 2000- to 1000-m altitude.

P7.65 The drag of a sphere at very low Reynolds numbers $\mathrm{Re}_D \ll 1$ was given analytically by G. G. Stokes in 1851: $F = 3\pi\mu VD$ [2, pp. 175–178]. This formula is an example of Stokes' *law of creeping motion,* where inertia is negligible. Show that the drag coefficient in this region is $C_D = 24/\mathrm{Re}_D$. A 1-mm-diameter sphere falls in 20°C glycerin at 2.5 mm/s. Is this a creeping motion? Compute (*a*) the Reynolds number, (*b*) the drag, and (*c*) the specific gravity of the sphere.

P7.66 A sphere of density ρ_s and diameter D is dropped from rest in a fluid of density ρ and viscosity μ. Assuming a constant drag coefficient C_{d_0}, derive a differential equation for the fall velocity $V(t)$ and show that the solution is

$$V = \left[\frac{4gD(S-1)}{3C_{d_0}}\right]^{1/2} \tanh Ct$$

$$C = \left[\frac{3gC_{d_0}(S-1)}{4S^2D}\right]^{1/2}$$

where $S = \rho_s/\rho$ is the specific gravity of the sphere material.

P7.67 Apply the theory of Prob. 7.66 to a steel sphere of diameter 2 cm, dropped from rest in water at 20°C. Estimate the time required for the sphere to reach 99 percent of its terminal (zero-acceleration) velocity.

P7.68 A baseball weighs 145 g and is 7.35 cm in diameter. It is dropped from rest from a 35-m-high tower at approximately sea level. Assuming a laminar-flow drag coefficient, estimate (*a*) its terminal velocity and (*b*) whether it will reach 99 percent of its terminal velocity before it hits the ground.

P7.69 Two baseballs from Prob. 7.68 are connected to a rod 7 mm in diameter and 56 cm long, as in Fig. P7.69. What power, in W, is required to keep the system spinning at 400 r/min? Include the drag of the rod, and assume sea-level standard air.

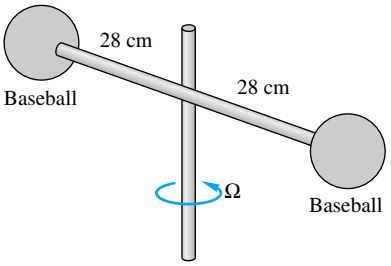

P7.69

P7.70 A baseball from Prob. 7.68 is batted upward during a game at an angle of 45° and an initial velocity of 98 mi/h. Neglect spin and lift. Estimate the horizontal distance traveled, (*a*) neglecting drag and (*b*) accounting for drag in a numerical (computer) solution with a transition Reynolds number $\mathrm{Re}_{D,\mathrm{crit}} = 2.5$ E5.

P7.71 A football weighs 0.91 lbf and approximates an ellipsoid 6 in in diameter and 12 in long (Table 7.3). It is thrown upward at a 45° angle with an initial velocity of 80 ft/s. Neglect spin and lift. Assuming turbulent flow, estimate the horizontal distance traveled, (*a*) neglecting drag and (*b*) accounting for drag with a numerical (computer) model.

P7.72 A settling tank for a municipal water supply is 2.5 m deep, and 20°C water flows through continuously at 35 cm/s. Estimate the minimum length of the tank which will ensure that all sediment (SG = 2.55) will fall to the bottom for particle diameters greater than (*a*) 1 mm and (*b*) 100 μm.

P7.73 A balloon is 4 m in diameter and contains helium at 125 kPa and 15°C. Balloon material and payload weigh 200 N, not including the helium. Estimate (*a*) the terminal ascent velocity in sea-level standard air, (*b*) the final standard altitude (neglecting winds) at which the balloon will come to rest, and (*c*) the minimum diameter (<4 m) for which the balloon will just barely begin to rise in sea-level standard air.

P7.74 If $D = 4$ m in Prob. 7.73 and the helium remains at 15°C and 125 kPa, estimate the time required for the balloon to rise through the standard atmosphere from sea level to its equilibrium altitude, which is approximately 4000 m.

P7.75 The helium-filled balloon in Fig. P7.75 is tethered at 20°C and 1 atm with a string of negligible weight and drag. The diameter is 50 cm, and the balloon material weighs 0.2 N,

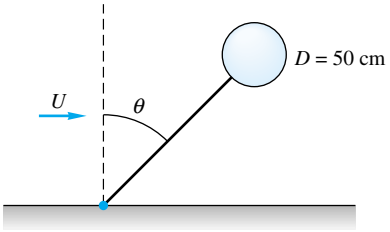

P7.75

not including the helium. The helium pressure is 120 kPa. Estimate the tilt angle θ if the airstream velocity U is (*a*) 5 m/s or (*b*) 20 m/s.

P7.76 Extend Prob. 7.75 to make a smooth plot of tilt angle θ versus stream velocity U in the range $1 < U < 12$ mi/h. (A spreadsheet is recommended for this task.) Comment on the effectiveness of this system as an air-velocity instrument.

P7.77 Modify Prob. 7.75 as follows: Let the fluid be water at 20°C, and let the 50-cm-diameter sphere be solid cork (SG = 0.16). Estimate the tilt angle θ if the water velocity U is 3 m/s.

P7.78 Apply Prob. 7.61 to a filter consisting of 300-μm-diameter fibers packed 250 per square centimeter in the plane of Fig. P7.61. For air at 20°C and 1 atm flowing at 1.5 m/s, estimate the pressure drop if the filter is 5 cm thick.

P7.79 Assume that a radioactive dust particle approximates a sphere of density 2400 kg/m^3. How long, in days, will it take such a particle to settle to sea level from an altitude of 12 km if the particle diameter is (*a*) 1 μm or (*b*) 20 μm?

P7.80 A heavy sphere attached to a string should hang at an angle θ when immersed in a stream of velocity U, as in Fig. P7.80. Derive an expression for θ as a function of the sphere and flow properties. What is θ if the sphere is steel (SG = 7.86) of diameter 3 cm and the flow is sea-level standard air at $U = 40$ m/s? Neglect the string drag.

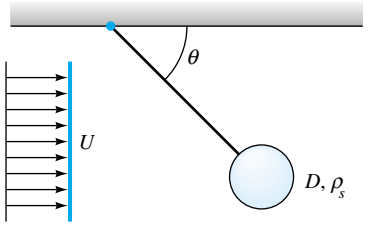

P7.80

P7.81 A typical U.S. Army parachute has a projected diameter of 28 ft. For a payload mass of 80 kg, (*a*) what terminal velocity will result at 1000-m standard altitude? For the same velocity and net payload, what size drag-producing "chute" is required if one uses a square flat plate held (*b*) vertically and (*c*) horizontally? (Neglect the fact that flat shapes are not dynamically stable in free fall.)

P7.82 The average skydiver with parachute unopened weighs 175 lbf and has a drag area $C_DA = 9$ ft^2 spread-eagled and 1.2 ft^2 falling feet first [12, p. 313]. What are the minimum and maximum terminal speeds that can be achieved by a skydiver at 5000-ft standard altitude?

P7.83 A high-speed car has a drag coefficient of 0.3 and a frontal area of 1 m^2. A parachute is to be used to slow this car from 80 to 40 m/s in 8 s. What should the chute diameter be? What distance will be traveled during this deceleration? Take $m = 2000$ kg.

P7.84 A Ping-Pong ball weighs 2.6 g and has a diameter of 3.8 cm. It can be supported by an air jet from a vacuum cleaner outlet, as in Fig. P7.84. For sea-level standard air, what jet velocity is required?

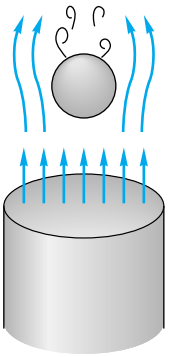

P7.84

***P7.85** An aluminum cylinder (SG = 2.7) slides concentrically down a taut 1-mm-diameter wire as shown in Fig. P7.85. Its length $L = 8$ cm, and its radius $R = 1$ cm. A 2-mm-diameter hole down the cylinder center is lubricated by SAE 30 oil at 20°C. Estimate the terminal fall velocity V of the cylinder if ambient air drag is (*a*) neglected and (*b*) included. Assume air at 1 atm and 20°C.

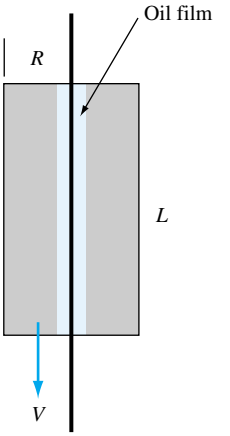

P7.85

P7.86 Hoerner [Ref. 12, pp. 3–25] states that the drag coefficient of a flag of 2:1 aspect ratio is 0.11 based on planform area. The University of Rhode Island has an aluminum flagpole 25 m high and 14 cm in diameter. It flies equal-sized national and state flags together. If the fracture stress of aluminum is 210 MPa, what is the maximum flag size that can be used yet avoids breaking the flagpole in hurricane (75 mi/h) winds?

P7.87 A tractor-trailer truck has a drag-area $C_DA = 8$ m^2 bare and 6.7 m^2 with an aerodynamic deflector (Fig. 7.18*b*). Its rolling resistance is 50 N for each mile per hour of speed. Calculate the total horsepower required at sea level with and without the deflector if the truck moves at (*a*) 55 mi/h and (*b*) 75 mi/h.

P7.88 A pickup truck has a clean drag-area C_DA of 35 ft^2. Estimate the horsepower required to drive the truck at 55 mi/h (*a*) clean and (*b*) with the 3- by 6-ft sign in Fig. P7.88 installed if the rolling resistance is 150 lbf at sea level.

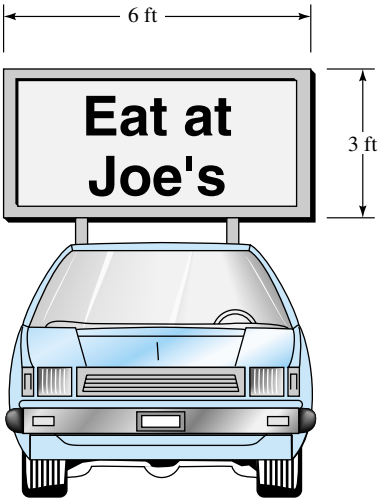

P7.88

P7.89 A water tower is approximated by a 15-m-diameter sphere mounted on a 1-m-diameter rod 20 m long. Estimate the bending moment at the root of the rod due to aerodynamic forces during hurricane winds of 40 m/s.

P7.90 In the great hurricane of 1938, winds of 85 mi/h blew over a boxcar in Providence, Rhode Island. The boxcar was 10 ft high, 40 ft long, and 6 ft wide, with a 3-ft clearance above tracks 4.8 ft apart. What wind speed would topple a boxcar weighing 40,000 lbf?

***P7.91** A cup anemometer uses two 5-cm-diameter hollow hemispheres connected to 15-cm rods, as in Fig. P7.91. Rod drag is negligible, and the central bearing has a retarding torque of 0.004 N · m. Making simplifying assumptions to average out the time-varying geometry, estimate and plot the variation of anemometer rotation rate Ω with wind velocity U in the range $0 < U < 25$ m/s for sea-level standard air.

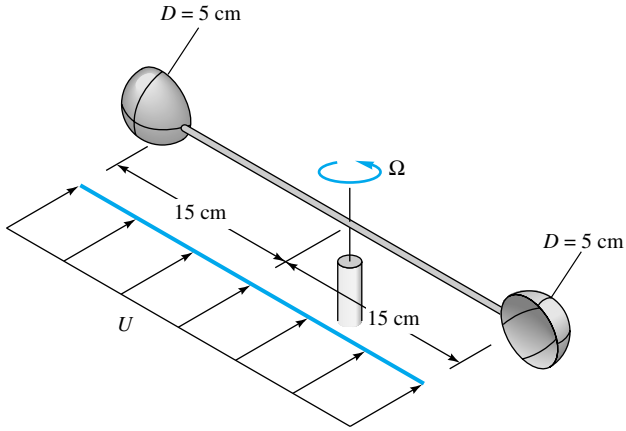

P7.91

P7.92 A 1500-kg automobile uses its drag area $C_DA = 0.4$ m^2, plus brakes and a parachute, to slow down from 50 m/s. Its brakes apply 5000 N of resistance. Assume sea-level standard air. If the automobile must stop in 8 s, what diameter parachute is appropriate?

P7.93 A hot-film probe is mounted on a cone-and-rod system in a sea-level airstream of 45 m/s, as in Fig. P7.93. Estimate the maximum cone vertex angle allowable if the flow-induced bending moment at the root of the rod is not to exceed 30 N · cm.

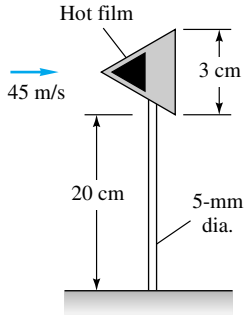

P7.93

P7.94 A rotary mixer consists of two 1-m-long half-tubes rotating around a central arm, as in Fig. P7.94. Using the drag from Table 7.2, derive an expression for the torque T required to drive the mixer at angular velocity Ω in a fluid

of density ρ. Suppose that the fluid is water at 20°C and the maximum driving power available is 20 kW. What is the maximum rotation speed Ω r/min?

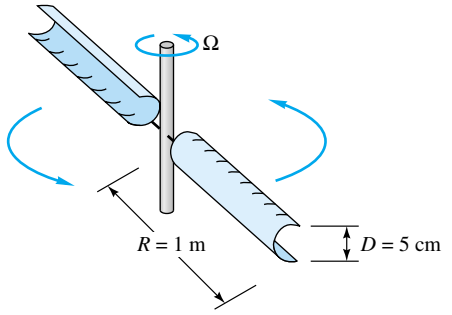

P7.94

P7.95 An airplane weighing 12 kN, with a drag-area $C_D A \approx 5$ m^2, lands at sea level at 55 m/s and deploys a drag parachute 3 m in diameter. No other brakes are applied. (*a*) How long will it take the plane to slow down to 30 m/s? (*b*) How far will it have traveled in that time?

***P7.96** A Savonius rotor (Fig. 6.29*b*) can be approximated by the two open half-tubes in Fig. P7.96 mounted on a central axis. If the drag of each tube is similar to that in Table 7.2, derive an approximate formula for the rotation rate Ω as a function of U, D, L, and the fluid properties (ρ, μ).

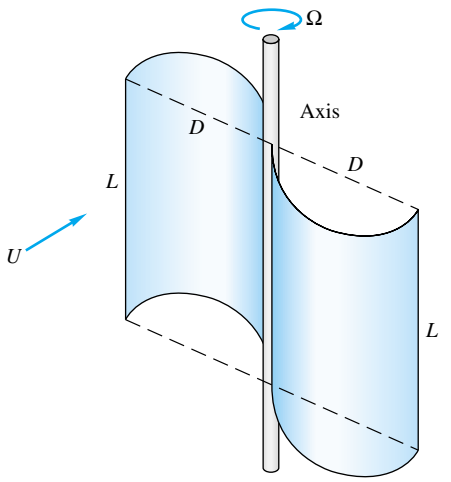

P7.96

P7.97 A simple measurement of automobile drag can be found by an unpowered *coastdown* on a level road with no wind. Assume constant rolling resistance. For an automobile of mass 1500 kg and frontal area 2 m^2, the following velocity-versus-time data are obtained during a coastdown:

t, s	0	10	20	30	40
V, m/s	27.0	24.2	21.8	19.7	17.9

Estimate (*a*) the rolling resistance and (*b*) the drag coefficient. This problem is well suited for digital-computer analysis but can be done by hand also.

***P7.98** A buoyant ball of specific gravity SG < 1 dropped into water at inlet velocity V_0 will penetrate a distance h and then pop out again, as in Fig. P7.98. Make a dynamic analysis of this problem, assuming a constant drag coefficient, and derive an expression for h as a function of the system properties. How far will a 5-cm-diameter ball with SG $= 0.5$ and $C_D \approx 0.47$ penetrate if it enters at 10 m/s?

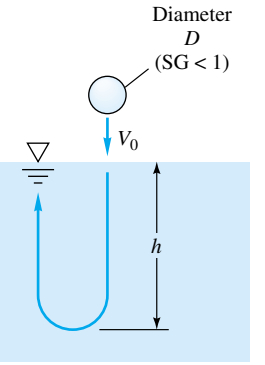

P7.98

P7.99 Two steel balls (SG $= 7.86$) are connected by a thin hinged rod of negligible weight and drag, as in Fig. P7.99. A stop prevents the rod from rotating counterclockwise. Estimate the sea-level air velocity U for which the rod will first begin to rotate clockwise.

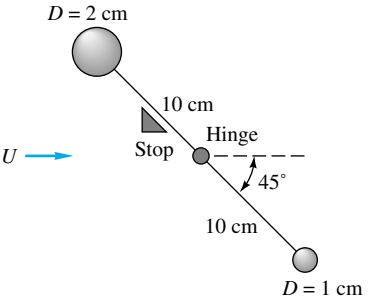

P7.99

P7.100 In creeping motion or *Stokes' flow* at velocity U past a sphere of diameter D, density (fluid inertia) is unimportant and the drag force is $F = 3\pi\mu UD$. This formula is valid if $\text{Re}_D \leq 1.0$ (see Fig. 7.16*b*). (*a*) Verify that Stokes' formula is equivalent to $C_D = 24/\text{Re}_D$. (*b*) Determine the largest diameter raindrop whose terminal fall velocity follows Stokes' formula in sea-level standard air.

P7.101 Icebergs can be driven at substantial speeds by the wind. Let the iceberg be idealized as a large, flat cylinder, $D \gg L$, with one-eighth of its bulk exposed, as in Fig. P7.101. Let the seawater be at rest. If the upper and lower drag forces depend upon relative velocities between the iceberg and the fluid, derive an approximate expression for the steady iceberg speed V when driven by wind velocity U.

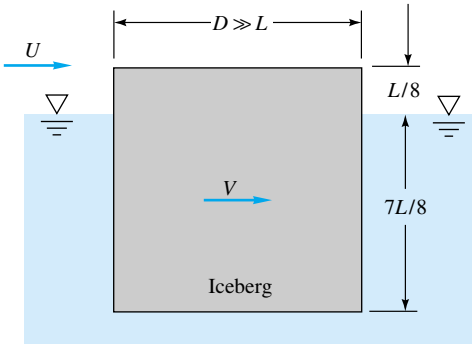

P7.101

P7.102 Sand particles (SG = 2.7), approximately spherical with diameters from 100 to 250 μm, are introduced into an upward-flowing stream of water at 20°C. What is the minimum water velocity which will carry all the sand particles *upward*?

P7.103 When immersed in a uniform stream V, a heavy rod hinged at A will hang at *Pode's angle* θ, after an analysis by L. Pode in 1951 (Fig. P7.103). Assume that the cylinder has normal drag coefficient C_{DN} and tangential coefficient C_{DT} which relate the drag forces to V_N and V_T, respectively. Derive an expression for Pode's angle as a function of the flow and rod parameters. Find θ for a steel rod, $L = 40$ cm, $D = 1$ cm, hanging in sea-level air at $V = 35$ m/s.

P7.104 Suppose that the body in Fig. P7.103 is a thin plate weighing 0.6 N, of length $L = 20$ cm and width $b = 4$ cm into the paper. For sea-level standard air, plot Pode's angle θ versus velocity V in the range $0 < V < 40$ m/s. Would this device make a good air-velocity meter (anemometer)?

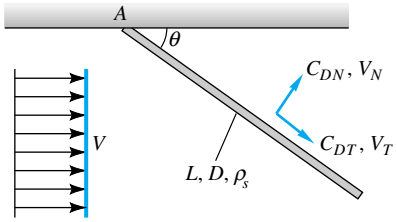

P7.103

P7.105 A ship 50 m long, with a wetted area of 800 m^2, has the hull shape tested in Fig. 7.19. There are no bow or stern bulbs. The total propulsive power available is 1 MW. For seawater at 20°C, plot the ship's velocity V kn versus power P for $0 < P < 1$ MW. What is the most efficient setting?

P7.106 A smooth steel 1-cm-diameter sphere ($W \approx 0.04$ N) is fired vertically at sea level at the initial supersonic velocity $V_0 = 1000$ m/s. Its drag coefficient is given by Fig. 7.20. Assuming that the speed of sound is constant at $a \approx 343$ m/s, compute the maximum altitude of the projectile (*a*) by a simple analytical estimate and (*b*) by a digital-computer program.

P7.107 Repeat Prob. 7.106 if the body is a 9-mm steel bullet ($W \approx 0.07$ N) which approximates the "pointed body of revolution" in Fig. 7.20.

P7.108 The data in Fig. P7.108 are for the lift and drag of a spinning sphere from Ref. 12, pp. 7–20. Suppose that a tennis ball ($W \approx 0.56$ N, $D \approx 6.35$ cm) is struck at sea level with initial velocity $V_0 = 30$ m/s and "topspin" (front of the ball rotating downward) of 120 r/s. If the initial height of the ball is 1.5 m, estimate the horizontal distance traveled before it strikes the ground.

P7.109 Repeat Prob. 7.108 if the ball is struck with "underspin" (front of the ball rotating upward).

P7.110 A baseball pitcher throws a curveball with an initial velocity of 65 mi/h and a spin of 6500 r/min about a vertical axis. A baseball weighs 0.32 lbf and has a diameter of 2.9 in. Using the data of Fig. P7.108 for turbulent flow, estimate how far such a curveball will have deviated from its straight-line path when it reaches home plate 60.5 ft away.

***P7.111** A table tennis ball has a mass of 2.6 g and a diameter of 3.81 cm. It is struck horizontally at an initial velocity of 20 m/s while it is 50 cm above the table, as in Fig. P7.111. For sea-level air, what spin, in r/min, will cause the ball to strike the opposite edge of the table, 4 m away? Make an analytical estimate, using Fig. P7.108, and account for the fact that the ball decelerates during flight.

P7.108

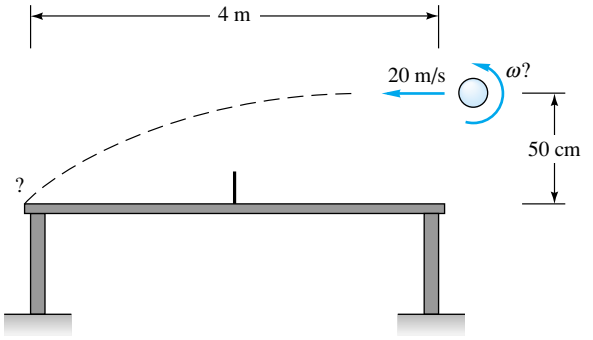

P7.111

P7.112 Repeat Prob. 7.111 by making a detailed digital-computer solution for the flight path of the ball. Use Fig. P7.108 for lift and drag.

P7.113 An automobile has a mass of 1000 kg and a drag-area $C_D A = 0.7$ m^2. The rolling resistance of 70 N is approximately constant. The car is coasting without brakes at 90 km/h as it begins to climb a hill of 10 percent grade (slope = $\tan^{-1} 0.1 = 5.71°$). How far up the hill will the car come to a stop?

***P7.114** Suppose that the car in Prob. 7.113 is placed at the top of the 10 percent grade hill and released from rest to coast down without brakes. What will be its speed, in km/h, after dropping a vertical distance of 20 m?

P7.115 An airplane weighs 180 kN and has a wing area of 160 m^2 and a mean chord of 4 m. The airfoil properties are given by Fig. 7.25. If the airplane cruises at 250 mi/h at 3000-m standard altitude, what propulsive power is required to overcome wing drag?

P7.116 The airplane of Prob. 7.115 is designed to land at $V_0 = 1.2V_{stall}$, using a split flap set at 60°. What is the proper landing speed in mi/h? What power is required for takeoff at the same speed?

P7.117 Suppose that the airplane of Prob. 7.115 takes off at sea level without benefit of flaps, with C_L constant so that the takeoff speed is 100 mi/h. Estimate the takeoff distance if the thrust is 10 kN. How much thrust is needed to make the takeoff distance 1250 m?

***P7.118** Suppose that the airplane of Prob. 7.115 is fitted with all the best high-lift devices of Fig. 7.28. What is its minimum stall speed in mi/h? Estimate the stopping distance if the plane lands at $V_0 = 1.25V_{stall}$ with constant $C_L = 3.0$ and $C_D = 0.2$ and the braking force is 20 percent of the weight on the wheels.

P7.119 An airplane has a mass of 5000 kg, a maximum thrust of 7000 N, and a rectangular wing with aspect ratio 6.0. It takes off at sea level with a 60° split flap whose two-dimensional properties are shown in Fig. 7.25. Assume all lift and all drag are due to the wing. What is the proper wing size if the takeoff distance is to be 1 km?

P7.120 Show that if Eqs. (7.70) and (7.71) are valid, the maximum lift-to-drag ratio occurs when $C_D = 2C_{D\infty}$. What are

$(L/D)_{max}$ and α for a symmetric wing when AR = 5 and $C_{D\infty} = 0.009$?

P7.121 In gliding (unpowered) flight, the lift and drag are in equilibrium with the weight. Show that if there is no wind, the aircraft sinks at an angle

$$\tan\theta \approx \frac{\text{drag}}{\text{lift}}$$

For a sailplane of mass 200 kg, wing area 12 m^2, and aspect ratio 11, with an NACA 0009 airfoil, estimate (*a*) the stall speed, (*b*) the minimum gliding angle, and (*c*) the maximum distance it can glide in still air when it is 1200 m above level ground.

P7.122 A boat of mass 2500 kg has two hydrofoils, each of chord 30 cm and span 1.5 m, with $C_{L,max} = 1.2$ and $C_{D\infty} = 0.08$. Its engine can deliver 130 kW to the water. For seawater at 20°C, estimate (*a*) the minimum speed for which the foils support the boat and (*b*) the maximum speed attainable.

P7.123 In prewar days there was a controversy, perhaps apocryphal, about whether the bumblebee has a legitimate aerodynamic right to fly. The average bumblebee (*Bombus terrestris*) weighs 0.88 g, with a wing span of 1.73 cm and a wing area of 1.26 cm^2. It can indeed fly at 10 m/s. Using fixed-wing theory, what is the lift coefficient of the bee at this speed? Is this reasonable for typical airfoils?

***P7.124** The bumblebee can hover at zero speed by flapping its wings. Using the data of Prob. 7.123, devise a theory for flapping wings where the downstroke approximates a short flat plate normal to the flow (Table 7.3) and the upstroke is feathered at nearly zero drag. How many flaps per second of such a model wing are needed to support the bee's weight? (Actual measurements of bees show a flapping rate of 194 Hz.)

Word Problems

W7.1 How do you *recognize* a boundary layer? Cite some physical properties and some measurements which reveal appropriate characteristics.

W7.2 In Chap. 6 the Reynolds number for transition to turbulence in pipe flow was about $Re_{tr} \approx 2300$, whereas in flat-plate flow $Re_{tr} \approx 1$ E6, nearly three orders of magnitude higher. What accounts for the difference?

W7.3 Without writing any equations, give a verbal description of boundary-layer displacement thickness.

W7.4 Describe, in words only, the basic ideas behind the "boundary-layer approximations."

W7.5 What is an *adverse* pressure gradient? Give three examples of flow regimes where such gradients occur.

W7.6 What is a *favorable* pressure gradient? Give three examples of flow regimes where such gradients occur.

W7.7 The drag of an airfoil (Fig. 7.12) increases considerably if you turn the sharp edge around 180° to face the stream. Can you explain this?

W7.8 In Table 7.3, the drag coefficient of a spruce tree decreases sharply with wind velocity. Can you explain this?

W7.9 Thrust is required to propel an airplane at a finite forward velocity. Does this imply an energy loss to the system? Explain the concepts of thrust and drag in terms of the first law of thermodynamics.

W7.10 How does the concept of *drafting,* in automobile and bicycle racing, apply to the material studied in this chapter?

W7.11 The circular cylinder of Fig. 7.13 is doubly symmetric and therefore should have no lift. Yet a lift sensor would definitely reveal a finite root-mean-square value of lift. Can you explain this behavior?

W7.12 Explain in words why a thrown spinning ball moves in a curved trajectory. Give some physical reasons why a side force is developed in addition to the drag.

Fundamentals of Engineering Exam Problems

FE7.1 A smooth 12-cm-diameter sphere is immersed in a stream of 20°C water moving at 6 m/s. The appropriate Reynolds number of this sphere is approximately
(*a*) 2.3 E5, (*b*) 7.2 E5, (*c*) 2.3 E6, (*d*) 7.2 E6, (*e*) 7.2 E7

FE7.2 If, in Prob. FE7.1, the drag coefficient based upon frontal area is 0.5, what is the drag force on the sphere?
(*a*) 17 N, (*b*) 51 N, (*c*) 102 N, (*d*) 130 N, (*e*) 203 N

FE7.3 If, in Prob. FE7.1, the drag coefficient based upon frontal area is 0.5, at what terminal velocity will an aluminum sphere (SG = 2.7) fall in still water?
(*a*) 2.3 m/s, (*b*) 2.9 m/s, (*c*) 4.6 m/s, (*d*) 6.5 m/s, (*e*) 8.2 m/s

FE7.4 For flow of sea-level standard air at 4 m/s parallel to a thin flat plate, estimate the boundary-layer thickness at $x = 60$ cm from the leading edge:
(*a*) 1.0 mm, (*b*) 2.6 mm, (*c*) 5.3 mm, (*d*) 7.5 mm, (*e*) 20.2 mm

FE7.5 In Prob. FE7.4, for the same flow conditions, what is the wall shear stress at $x = 60$ cm from the leading edge?
(*a*) 0.053 Pa, (*b*) 0.11 Pa, (*c*) 0.16 Pa, (*d*) 0.32 Pa, (*e*) 0.64 Pa

FE7.6 Wind at 20°C and 1 atm blows at 75 km/h past a flagpole 18 m high and 20 cm in diameter. The drag coefficient,

based upon frontal area, is 1.15. Estimate the wind-induced bending moment at the base of the pole.
(*a*) 9.7 kN · m, (*b*) 15.2 kN · m, (*c*) 19.4 kN · m, (*d*) 30.5 kN · m, (*e*) 61.0 kN · m

FE7.7 Consider wind at 20°C and 1 atm blowing past a chimney 30 m high and 80 cm in diameter. If the chimney may fracture at a base bending moment of 486 kN · m, and its drag coefficient based upon frontal area is 0.5, what is the approximate maximum allowable wind velocity to avoid fracture?
(*a*) 50 mi/h, (*b*) 75 mi/h, (*c*) 100 mi/h, (*d*) 125 mi/h, (*e*) 150 mi/h

FE7.8 A dust particle of density 2600 kg/m^3, small enough to satisfy Stokes' drag law, settles at 1.5 mm/s in air at 20°C and 1 atm. What is its approximate diameter?
(*a*) 1.8 μm, (*b*) 2.9 μm, (*c*) 4.4 μm, (*d*) 16.8 μm, (*e*) 234 μm

FE7.9 An airplane has a mass of 19,550 kg, a wing span of 20 m, and an average wing chord of 3 m. When flying in air of density 0.5 kg/m^3, its engines provide a thrust of 12 kN against an overall drag coefficient of 0.025. What is its approximate velocity?
(*a*) 250 mi/h, (*b*) 300 mi/h, (*c*) 350 mi/h, (*d*) 400 mi/h, (*e*) 450 mi/h

FE7.10 For the flight conditions of the airplane in Prob. FE7.9 above, what is its approximate lift coefficient?
(*a*) 0.1, (*b*) 0.2, (*c*) 0.3, (*d*) 0.4, (*e*) 0.5

Comprehensive Problems

C7.1 Jane wants to estimate the drag coefficient of herself on her bicycle. She measures the projected frontal area to be 0.40 m^2 and the rolling resistance to be 0.80 N · s/m. The mass of the bike is 15 kg, while the mass of Jane is 80 kg. Jane coasts down a long hill which has a constant 4° slope. (See Fig. C7.1.) She reaches a terminal (steady state) speed of 14 m/s down the hill. Estimate the aerodynamic drag coefficient C_D of the rider and bicycle combination.

C7.2 Air at 20°C and 1 atm flows at $V_{avg} = 5$ m/s between long, smooth parallel heat-exchanger plates 10 cm apart, as in Fig. C7.2. It is proposed to add a number of widely spaced 1-cm-long interrupter plates to increase the heat transfer, as shown. Although the flow in the channel is turbulent, the boundary layers over the interrupter plates are essentially laminar. Assume all plates are 1 m wide into the paper. Find (*a*) the pressure drop in Pa/m without the small plates present. Then find (*b*) the number of small plates per meter of channel length which will cause the pressure drop to rise to 10.0 Pa/m.

C7.3 A new pizza store is planning to open. They will, of course, offer free delivery, and therefore need a small delivery car with a large sign attached. The sign (a flat plate) is 1.5 ft high and 5 ft long. The boss (having no feel for fluid mechanics) mounts the sign bluntly facing the wind. One of his drivers is taking fluid mechanics and tells his boss he can save lots of money by mounting the sign parallel to the wind. (See Fig. C7.3.) (*a*) Calculate the drag (in lbf) on the *sign alone* at 40 mi/h (58.7 ft/s) in *both orientations.* (*b*) Suppose the car without any sign has a drag coefficient of 0.4 and a frontal area of 40 ft^2. For $V = 40$ mi/h, calculate the *total* drag of the car-sign combination for both orientations. (*c*) If the car has a rolling resistance of 40 lbf at 40 mi/h, calculate the horsepower required by the engine to drive the car at 40 mi/h in both orientations. (*d*) Finally, if the engine can deliver 10 hp for 1 h on a gallon of gasoline, calculate the fuel efficiency in mi/gal for both orientations at 40 mi/h.

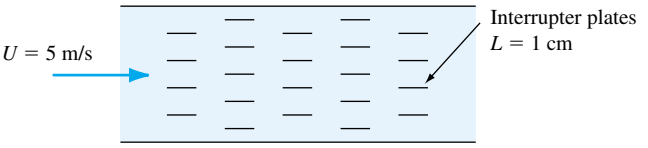

C7.2

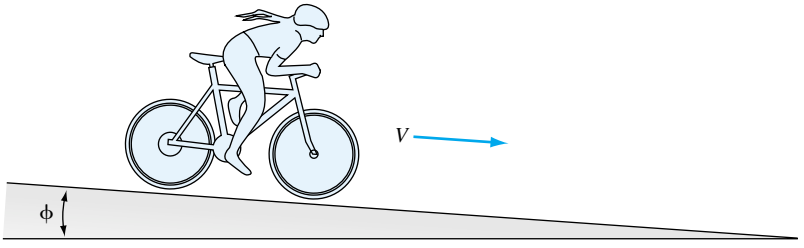

C7.1

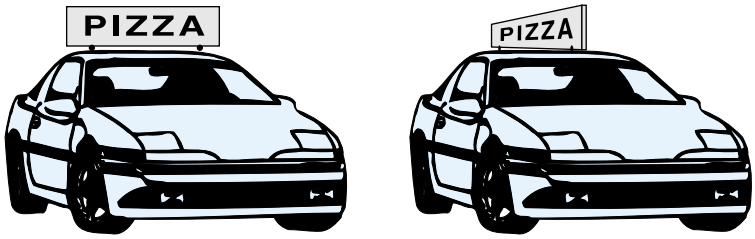

C7.3

C7.4 Consider a pendulum with an unusual bob shape: a hemispherical cup of diameter D whose axis is in the plane of oscillation, as in Fig. C7.4. Neglect the mass and drag of the rod L. (*a*) Set up the differential equation for the oscillation $\theta(t)$, including different cup drag (air density ρ) in each direction, and (*b*) nondimensionalize this equation. (*c*) Determine the natural frequency of oscillation for small $\theta \ll 1$ rad. (*d*) For the special case $L = 1$ m, $D = 10$ cm, $m = 50$ g, and air at 20°C and 1 atm, with $\theta(0) = 30°$, find (numerically) the time required for the oscillation amplitude to drop to 1°.

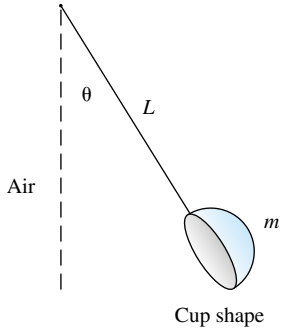

C7.4

Design Project

D7.1 It is desired to design a cup anemometer for wind speed, similar to Fig. P7.91, with a more sophisticated approach than the "average-torque" method of Prob. 7.91. The design should achieve an approximately linear relation between wind velocity and rotation rate in the range $20 < U < 40$ mi/h, and the anemometer should rotate at about 6 r/s at $U = 30$ mi/h. All specifications—cup diameter D, rod length L, rod diameter d, the bearing type, and all materials—are to be selected through your analysis. Make suitable assumptions about the instantaneous drag of the cups and rods at any given angle $\theta(t)$ of the system. Compute the instantaneous torque $T(t)$, and find and integrate the instantaneous angular acceleration of the device. Develop a complete theory for rotation rate versus wind speed in the range $0 < U < 50$ mi/h. Try to include actual commercial bearing-friction properties.

References

1. H. Schlichting, *Boundary Layer Theory,* 7th ed., McGraw-Hill, New York, 1979.
2. F. M. White, *Viscous Fluid Flow,* 2d ed., McGraw-Hill, New York, 1991.
3. L. Rosenhead (ed.), *Laminar Boundary Layers,* Oxford University Press, London, 1963.
4. D. A. Anderson, J. C. Tannehill, and R. H. Pletcher, *Computational Fluid Mechanics and Heat Transfer,* 2d ed., Hemisphere, New York, 1997.
5. R. H. Pletcher and C. L. Dancey, "A Direct Method of Calculating through Separated Regions in Boundary Layer Flow," *J. Fluids Eng.,* September 1976, pp. 568–572.
6. P. K. Chang, *Control of Flow Separation,* McGraw-Hill, New York, 1976. See also P. K. Chang, *Recent Development in Flow Separation,* Pang Han Pub. Co., Seoul, Korea, 1983.
7. T. von Kármán, "On Laminar and Turbulent Friction," *Z. Angew. Math. Mech.,* vol. 1, 1921, pp. 235–236.
8. G. B. Schubauer and H. K. Skramstad, "Laminar Boundary Layer Oscillations and Stability of Laminar Flow," *Natl. Bur. Stand. Res. Pap.* 1772, April 1943 (see also *J. Aero. Sci.,* vol. 14, 1947, pp. 69–78, and *NACA Rep.* 909, 1947).
9. W. Rodi, *Turbulence Models and Their Application in Hydraulics,* Brookfield Pub., Brookfield, VT, 1984.

10. P. W. Runstadler, Jr., et al., "Diffuser Data Book," Creare Inc., *Tech. Note* 186, Hanover, NH, May 1975.
11. B. Thwaites, "Approximate Calculation of the Laminar Boundary Layer," *Aeronaut. Q.,* vol. 1, 1949, pp. 245–280.
12. S. F. Hoerner, *Fluid Dynamic Drag,* published by the author, Midland Park, NJ, 1965.
13. J. D. Anderson, *Fundamentals of Aerodynamics,* 2d ed., McGraw-Hill, New York, 1991.
14. V. Tucker and G. C. Parrott, "Aerodynamics of Gliding Flight of Falcons and Other Birds," *J. Exp. Biol.,* vol. 52, 1970, pp. 345–368.
15. Eric Tupper, *Introduction to Naval Architecture,* Butterworth, Boston, 1996.
16. I. H. Abbott and A. E. von Doenhoff, *Theory of Wing Sections,* Dover, New York, 1959.
17. R. L. Kline and F. F. Fogleman, Airfoil for Aircraft, U.S. Patent 3,706,430 Dec. 19, 1972.
18. T. Y. Yu et al. (eds.), *Swimming and Flying in Nature: Proceedings of a Symposium,* Plenum, New York, 1975.
19. National Committee for Fluid Mechanics Films, *Illustrated Experiments in Fluid Mechanics,* M.I.T. Press, Cambridge, MA, 1972.
20. E. M. Uram and H. E. Weber (eds.), "Laminar and Turbulent Boundary Layers," *ASME Symp. Proc.,* vol. I00167, February 1984.
21. G. Sovran, T. Morel, and W. T. Mason, Jr. (eds.), *Aerodynamic Drag Mechanisms of Bluff Bodies and Road Vehicles,* Plenum, New York, 1978.
22. W. H. Hucho, *Aerodynamics of Road Vehicles,* Butterworth, Boston, 1986.
23. R. D. Blevins, *Applied Fluid Dynamics Handbook,* van Nostrand Reinhold, New York, 1984.
24. R. C. Johnson, Jr., G. E. Ramey, and D. S. O'Hagen, "Wind Induced Forces on Trees," *J. Fluids Eng.,* vol. 104, March 1983, pp. 25–30.
25. P. W. Bearman et al., "The Effect of a Moving Floor on Wind-Tunnel Simulation of Road Vehicles," Paper No. 880245, SAE Transactions, *J. Passenger Cars,* vol. 97, sec. 4, 1988, pp. 4.200–4.214.
26. *CRC Handbook of Tables for Applied Engineering Science,* 2d ed., CRC Press, Boca Raton, FL, 1973.
27. T. Inui, "Wavemaking Resistance of Ships," *Trans. Soc. Nav. Arch. Marine Engrs.,* vol. 70, 1962, pp. 283–326.
28. L. Larsson et al., "A Method for Resistance and Flow Prediction in Ship Design," *Trans. Soc. Nav. Arch. Marine Engrs.,* vol. 98, 1990, pp. 495–535.
29. R. L. Street, G. Z. Watters, and J. K. Vennard, *Elementary Fluid Mechanics,* 7th ed., Wiley, New York, 1995.
30. J. D. Anderson, Jr., *Modern Compressible Flow, with Historical Perspective,* 2d ed., McGraw-Hill, New York, 1990.
31. J. D. Anderson, Jr., *Hypersonic and High Temperature Gas Dynamics,* McGraw-Hill, New York, 1989.
32. J. Rom, *High Angle of Attack Aerodynamics: Subsonic, Transonic, and Supersonic Flows,* Springer-Verlag, New York, 1992.
33. S. Vogel, "Drag and Reconfiguration of Broad Leaves in High Winds," *J. Exp. Bot.,* vol. 40, no. 217, August 1989, pp. 941–948.
34. S. Vogel, *Life in Moving Fluids,* Princeton University Press, Princeton, NJ, 1981.
35. J. A. C. Humphrey (ed.), *Proceedings 1st International Symposium on Mechanics of Plants, Animals, and Their Environment,* Engineering Foundation, New York, January 1998.
36. D. D. Joseph, R. Bai, K. P. Chen, and Y. Y. Renardy, "Core-Annular Flows," *Annu. Rev. Fluid Mech.,* vol. 29, 1997, pp. 65–90.
37. J. W. Hoyt and R. H. J. Sellin, "Scale Effects in Polymer Solution Pipe Flow," *Experiments in Fluids,* vol. 15, no. 1, June 1993, pp. 70–74.
38. S. Nakao, "Application of V-shape Riblets to Pipe Flows," *J. Fluids Eng.,* vol. 113, December 1991, pp. 587–590.
39. P. R. Bandyopadhyay, "Review: Mean Flow in Turbulent Boundary Layers Disturbed to Alter Skin Friction," *J. Fluids Eng.,* vol. 108, 1986, pp. 127–140.
40. N. K. Madavan, S. Deutsch, and C. L. Merkle, "Measurements of Local Skin Friction in a Microbubble Modified Turbulent Boundary Layer," *J. Fluid Mech.,* vol. 156, 1985, pp. 237–256.
41. S. M. Trujillo, D. G. Bogard, and K. S. Ball, "Drag Reduction in a Turbulent Boundary Layer by Wall Oscillation," Paper AIAA 97-1870, AIAA Shear Flow Control Conference, Austin, TX, December 1997.
42. J. G. Chandler, "Microplanes," *Popular Science,* January 1998, pp. 54–59.